Reconstruction of Antarctic climate variability using high resolution ice core stratigraphy

A THESIS SUBMITTED IN PARTIAL FULFILLMENT FOR THE DEGREE OF

DOCTOR OF PHILOSOPHY

IN THE SCHOOL OF EARTH, OCEAN AND ATMOSPHERIC SCIENCES
GOA UNIVERSITY

By

Rahul Dey
National Centre for Polar and Ocean Research
Headland Sada, Vasco da Gama
Goa, India

NOVEMBER 2023

DECLARATION

I, Rahul Dey, hereby declare that this thesis represents work that has been carried out by me and that it has not been submitted, either in part or full, to any other University or Institution for the award of any research degree.

Place: Taleigao Plateau

Rahul Dey

Date:

CERTIFICATE

I hereby certify that the above Declaration of the candidate, Rahul Dey, is true, and the work was carried out under my/our supervision.

Dr Thamban Meloth

Research Supervisor
Director and Scientist G
National Centre for Antarctic & Ocean Research
Vasco-da-Gama, Goa 403 804

Dr Kotha Mahender

Research co-supervisor
Professor (retd)
School of Earth, Ocean & Atmospheric Sciences
Goa University, Taleigao, Goa 403 206

Acknowledgements

In the pursuit of knowledge, I have been fortunate to receive invaluable support from mentors and colleagues, serving as my guiding light. This journey underscores the potency of collaboration and steadfast encouragement in the field of scientific exploration. To begin with, I extend profound gratitude to my supervisor, Dr Thamban Meloth, for his unwavering guidance, consistent support, and infinite patience throughout my PhD journey. His profound knowledge and extensive experience have played a pivotal role in both my academic achievements and daily life. The motivation and inspiration drawn from him were indispensable in shaping my overall experience. A special acknowledgement to my co-supervisor, Prof Kotha Mahender, whose continuous guidance proved crucial to the success of my doctoral work.

My sincere thanks to Dr Kenichi Matsuoka for his continued encouragement, guidance, and support throughout the research process. His insightful suggestions significantly enriched both my scientific knowledge and the final outcomes of this thesis. Special thanks to Dr Bhanu Pratap for his unwavering support and motivation, and for being like a mentor throughout my PhD journey. I'd like to thank my DRC members, Dr Anthony A. A. Viegas and Dr Sushant S. Naik, for their constructive discussions and valuable suggestions.

Acknowledgement is owed to the National Centre for Polar and Ocean Research for providing essential academic and administrative support. Heartfelt gratitude goes to the former Director of NCPOR, Dr. M. Ravichandran, Secretary, Ministry of Earth Science (MoES), for consistent support and encouragement throughout my research journey. My deepest thanks to Dr Rahul Mohan and Dr Laluraj CM for their positivity and support,

significantly contributing to my research journey. Recognition is extended to the Ministry of Earth Sciences (MoES), Government of India, for funding through the "PACER-Cryosphere and Climate" project and the University Grants Commission (UGC) for the NET (JRF) fellowship. Special thanks to the Vice-Chancellor, Registrar, Dean, and all staff members of the School of Earth, Ocean, and Atmospheric Science at Goa University for their unwavering support. Sincere appreciation to all scientists and staff members of the NCPOR family. I would especially thank Mr Prashant Redkar, Mr Ashish Painginkar, and Mr Tariq Ejaz for their immense support during ice core processing and analysis.

True friends are the compass that guides us through life's journey, shining brightest in our darkest moments. I thank Priyesh, Nibedita, Padmasini, and Priyanka for their constant comfort and for making this journey a pleasant one. I sincerely thank Lathika, Gautami, Aritri, Mahalingathan, Tarique, Nuruzzamma, Ajit, and Vikram for their words of advice that helped me stay on the right track.

Finally, and most importantly, I express my deepest gratitude to my parents, Mrs. Shila Dey and Mr. Rabi Dey, and my brother Rohan for being the cornerstone of love and support during this long and arduous journey!

Rahul Dey

Dedicated to a dream,

the struggles and,

the perseverance…

Contents

List of figures

List of tables

List of abbreviations

AIS	Antarctic Ice Sheet
ASL	Amundsen Sea Low
CLAHE	Contrast Limited Adaptive Histogram Equalisation
DIR	Djupranen Ice Rise
DML	Dronning Maud Land
DMS	Dimethylsulfide
DMSP	Dimethylsulphoniopropionate
ENSO	El Niño Southern Oscillation
EPP	Expanded Polypropylene
FIS	Fimbul Ice Shelf
GNSS	Global Navigation Satellite System
GPR	Ground Penetrating Radar
IC	Ion Chromatograph
ILCS	Intermediate Layer Core Scanner
LGR	Los Gatos Research
LIR	Leningradkollen Ice Shelf
MAD	Median Absolute Deviation
METUM	Met Office Unified Model
MSA	Methane Sulphonic Acid
PDH	Positive Degree Hour
RC	Reconstructed Component
RM	Running Mean
SAM	Southern Annular Mode
SIC	Sea Ice Concentration
SMB	Surface Mass Balance
SOI	Southern Oscillation Index
VS	Visual Stratigraphy
WAIS	West Antarctic Ice Sheet

Introduction

1.1 Overview

Antarctica plays a crucial role in the global climate system as it serves as a heat sink for the transport of heat from the equator to high latitudes through extratropical cyclones and ocean currents (Trenberth and Solomon, 1994; King and Turner, 1997). The continent's isolation within the Southern Ocean enables the formation of a persistent westerly circulation of cyclonic systems around it (King and Turner, 1997). The high albedo of Antarctica and its associated sea ice cover cools the continent, affecting the earth's energy budget. This cooling causes a temperature inversion that produces persistent katabatic winds that blow off the continent (Parish, 1988). The most significant interaction between Antarctica and the global climate system is the delicate mass balance of the ice sheets, which contain 61% of the world's fresh water. The Antarctic Ice Sheet (AIS) is the largest reservoir of fresh water globally and has the potential to raise the global sea level by approximately 58.3 meters if it were to melt completely (IPCC, 2013).

The climate variability in the Antarctic region is not well-characterized, mainly due to lack of direct climate observations and large interannual to decadal climate variability (Stenni et al., 2017). Antarctica has reliable and continuous temperature records for only a few decades. The use of proxy records from ice cores is one of the most accurate methods to study climate change in Antarctica beyond instrumental limits (Schneider et al., 2006; Thamban et al., 2013). Since temperatures across most of the Antarctic ice sheets are extremely cold, layers of snowfall at the surface never melt; instead, successive snowfall covers the previous layers and are gradually buried. Deeper in the ice sheet, deformation of ice thins each layer due to the large stress, spreading them towards the ice sheet edge, where they eventually reach the ocean as ice shelves or icebergs (Wolff, 2012). The annual snowfall rate ranges from as low as 2 cm w.e. over the high plateau region of East Antarctic (Bromwich, 1988) to several meters in coastal Antarctica (Lenaerts et al., 2012). By vertically drilling through the ice layers, the chemical and physical properties of the ice can be determined as a function of depth and, ultimately, time. Ice cores contain information about the past climate and environmental conditions on timescales ranging from decades to hundreds of millennia and provide direct records of atmosphere composition. Major findings related to global climate change have been established through the study of several ice cores from Antarctica over the last few decades.

However, from a long-term paleoclimatological perspective, the coastal regions of Antarctica remain one of the least explored and not-so-well-understood parts of the continent. This is majorly because the coastal areas are mostly low-lying, prone to summertime melting and seasonal storm activities, and have significantly high ice flow rates, making retrieving a reliable and continuous climatic record difficult. The Dronning Maud Land (DML) coast is one such data-scarce region with only a few ice core records extending beyond the instrumental period and only two records extending beyond the 20^{th} century (Kaczmarska et al., 2004; Philippe et al., 2016). The ice rises fringing the coast of DML, which are grounded features, have their local flow regime and are independent of the ice sheet or ice shelves surrounding them. The divide/summit of these ice rises can have practically zero horizontal flow, and the Raymond effect results in an anticline effect, thus making it easier to retrieve longer records from relatively shallow ice cores. While the effect of summertime melting and noise from seasonal storm activities are still significant, the undisturbed stratigraphy at the ice rise divide makes it an ideal location for retrieving ice cores in coastal areas.

Various stratigraphical methods can be used to establish the annual dating of ice cores by examining seasonal variations in the isotopic composition of the ice, impurity concentrations, and the physical properties of snow (Gow, 1965). The seasonal variation in stable isotope content is one such method, which is used to build a chronology for many ice cores (Dansgaard, 1964). This method has the advantage of not requiring any special precautions to prevent contamination of samples. However, a damping effect associated with diffusion processes occurring during firn formation restricts the stable isotope method to dating the upper portion of firn in locations where snow accumulation rate is below 200 kg $m^{-2}yr^{-1}$ (Johnsen, 1977). Moreover, the seasonal signal in isotopic records is negatively impacted by frequent summertime melting in low-lying areas, making it challenging to identify annual layers.

Among chemical species currently measured in polar precipitation, sea salt species like sodium and chloride exhibit strong seasonality in Antarctic snow layers. Calcium, having two major sources (marine and continental dust), exhibits little variation in Antarctica. Acidic species like nitrate, sulphate, and methane sulphonic acid (MSA) show moderate maxima in spring and summer in Antarctic snow. MSA is a special case for which the seasonality exhibits a complex picture. However, with the proximity to the open ocean and frequent storm activities, the chemical species exhibit a rather noisy signal and require

significant post-processing to extract clear annual signals from the record. All of this calls for a more reliable proxy for identifying annual layers in the ice cores from coastal areas, which is not heavily influenced by summertime melting and due to the proximity to the open ocean. The presence of melt layers also provides an opportunity to understand the summertime melt variability over the region on a longer timescale and the atmospheric factors controlling this variability. All of this combined information can provide a detailed understanding of the region's climatic variability and the stability of the ice rises, which themselves act as a support system for the larger ice sheet.

1.2 Antarctic in a changing climate scenario

Over the past few years, significant changes in the Antarctic climate have been observed, including rapid warming on the Antarctic Peninsula (Vaughan et al., 2003), strengthening of the polar vortex (Thompson and Solomon, 2002), ice shelf collapse (Scambos et al., 2000), and ecological shifts (Doran et al., 2002). In the last hundred years, temperatures have risen significantly, indicating a high degree of confidence, like the observed changes at the global scale. According to (Karl and Trenberth, 2003), the early 21st-century climate will likely exceed natural climate variability over the past millennium.

Due to its unique physical characteristics, Antarctica has a complex interaction with the global climate system. This results from its extreme cold, windy, high altitude, and driest climate on the planet. There is an ice sheet covering nearly the entire continent that contains 58.3 m of sea level equivalent water (IPCC, 2013). This ice sheet has a high shortwave albedo, a nearly black-body longwave emissivity, and a surface-based temperature inversion, so the surface energy balance over the ice sheet is imperative. In addition to the atmospheric circulation and the midlatitude climate, the Antarctic surface climate is closely associated with atmospheric circulation, heavily influencing the earth's climatic systems (van den Broeke et al., 2004).

Increasing ocean temperatures, sea level rise, and warming of the Antarctic climate generally have been attributed to a greater likelihood of the marine-grounded West Antarctic Ice Sheet (WAIS) collapsing, which would lead to an increase in global sea level. Shepherd et al. (2004) have identified warmer oceans as being associated with accelerated WAIS thinning, and (Scambos et al., 2000) have identified warmer surface temperatures in the Antarctic Peninsula region as being associated with rapid retreat of ice shelves. As a result of the retreat of ice shelves, the sea level does not directly increase, but it may accelerate the

discharge of glaciers inland.

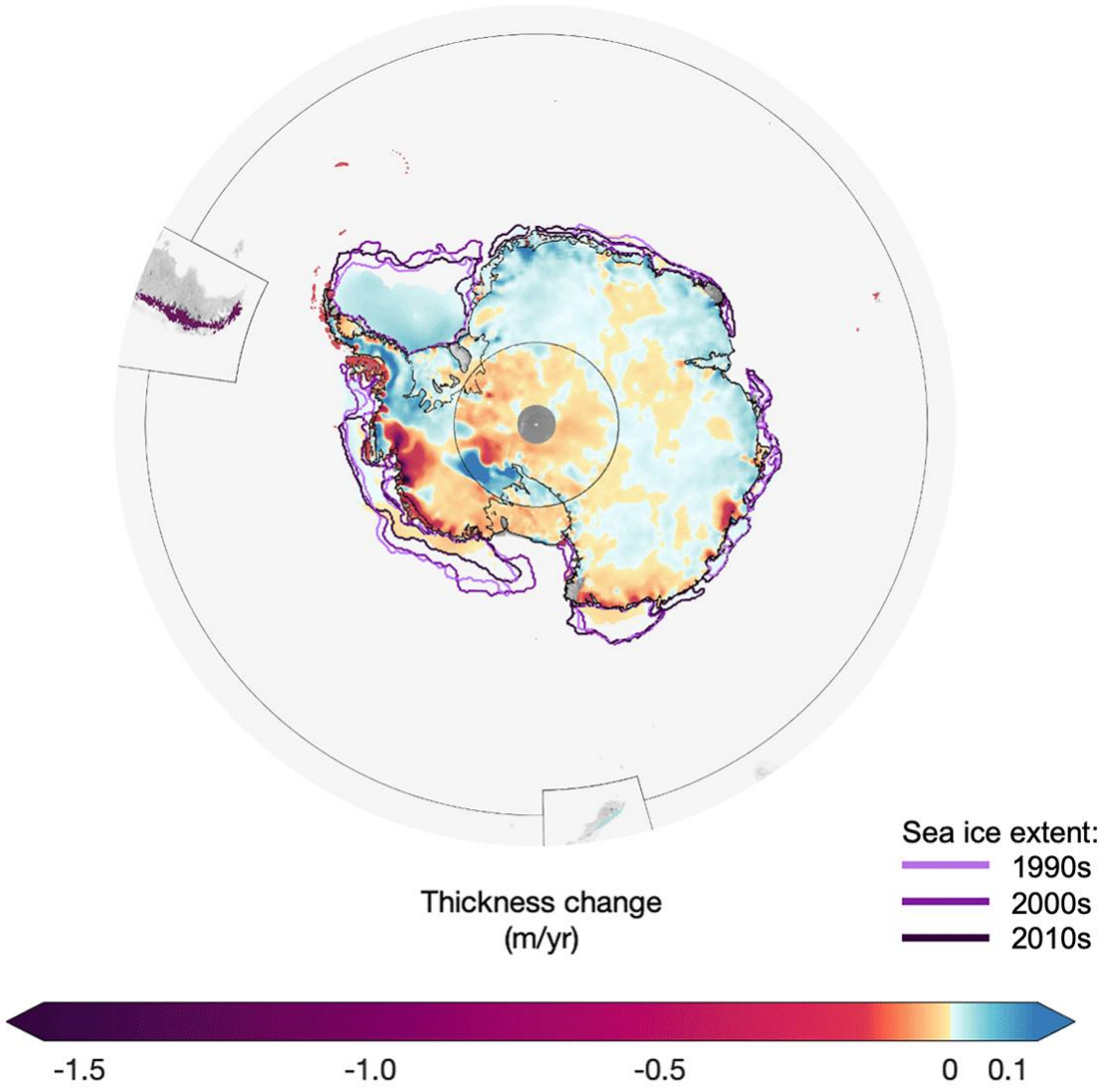

Figure 1.1 Average rate of ice thickness change in the Southern Hemisphere. Changes in Antarctic ice sheet (1992–2017) thickness were estimated using repeat satellite altimetry following the methods of Shepherd et al. (2019). Sea ice thickness trends between 1990 and 2019 are determined from numerical sea ice and ocean modelling (Zhang and Rothrock, 2003), as well as the average minimum of sea ice extent in February (Antarctic) and September (Arctic) (purple lines) for each decade during the same period. Adapted from (Slater et al., 2021).

According to several studies, there are unusual regional trends in the modern Antarctic climate compared to global trends, largely due to significant changes in atmospheric circulation during the instrumental era of Antarctic observation (Kwok and Comiso, 2002; Thompson and Solomon, 2002; Shindell and Schmidt, 2004). While surface temperatures in some parts of the Antarctic continent have increased, the continent overall has experienced a cooling trend. Similar trends are seen in the case of ice sheet thickness

changes (Figure 1.1; Slater et al. (2021)). This cooling trend has been linked to the shift towards the positive phase of the Southern Annular Mode (SAM), a leading pattern of variability in sea level pressures and tropospheric geopotential heights in the Southern Hemisphere extratropical latitudes, accompanied by anomalies in the westerlies and temperatures over the polar region (Kwok and Comiso, 2002; Thompson and Solomon, 2002). This trend has been particularly noticeable in summer and autumn and has been associated with the depletion of stratospheric ozone and an increase in CO_2 concentrations, suggesting that anthropogenically-driven impacts are leading to regional exceptions to the global trend towards warmer conditions (Marshall, 2003; Marshall et al., 2004; Shindell and Schmidt, 2004). Although studies have explored the connection between the El Nino-Southern Oscillation (ENSO) and the Antarctic climate, the significance of ENSO to the Antarctic climate is uncertain (Bertler et al., 2004; Turner, 2004).

1.3 Ice core paleoclimatology and proxies

Ice cores provided an invaluable record of various past environmental conditions such as temperature changes, atmospheric circulation, volcanic eruptions, dust loading, biological processes, and human impact on the environment (Dansgaard, 1964; Johnsen, 1977; Hammer, 1980; Herron et al., 1981; Kukla and Gavin, 1981; Jouzel and Merlivat, 1984; Legrand and Delmas, 1984; Legrand and Mayewski, 1997). Proxies such as isotopic, major ion, and trace element analysis provide a near instrumental-quality account of these past conditions. Ice cores in locations with high snow accumulation rates offer continuous reconstructions dating back as far as 850,000 years ago, with some being seasonally resolved for the past ~30,000-40,000 years (Bertler and Barrett, 2010). This is particularly significant in Antarctica, where instrumental data are limited in duration and distribution (Jouzel and Merlivat, 1984). Brook (2007) added that major ion analysis is useful in tracing elements from sources such as continental dust, volcanic eruptions, sea salt, and biological processes. Antarctic ice cores offer detailed and well-dated records of marine aerosols and the isotopic makeup of atmospheric water reaching Antarctica. Changes in the concentrations of these elements are connected to historical shifts in sea-ice conditions. Valuable chemical indicators for reconstructing sea-ice history include sea salt (typically expressed as sea salt sodium, $ssNa^+$) and methane sulfonic acid (MSA). Beyond these aerosols, the stable isotope composition ($\delta^{18}O$) of snowfall is influenced by sea-ice extent, impacting moisture sources, air mass transport, atmospheric hydrology, and temperature across Antarctica. These factors collectively shape the $\delta^{18}O$ in snow, highlighting how sea-ice conditions modify the

atmospheric dynamics of the region, ultimately reflected in the preserved composition of ice core archives (Figure 1.2).

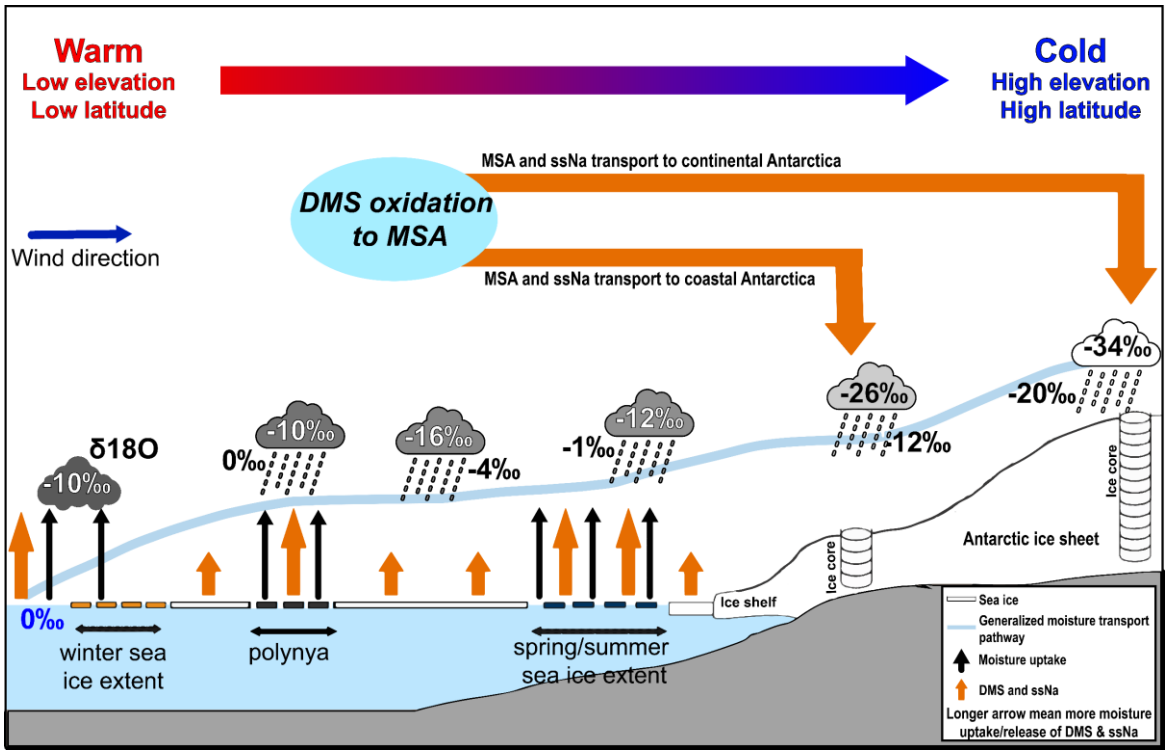

Figure 1.2 Major ice core proxies and their relationship to sea ice.

1.3.1. Major Ions

The use of Na^+ and Cl^- concentrations in ice cores as proxies for sea salt is well-established, as they have a molar ratio similar to that of the bulk seawater value (1.17), and they are sensitive recorders of winds originating over the open ocean (Legrand and Mayewski, 1997; Kreutz et al., 2000). The presence of sea-salt SO_4^{2-} ($ssSO_4^{2-}$) is predominantly sourced from polynyas, frequent spring-time cyclonic activity, bubble bursting, and frost flowers, and they mostly reach Antarctica through lower troposphere. Typically, SO_4^{2-} peaks during summer when the sea ice is at its lowest and reaches its minimum extent mostly during winter (Legrand and Delmas, 1984).

Non-sea salt sulphate ($nssSO_4^{2-}$) can originate from volcanic eruptions, although it is minor except for large eruptions or open-ocean biological reactions occurring mostly in local polynyas (Dixon et al., 2004). Phytoplanktons are known to produce non-sea salt sulphate through the conversion of dimethylsulphoniopropionate (DMSP) to dimethylsulfide (DMS), which then oxidises to form MSA^- and sulphate (Abram et al., 2013b; Sinclair et al., 2014).

According to Legrand and Delmas (1986), the presence of NO_3^- is believed to originate from lightning and soil exhalation in tropical regions. The upper troposphere/lower stratosphere then transports NO_3^- to Antarctica. Katabatic winds can transport the NO^{3-} signature to coastal areas, indicating a contribution from polar stratospheric clouds and thus showing evidence of a stratospheric contribution (Legrand and Mayewski, 1997). Dust-bound NO_3^- is also a significant contributor in coastal Antarctica (Mahalinganathan and Thamban, 2016).

Frost flowers arise when sea ice develops rapidly under cold conditions, and if temperatures drop below -8°C, mirabilite or sodium sulphate will develop from the brine (Kaspari et al., 2005). During this process, approximately 13% of the sodium and most of the sulphate are removed from the solution, creating a separation between the two ions. The surface brine then evaporates, creating a layer of water vapour where frost flowers grow extensively (Martin et al., 1996). Synoptic cyclones and onshore winds transport the frost flowers to coastal sites. These winds need to be strong enough to incorporate salt from the flowers but not so powerful that the flowers are destroyed (Rankin et al., 2000). Frost flowers contribute to 40% of the Na^+ budget in Antarctic ice cores and are more prevalent than open-water production in coastal sites with at least 300 km of sea ice (Rankin et al., 2000; Kaspari et al., 2005). Therefore, the $nssSO_4^{2-}/Na^+$ ratio can be used to estimate sea ice extent by identifying the typical ratio of frost flowers, providing an additional proxy for sea ice extent (Rankin et al., 2000; Dixon et al., 2005).

1.3.2. Water Stable Isotope Ratios

The measurement and analysis of water isotope ratios have played a vital role in enhancing our comprehension of past and present climate. The pioneering studies by Dansgaard (1964) focused on the analysis of meteoric water, spatial variances in deuterium and oxygen-stable isotopes, and the effects of equilibrium and kinetic processes in the hydrological cycle. They also established the link between the isotopic composition of water and various factors such as latitude, elevation, precipitation levels, surface air temperature, and proximity to the coast. Water-stable isotopes exhibit fractionation due to the variance in the mass of water molecules arising from a difference in the number of neutrons. During evaporation, the isotopically heavier molecules (enriched δ^2H (δD) and $\delta^{18}O$) are left behind in the liquid phase, while during condensation, they precipitate as heavier molecules, whereas the remaining air parcel becomes isotopically lighter. For instance, water molecules

are made up of three different isotopic species, namely $H_2{}^{16}O$ (most abundant), $H_2{}^{18}O$, and $HD^{16}O$ (rare). The rare isotopic species' abundance can be presented as ratios of D/H and $^{18}O/^{16}O$. The standard notation for representing the abundance of heavy isotopes is by using δD and $\delta^{18}O$ as:

$$\delta^{18}O(\text{ or } \delta D) = 1000\left[\frac{\left(R_{\text{sample}} - R_{\text{SMOW}}\right)}{R_{\text{SMOW}}}\right]\%0,$$

where $R \equiv \frac{[^{18}O]}{[^{16}O]}$ or $R \equiv \frac{[^{2}H]}{[^{1}H]}$ and R_{SMow} is the corresponding ratio in the Standard Mean Ocean Water (Gonfiantini, 1978).

The process of isotopic fractionation, which occurs due to different vapour pressures for heavy and light isotopes of water, results in an increase of heavy isotopes in the water and a decrease in the vapour phase. The temperature affects this effect, and at 25°C, the $\delta^{18}O$ and δD of water vapour in equilibrium with liquid water are −9.3‰ and −76‰, respectively, which is lower than in liquid ocean water. The kinetic isotope effect, a non-equilibrium process that happens during evaporation, causes a depletion of $\delta^{18}O$ and δD in the water vapour added to air. This effect is due to the difference in diffusion rates between the isotopic species of water. The kinetic isotope effect during evaporation is more significant for $H_2{}^{18}O$ than for $HD^{16}O$ (Clark and Fritz, 1997).

According to Masson-Delmotte et al. (2008), changes that occur after the deposition of ice cores can significantly impact the isotopic signature of water. As a result, understanding these site-specific effects is crucial to providing an accurate quantitative representation of the ice core records. Diffusive processes, which involve the exchange of gases between ice grains and pore spaces, can diminish the amplitude of the isotopic signal with depth (van Ommen and Morgan, 1997; Cuffey and Steig, 1998; Johnsen et al., 2000). Nonetheless, diffusion is generally negligible on interannual timescales for WA ice cores, which have high accumulation rates (Cuffey and Steig, 1998). Back-diffusing techniques (Cuffey and Steig, 1998; Johnsen et al., 2000) have been used to recover the amplitude of the original deposited isotopic signal.

In addition to this, the isotopic signature may exhibit seasonality bias as a result of varying precipitation amounts (Krinner et al., 1997) and environmental conditions, such as warm air temperatures (Sime et al., 2009), which can create a preference towards a synoptic condition and/or a seasonal precipitation bias. To diminish the impact of deposition-related

interference, δ-record stacks have been developed (Fisher et al., 1985; Vinther et al., 2010) from various local cores (van Ommen and Morgan, 1997; Van Ommen et al., 2004) or across larger regions (Küttel et al., 2012). However, Schneider and Noone (2007) cautioned that combining isotope records from different cores may cancel out climatic signals despite the benefits of using core stacks to reduce noise.

1.3.3. Line-scan images

The visual stratigraphy (VS) record obtained from ice cores is a crucial source of information (Langway, 1967). However, early attempts to use such data were challenging due to the limited quality and resolution of drawings and analogue photographs (Alley et al., 1997; Meese et al., 1997). Additionally, the observer-dependent nature of the data made it difficult to verify results later. With the advent of low-cost digital imagery equipment and large data storage media, high-resolution digital recording of VS became feasible. The first high-resolution measurements of VS were conducted at the NGRIP ice core in 2000 (Svensson et al., 2005), and similar measurements have since become widely used in ice core analysis (Takata et al., 2004; McGwire et al., 2008a; McGwire et al., 2008b; Faria et al., 2010). While VS measurements are relatively easy to obtain and non-destructive, their scientific usefulness as paleoclimatic data series has been limited by the level of detail in the records and uncertainties in their interpretation.

The layering observed in ice cores results from varying amounts of impurities scattered throughout the core. These impurities scatter incoming light, and their size and concentration changes create distinguishable horizons in line-scan images (Faria et al., 2010). Each layer most likely corresponds to a single deposition event and reflects the changing chemical and physical conditions present at the time of deposition. However, the inclusions responsible for scattering may take the form of either solid impurities or air bubbles enclosed in the ice, and the resulting scattering depends on their size distribution and quantity. As a result, the information recorded in line-scan images is not unequivocal.

Firn density generally increases with depth (Figure 1.3). Surface snow drift, disintegration and transport by wind, and melt, can increase the surface density to around 280 – 420 kg/m3. Subsequent densification of dry snow is primarily driven by overburden pressure (Herron and Langway, 1980). Up to a density of ~550 kg m^{-3}, densification is most rapid and driven by settling, the physical packing and rounding of snow grains. Between ~550 and ~830 kg m^{-3}, the dominant process is recrystallization and deformation, which

includes sintering as stresses between grains decrease the pressure melting temperature along grain contacts and deformation along the basal planes of ice crystals (Cuffey and Paterson, 2010). Finally, above ~830 kg m^{-3}, densification is driven by plastic deformation, where the compression of closed-off pore space is driven by overburden pressure. This process of firnification also influences the line-scan image brightness of ice cores in shallow depths, which has been one of the major challenges in using visual stratigraphy in the firn section. However, conversely, this brightness change can used to obtain high-resolution density variations of the ice cores (Sjögren et al., 2007; Kinnard et al., 2008).

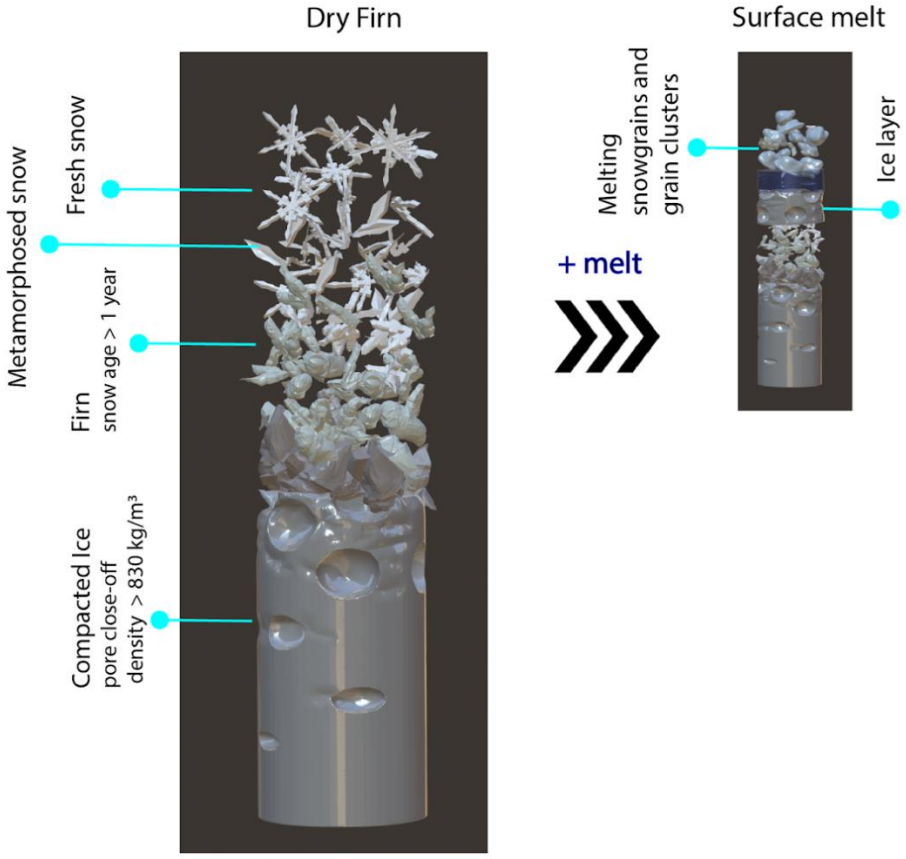

Figure 1.3 Schematic representation of firn columns evolving from dry conditions (left) and the effect of surface melting (right). Adapted from The firn symposium team (2023).

The Antarctic Ice Sheet experiences minimal surface melting during summer due to consistently low air temperatures, except on the Antarctic Peninsula and on or near the marginal ice shelves (Das and Alley, 2005). The primary contributors to mass loss from Antarctica are iceberg calving and melting under the ice shelves, with surface sublimation

and meltwater runoff playing a minor role. Any melting occurring in Antarctica's interior is typically isolated and occurs in response to abnormally high air temperatures.

The formation of melt layers is common in snowpacks and is often associated with strong solar radiation and high. These melt layers can be identified based on their characteristics, which include the presence of liquid melt puddles that percolate into the snowpack. This phenomenon can be observed in both horizontal melt layers and lenses, as well as vertical melt pipes (Pfeffer and Humphrey, 1998), which are distinguishable from the surrounding snowpack due to their lack of bubbles (Figure 1.3). In some cases, water can freeze uniformly within a section of the snowpack where there is no low-permeability layer.

According to Das and Alley (2005), surface melting is minimal in the Antarctic Ice Sheet during the summer due to consistently low air temperatures. Exceptions to this are observed in areas such as the Antarctic Peninsula and on or near the marginal ice shelves. The primary causes of mass loss in Antarctica are calving at the ice shelf front and melting under the ice shelves, while surface sublimation and meltwater runoff play a smaller role. Any melting occurring in Antarctica's interior is typically isolated and occurs in response to abnormally high air temperatures.

Melt layers are a common phenomenon that occurs when the snowpack experiences high temperatures and/or intense solar radiation. They are characterised by the formation of liquid melt puddles on the snow surface, which subsequently percolate into the snowpack. This phenomenon has been extensively studied and categorised into different types, including horizontal melt layers, lenses, and vertical melt pipes. These features can be easily identified in the snowpack's stratigraphy due to their lack of bubbles. Additionally, in certain situations where a low-permeability layer is absent, water may refreeze uniformly within a section of the snowpack (Pfeffer and Humphrey, 1998).

1.3.4. Ice core timescales

There are various methods for dating ice cores, and the choice of method depends on the specific circumstances and available data. The most accurate dating methods are those that are stratigraphically based. If the necessary data for creating such timescales are unavailable, ice flow models of varying complexity can be utilised to estimate the relationship between age and depth (Eisen et al., 2008).

Ice flow models provide valuable information on stress and strain rates in ice sheets.

This information can be utilised to predict the rate at which annual layers thin with depth and construct timescales for ice cores (Dansgaard and Johnsen, 1969; Parrenin et al., 2004). These models range from simple 1D models to more complex ones. Before obtaining an ice core, ice flow models can be used to determine the optimal drilling location based on the constructed timescales. After retrieving the core, data from the ice core can be incorporated into the model. Studies have demonstrated a strong relationship between past accumulation rates and the relative concentration of stable water isotopes ($\delta^{18}O$) in the ice core (Dahl-Jensen et al., 1993), which can be included in the model. Age markers obtained from the ice core data can also be combined with ice flow models to establish timescales for Antarctic ice cores (Parrenin et al., 2004; Parrenin et al., 2007).

The dating of ice cores involves using reference horizons to establish a fixed chronology and counting annual layers to obtain annually resolved data. Reference horizons are created by various events that stand out in the ice core record. The most commonly used reference horizons are layers of high concentrations of sulphuric acid, typically associated with volcanic events. These layers can serve as tie points in the timescale, even when the volcanic event has not been independently dated and can connect individual paleoclimatic records (Hammer, 1980; Vinther et al., 2006).

Other methods can also be used to establish chronologies for ice core records, including wiggle-matching to existing ice or ocean cores. A combination of multiple methods is often used to establish a comprehensive timescale for ice cores. For example, Lemieux-Dudon et al. (2010) utilised flow modelling, age markers from several ice cores, and other methods to simultaneously create a consistent timescale for multiple ice cores.

1.3.5. Major challenges

The composition of snow deposited in the inner part of an ice sheet is influenced by the climate and time of the year, with variations that can be recorded in the ice and preserved over long periods. Antarctic ice cores, in particular, offer a high temporal resolution that enables the identification of seasonal information as well as past climate changes. To establish a counted chronology, the chemical impurities in the ice must be measured at high resolution, which depends on the thickness of the annual layers being studied. However, annual layer resolution is not solely determined by the measurement technique.

In the upper part of an ice core, a clear annual signal is often seen in the $\delta^{18}O$-record of

the ice due to the large temperature differences between summer and winter. However, this signal slowly disappears with depth due to the significant diffusion during the firnification process and molecular diffusion in the ice, which causes the annual layering to diffuse slowly. Another major factor influencing the isotopic record is the frequent summertime melting in the coastal low lying areas. While back-diffusion methods can be used to reconstruct the annual signal, the presence of significant summertime melt can adversely affect reconstruction techniques, resulting in unwanted artefacts. The effect of diffusion in the chemical records is comparatively lesser, but these records are affected by the frequent storm activities in the coastal areas, thus adding noise to the annual signal. Therefore, using traditional proxies for obtaining a timescale and climatic information from ice cores drilled in the coastal areas, like over ice rises, have their unique challenges.

1.4. Ice rises

Ice rises are elevated grounded features that are completely or partially surrounded by ice shelves or ice streams, and they are primarily composed of locally accumulating snow with separate radial ice-flow divides from the main ice sheet. Compared to the surrounding ice shelves, the ice rises are typically several hundred meters higher (King et al., 2004; Drews et al., 2015; Goel et al., 2017; Kausch et al., 2020; Pratap et al., 2022). According to Goel et al. (2022), the 33 ice rises present along the DML coast play a vital role in the region's dynamics and stability. While only four of these ice rises have distinct surface features that suggest long-term stability, however, most of the ice rises in the area undergo ice-dynamical changes (Goel et al., 2020). The central part of the DML coast has undergone a transition from a net mass loss of -27.5 ± 4.5 Gt a^{-1} in 2009 to mass gains of 63.4 ± 9.65 Gt a^{-1} in 2017 over the last few decades (Schröder et al., 2019). Several anomalous snowfall events during this period have primarily contributed to these mass gains (Boening et al., 2012; Lenaerts et al., 2013; Rignot et al., 2019).

A recent study by (Diener et al., 2021 Schröder et al., 2019) has highlighted a strong association between mass balance shifts in DML and surface mass balance (SMB) in the past two decades. Although DML ice rises are exposed to comparable oceanic and atmospheric stimuli, varied response periods and intricate interactions between the ice shelves, ice rises, and the ice sheet can result in different local mass balances over ice rises (Smith et al., 2020; Hogg et al., 2021). Although ice-flow modelling has been employed to determine the mass balance and ice flow history of several ice rises over centennial and millennial time scales

(Kingslake et al., 2014; Drews et al., 2015; Goel et al., 2017), ascertaining short-term mass balances over ice rises remains a challenge (Goel et al., 2020).

Ice rise ice flow can vary from outward radiating streamlines originating from the summit of a dome-shaped ice rise to near-parallel streamlines over an ice rise with a distinctive ridge (Matsuoka et al., 2015). The primary source of mass input for an ice rise is the net surface mass balance (SMB), which is restricted to the local accumulation of snow on the ice rise (King et al., 2004; Drews et al., 2015; Goel et al., 2017; Kausch et al., 2020; Pratap et al., 2022). This distribution is the result of orographic precipitation over these characteristics, with several factors influencing the final SMB pattern, including the ice rise's size and morphology relative to the prevailing winds and the distance from the precipitation source (Lenaerts et al., 2014).

According to MacAyeal et al. (1987), the morphology of an ice rise and the flow regime of the surrounding ice shelf are closely related to its ice flow and surface mass balance (SMB). Hence, changes in the SMB of ice rises can serve as indicators of past and ongoing variations in regional climate and ice dynamics. Bindschadler et al. (1989) also suggest that the flow divide or centre of an ice rise is a prime location for extracting ice cores to study the coastal Antarctic climate, owing to high local snow accumulation and negligible horizontal ice flow. Furthermore, due to their close proximity to the open ocean and high snow accumulation rates, these sites are ideal for reconstructing the maritime history of the region over timescales ranging from decades to millennia.

Therefore, in this doctoral study, the climatic history of two ice rises in the Dronning Maud Land coast was studied using shallow ice cores. The ice cores were analysed for water stable isotopes and major ions, and line-scanned to retrieve visual stratigraphy and melt records. The records are then combined to obtain a robust chronology for the ice cores, which is then used to reconstruct snow accumulation rates and summertime melt variability in the region. Further, the ice core timescales are combined with shallow radar surveys to understand the surface mass balance history over the two ice rises. Efforts are also made to understand the role of atmospheric and maritime factors influencing the ice core records.

1.5. Objectives of the study

The objectives of this doctoral study are as follows:

I. To establish visual stratigraphy techniques to identify annual cycles or melt layers in ice cores and utilise this method for establishing chronology for coastal Antarctic sites.

II. To study the melt layer records of ice cores from coastal ice rises of Dronning Maud Land (East Antarctica) as a potential proxy for climate reconstruction through integration with radar data and established proxy records.

III. To reconstruct the maritime climate variability of East Antarctica during the last few centuries and its linkages to the regional and global climatic fluctuations.

1.6. Outline of the thesis

The thesis comprises six chapters, and the brief content of each chapter is as follows:

Chapter 1 describes the importance and significance of the proposed work. The chapter also briefly introduces the Antarctic climate system, followed by an overview of ice core proxies and timescale construction techniques and their relevant climatic information. The role of ice rises and their significance as an important ice coring site is also highlighted in this chapter.

Chapter 2 provides a detailed overview of the study region (Dronning Maud Land coast in East Antarctica) and its importance for paleoclimatic reconstructions. This chapter also describes the theoretical and experimental basis for the thesis. A detailed description of ice/snow core processing (cutting and sub-sampling) is provided in this chapter. Further, the analytical techniques used for line scanning, stable isotope and major ion measurements are described in detail. The chapter also details the post-processing of the ice core records and techniques used for timescale construction. Additionally, this chapter covers the supporting data sources, statistical methods, and toolbox used in this study.

Chapter 3 focuses on establishing a technique to use line scan images to obtain chronology in the firn section of an ice core and an improved methodology for extracting high-resolution melt records from the line scan images.

Chapter 4 uses a multiproxy approach by using visual stratigraphy (method from chapter 3), water stable isotopes and major ions to establish the chronology of the ice cores and then understand the influence of different atmospheric and oceanic processes in

controlling the stable isotope and snow accumulation variability over the study area. This chapter provides one of the region's longest snow accumulation variability records.

Chapter 5 of the thesis uses ground penetrating radar survey and the ice core information to reconstruct the surface mass balance of the two ice rises from the region for the last three decades. This chapter provides an overview of temporal as well as the spatial variability of surface mass balance over the ice rises. This chapter also provides a record of annual summertime melt variability in the study area by extracting high-resolution melt reconstruction from line scan images. The role of various atmospheric factors in controlling the summertime melt is discussed in this chapter.

Chapter 6 summarises the principal conclusions drawn from this thesis work. Furthermore, this chapter briefly outlines future research/study scope.

Chapter 2

Materials and methods

Ice sheets, like those found in present-day Antarctica and Greenland, require several thousand years to grow to their enormous sizes (Kageyama et al., 2004; Garbe, 2020). These ice sheets form in regions where accumulated snow has undergone compaction, transforming into thick ice layers that can reach several kilometers in depth. Under such conditions, the ice flows slowly under its own weight through pure deformation (Cuffey and Paterson, 2010). Over geological time scales, changes in the extent and topography of ice sheets can significantly influence atmospheric circulation, altering weather systems and their connections to other circulation patterns globally (Löfverström et al., 2014; Jones et al., 2021).

Understanding the mass balance and evolution of coastal regions is essential for comprehending Antarctic contributions to global sea-level changes. Ice rises and rumples, which are locally grounded features in ice shelves, play a vital role in the stability of the ice sheet and its contribution to sea level. Ice rises, rising several hundred meters above the surrounding ice shelf, contain valuable climatic history dating back thousands of years. The largely unexplored Dronning Maud Land (DML) coast in East Antarctica features a chain of small ice shelves connected to ice rises with distinct environmental settings, indicating different responses to ongoing climate change. To gain a detailed understanding of ice shelves and ice rises in coastal Dronning Maud Land, the Indo-Norwegian project MADICE (Mass balance, dynamics, and climate of the central Dronning Maud Land coast, East Antarctica) was launched in 2016. The project is a collaborative effort between scientists from the National Centre for Polar and Ocean Research (NCPOR) and the Norwegian Polar Institute (NPI). It investigates ice dynamics, current and past changes in atmospheric and sea ice dynamics along the central DML coast using remote sensing data, geophysical field measurements, and ice core-based climate reconstructions. The ice cores and radar data used in this doctoral work were collected through the MADICE project.

2.1. The study area

DML is situated in East Antarctica, adjacent to the South Atlantic Ocean, and spans between the meridians 20°W and 44°E, with its southern boundary being uncertain. The coastal region covers approximately 2.5 x 10^6 km^2 and extends from the ice shelf edge to the

southern mountain ridges, positioned 200 – 350 km southwards, effectively separating the area from the inland regions. The complex topography of DML also influences the local climate. The coastal region of DML is located at < 500 m a.s.l. and is highly exposed to weather systems (Altnau et al., 2015), while the escarpment acts as an orographic barrier, creating much drier and more stable conditions over the polar plateau (> 2000 m a.s.l.). DML coast is characterized by the presence of various ice rises and ice shelves, which contribute to ice sheet stability through a buttressing effect (Goel et al., 2020). These ice shelves, though relatively small, extend near or beyond the continental shelf break. The ice rises fringing the ice shelves, having their own flow, also act like miniature ice sheets (Figure 2.1; Matsuoka et al. (2015)).

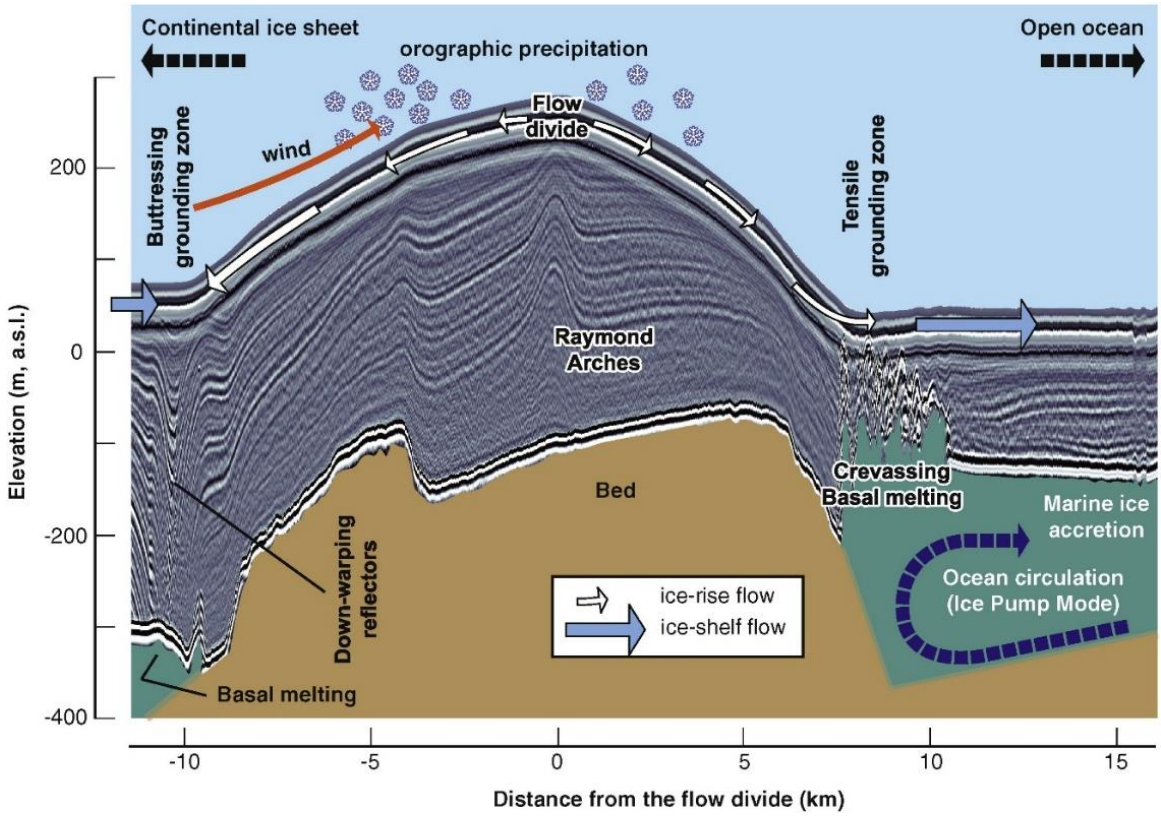

Figure 2.1 Cross section of an ice rise (Matsuoka et al., 2015).

Based on satellite data in Dronning Maud Land, the melt rates in the region vary from nearly 0 to 7 meters per year between 2003 and 2008 (Rignot et al., 2013). The area's interior is partially segregated by tall mountains, leading to steep ice surface gradients from the continental plateau towards the coastal regions (Howat et al., 2019). The Nivlisen ice shelf's drainage basin, which includes grounded ice draining to the ice shelf, has the potential to raise global sea levels by 8 cm (Rignot et al., 2019). It forms a closed embayment between

two larger promontory-type ice rises, Djupranen and Leningradkollen. The region experiences moisture and precipitation from an easterly wind flow, which is mostly sourced from the Atlantic sector of the Southern Ocean and transported through the westerly circulation. However, the elevated topography alters the accumulation rate and snowfall distribution spatially, resulting in significant precipitation on the upwind sides (Lenaerts et al., 2013).

This doctoral work focuses on two ice rises, Leningradkollen (LIR; east) and Djupranen (DIR; west). DIR is the larger of the two, with a surface elevation of 325 meters and a surface area of 731 km^2. It has a ridge extending from the ice sheet to a saddle before rising into a seaward ice rise. LIR, on the other hand, has a lower surface elevation of 174 meters and a net surface area of 375 km^2. Structurally, LIR is similar to DIR, with a smaller ridge extending from the ice sheet and a saddle. However, the seaward dome has another ridge extending west, making the topography more complex than DIR. Both ice rises are located at the calving front and exhibit an upwind-downwind contrast with corresponding high-low surface mass balance (SMB), with DIR showing a higher SMB and stronger contrast than LIR. Additionally, DIR has two quasi-parallel lineations near the ice-flow divide, suggesting long-term stability of the divide position for approximately 2400 years. In contrast, LIR does not have visible lineations in satellite imagery, indicating that its divide position is less sustainable and may have migrated in the past 1800 years. However, it is still unclear whether both ice rises have thickened or thinned on longer timescales when their divide positions were stable and whether their divides have migrated in the past centuries, during which the surface topography could not readily respond to new conditions.

Recent geodetic mass balance measurements using satellite altimetry data (Goel et al., 2022) have shown that DIR experienced significant thickening (0.04 – 0.09 meters ice equivalent per year) from 2003 to 2012, followed by subsequent thinning. On the other hand, LIR remained in balance (-0.02 – 0.02 meters ice equivalent per year) throughout the entire period. This decreasing trend in mass balance aligns with the decreasing SMB in the respective regions, suggesting that SMB plays a crucial role in the observed mass balance changes. Therefore, to gain a better understanding of the stability of these ice rises and the influence of local and regional climatic processes, it is essential to examine the long-term SMB and snow accumulation rate variability, which constitutes the major component of SMB variability, for these ice rises.

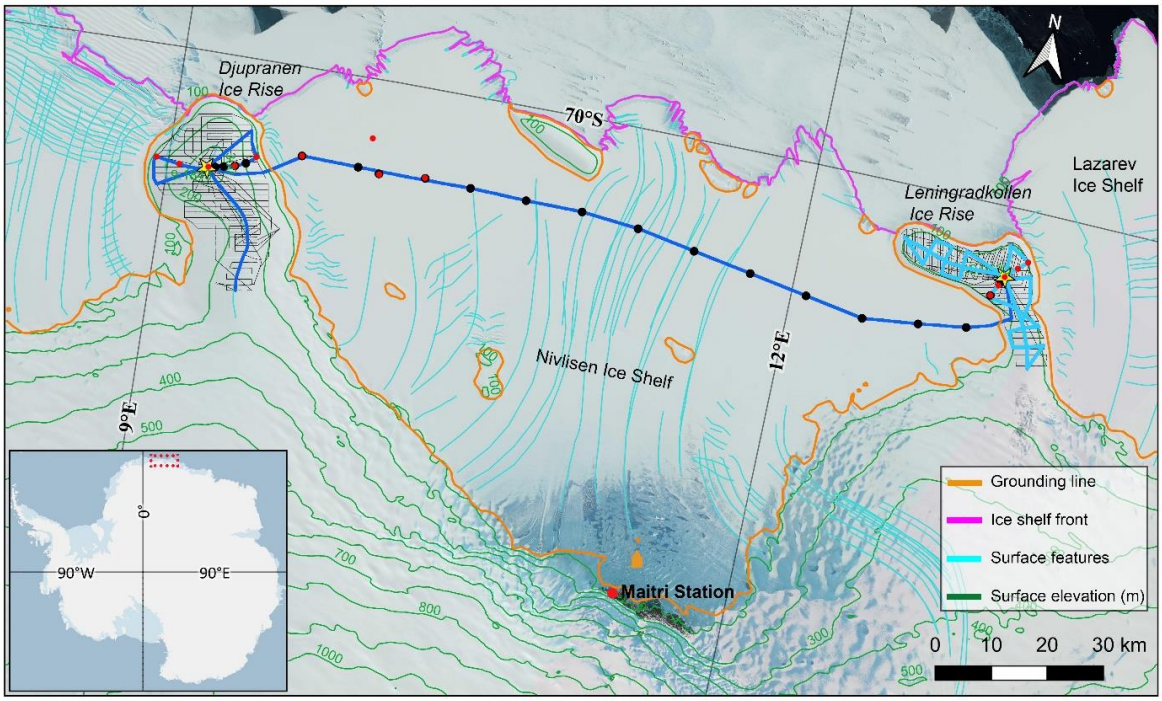

Figure 2.2 The location of the main map is shown in the inset. Shallow radar profiles (light blue, 2016/17 and blue, 2017/18) connect to the two ice-core sites at the summits (yellow stars) of the Leningradkollen and Djupranen ice rises. The radar profiles over the ice rises are only used in this study. The background image is the Landsat Image Mosaic of Antarctica (Bindschadler et al., 2008), with grounding line (Mouginot et al., 2017), ice shelf fronts and ice surface features (Goel et al., 2020), and surface elevation (m a.s.l) contours over the grounded ice (Howat et al., 2019). Coordinate reference system: WGS84 Antarctic polar stereographic parallel to 71˚S (EPSG:3031).

2.2. Kinematic GNSS survey for topography

As part of the MADICE project, differential kinematic Global Navigation Satellite System (GNSS) surveys using Trimble NetR9 dual-frequency receivers were undertaken over the two ice rises to measure their surface topography (Figure 2.2). Two base stations were set up near the ice-coring site at the ice-rise summits. Rover receivers were installed on each snowmobile, moving at a nominal speed of 15 km h^{-1}. The survey was done in a grid pattern with typical spacing between two adjacent profiles of 1 – 2 km. Data were collected at 1-sec intervals, giving the nominal data spacing of about 4 m along the profile. Kinematic baselines between the base station and the rovers were analyzed using Trimble software and the base station positions were fixed with a Canadian precise point-processing service (CSRS-PPP; Natural Resources Canada, 2017). To derive the elevations relative to the mean sea level, EGM2008 geoid model was used (Pavlis et al., 2012).

2.3. Radar profiling and ice coring from cDML

Two major field campaigns of the MADICE project were undertaken in the 2016 – 17 and 2017 – 18 Antarctic field seasons. The team collected geophysical measurements and ice coring to investigate mass balance, dynamics, and climate of an inter-connected system of the grounded features (ice rises) and the Nivlisen and Lazarev ice shelves around India's Maitri Station, central Dronning Maud Land (DML). The details about the radar profiling studies and ice coring are described below.

2.3.1. Radar profiling

Shallow englacial stratigraphy was observed using 250-MHz pulseEKKO ground-penetrating radar (GPR) for ~145 km profile length over the Leningradkollen Ice Rise in 2016/17 austral summer, and ~85 km over the Djupranen Ice Rise and ~161 km over the Nivlisen Ice Shelf in 2017/18 austral summer (Figure 2.2). The radar system was towed behind a snowmobile at a speed of 12 – 15 km h^{-1}. Geographic locations of the GPR data were acquired using a GNSS receiver connected to the system. Radar data were digitized at 0.4 ns intervals over a time window of 500 ns, corresponding to the top ~45 m of the firn with radar velocity of 0.2 m ns^{-1} sampled at about 4 cm depth intervals. Four waveforms were averaged to reduce thermal noise so that the data were recorded with about 1.3 m intervals along the radar profiles. Post-processing to develop radargrams includes a Dewow filter, band-pass filter, and depth-variable gain function (Goel et al., 2017). Radar profiles were made 30 – 100 m away from the ice core sites to prevent radar scatters from the ice-coring set-up.

2.3.2. Ice core drilling

The drill site of the Djupranen ice rise was located at its summit based on the analysis of the satellite altimetry data and satellite image analysis. The ice-penetrating radar survey also revealed Raymond arches, indicative of relatively stable summit position in the past. A drilling camp was set up on 27/11/2016 and the drilling was carried out during the night hours to avoid complications to the drilling process from the increased temperature and solar radiation. The drilling was done using an Electromechanical ice core drilling system (Model D2, GeoTec, Japan). Over the next nine days, a total of 122 m ice core (IND 36/B9; hereafter IND36/9) was retrieved, which was a record length for an Indian ice core. The drilling camp at Leningradkollen ice rise was established on 15/12/2016. The ice core site was selected at

the triple junction of this ice rise, using satellite data. A 50 m ice core (IND 36/B10; hereafter IND36/10) was retrieved from this site. All ice cores were immediately measured after retrieval, packed in HDPE bags, stored in expanded polypropylene (EPP) boxes, and shifted to a reefer container maintained at -20°C, so as to protect the ice cores from the diurnal temperature variations during storage and transportation.

2.3.3. Ice core processing and line scanning

The ice core processing laboratory at NCPOR is maintained at -15°C and equipped with core cutting/sub-sampling facilities for ice cores. A custom-made automated horizontal band saw is used to slice the ice cores into two sections along the c-axis, with one section archived for future work (Figure 2.3c). Another 1.5 cm-thick section is cut along the c-axis from the curved face of the core section, so as to obtain a trapezoidal prism-like structure, with two flat sides along a-axis and two curved sides along b-axis. These 3.5-cm-thick, ~10-cm-wide slabs for line scanning were polished on both sides using a pre-cleaned handheld microtome blade to remove surface undulations resulting from cutting the ice slab using a bandsaw. The ice slabs were then allowed to sit for some time so as to remove any minor undulations on the surface.

The line scanning of the ice core slabs was done using an Intermediate Layer Core Scanner (ILCS), which is designed to perform a transect of a planar ice core at a predetermined depth, providing an intermediate layer scan of the ice core (Krischke et al., 2015). The ILCS works on the principle of dark field microscopy with two LED line illumination sources of wavelength 640 ± 20 nm. Dark field is a method of illuminating a sample with an oblique light source so that the camera only records the light scattered through the sample. The direct light from the light source falls outside the camera's field of view and, therefore, does not appear in the image, resulting in a dark, almost black background with bright objects. The two illumination sources are placed below the polished ice core slab at an incident angle of 45°, and the camera is placed above the sample to measure obliquely-forward scattering (Figure 2.3b). Areas of the ice core with a high concentration of micro-inclusions will scatter more light and be recorded as bright bands, whereas areas of clear ice like melt layers would appear dark. While the core sample was fixed, the 2048-pixel monochrome 8-bit line scan camera and light sources were moved synchronously along the ice core using a computer-controlled motorised unit. The maximum scan length is 1200 mm with a single scan and 1700 mm with two overlapping scans, having

a scan width of 105 mm and an effective resolution of 51 µm/pixel. The length of the overlapping scans is restricted to the length of the ice core tray (1750 mm). The image data is transferred via a Gigabit Ethernet interface to the SKan-G-ILCS software used for image acquisition and inspection (Krischke et al., 2015).

After line scanning, the core sections were decontaminated by carefully removing the outer layers using microtome blades. The core section is then sub-sampled sections at 5cm resolution for stable isotopes of water (oxygen and hydrogen), trace elements, atmospheric dust, and major ion measurements. The outer section of the sub-samples is used for stable isotopic measurement, whereas the inner sections are used for trace elements, atmospheric dust, and major ion measurement to avoid contamination. The subsamples were sealed in contamination-free LDPE containers for further analysis. The samples for major ion analysis were cut into cuboids; the three dimensions of the samples were measured using a calliper and weighed using a weighing balance. The density for the samples was calculated as mass divided by the volume of each sample. The error in measuring the sample dimensions was ±0.5 mm, while the weighing balance's uncertainty was ±0.1 g for measurements up to 100 g. As a result, the density measurements have a propagated uncertainty of 5%.

2.3.4. Image processing

The monochrome line-scan camera records 8-bit greyscale images of the ice core section (Figure 2.4a). The intensity of the scattered light, recorded as pixel intensity values with the 8-bit resolution, ranges from 0 (black) to 255 (white, saturated). Theoretically, the pixel intensity value of a section of clear ice should be zero, which is rarely observed in our study. All image processing was done using MATLAB (version 2018a, The MathWorks, Inc., Natick, Massachusetts, United States), as summarised below. To remove the image section outside the core sample, first a value of 255 is assigned to pixels with a value greater than half of the mean value of all pixels in the image (Figure 2.4b). A 7x7 structural element was then used to erode and subsequently dilate the greyscale image morphologically. This greyscale image was then converted to a binary image, and the holes were flood-filled. A 250-pixel disc structuring element was then used to erode morphologically and then dilate the binary image, to remove any objects smaller than 250 pixels in width, resulting in a mask of the ice core section (Figure 2.4c). Finally, the central 7-cm-wide section of the sample object was extracted (Figure 2.4d). The image contrast was enhanced using contrast limited adaptive histogram equalisation (CLAHE) with exponential distribution (Figure 2.4e). The

CLAHE is a variant of adaptive histogram equalisation in which contrast amplification is limited to reduce problems of noise amplification (Magudeeswaran and Singh, 2017). Breaks in the ice core sometimes appear as saturated pixels, and these regions were excluded from further analysis. A total of 1.5% of the total ice core length was thus excluded. The arithmetic mean of grey values along the width of the core sections is used as a parameter for further analysis.

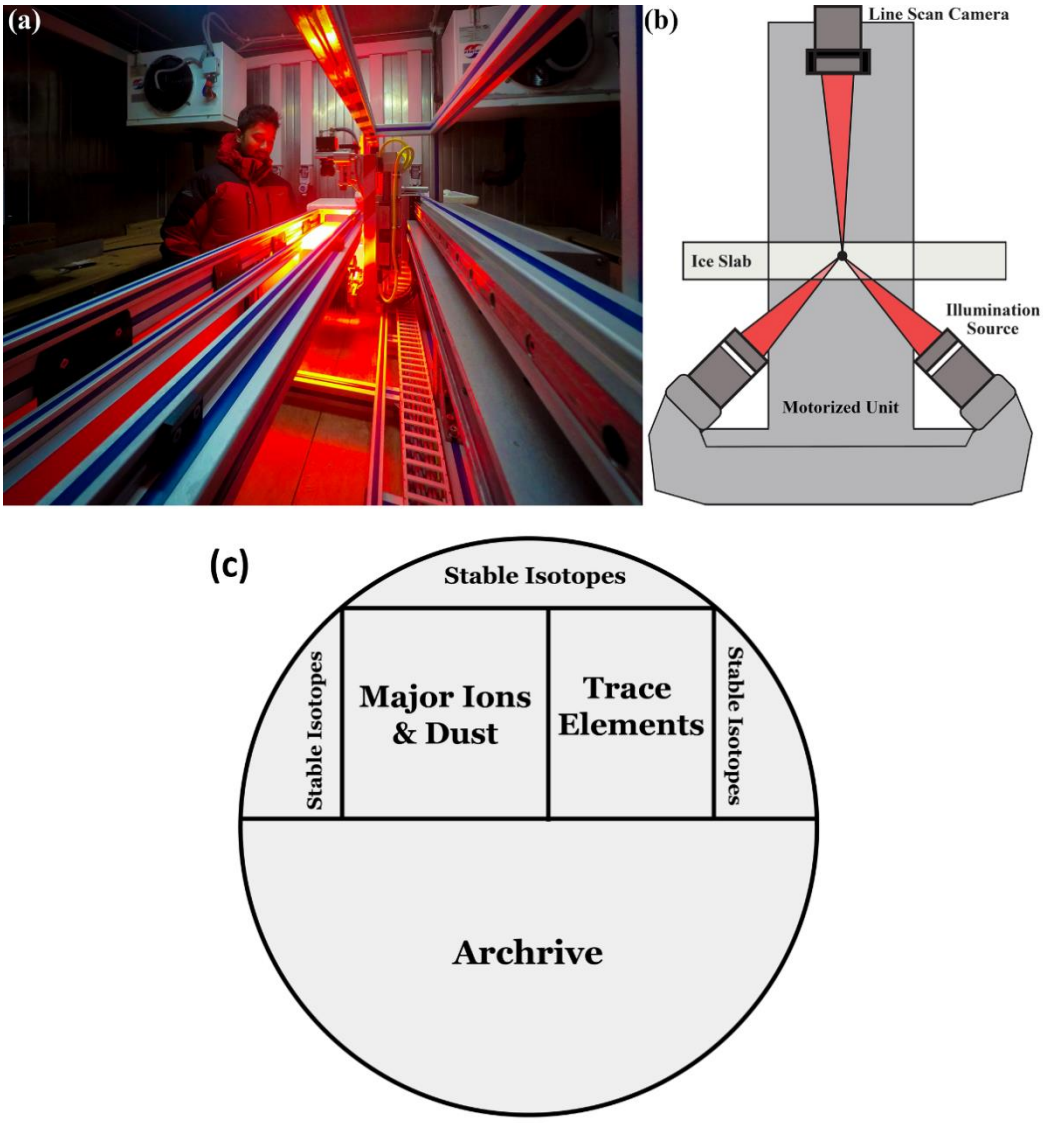

Figure 2.3 (a). The ILCS line scanning setup at the Ice Core Lab of National Centre for Polar and Ocean Research. The bright object in front of the person is the ice core being scanned. **(b).** Schematic cross-sectional representation of ILCS imaging technique. The line scan camera above the ice slab moves synchronously (perpendicular to the page) with the two line-LED illumination sources mounted below the slab at an incident angle of 45°. **(c)** Typical ice core sub-sampling plan.

A continuous VS profile was merged for the total length of the ice cores. Considering the sub-millimetre-scale (51µm/pixel) scanning of ILCS, the VS profiles has the potential to provide an extremely detailed record of snow accumulation and sea salt inclusions. Due to the inherent noise involved in such ultra-high-resolution data of line scanning and to make it comparable with the $\delta^{18}O$ records, the VS profiles were downsampled at 5 cm resolution by calculating the mean of greyscale values for every 5 cm intervals at which discrete isotopic and chemical analysis were performed. This enabled us to enhance the signal-to-noise ratio and to improve confidence in annual layer counting.

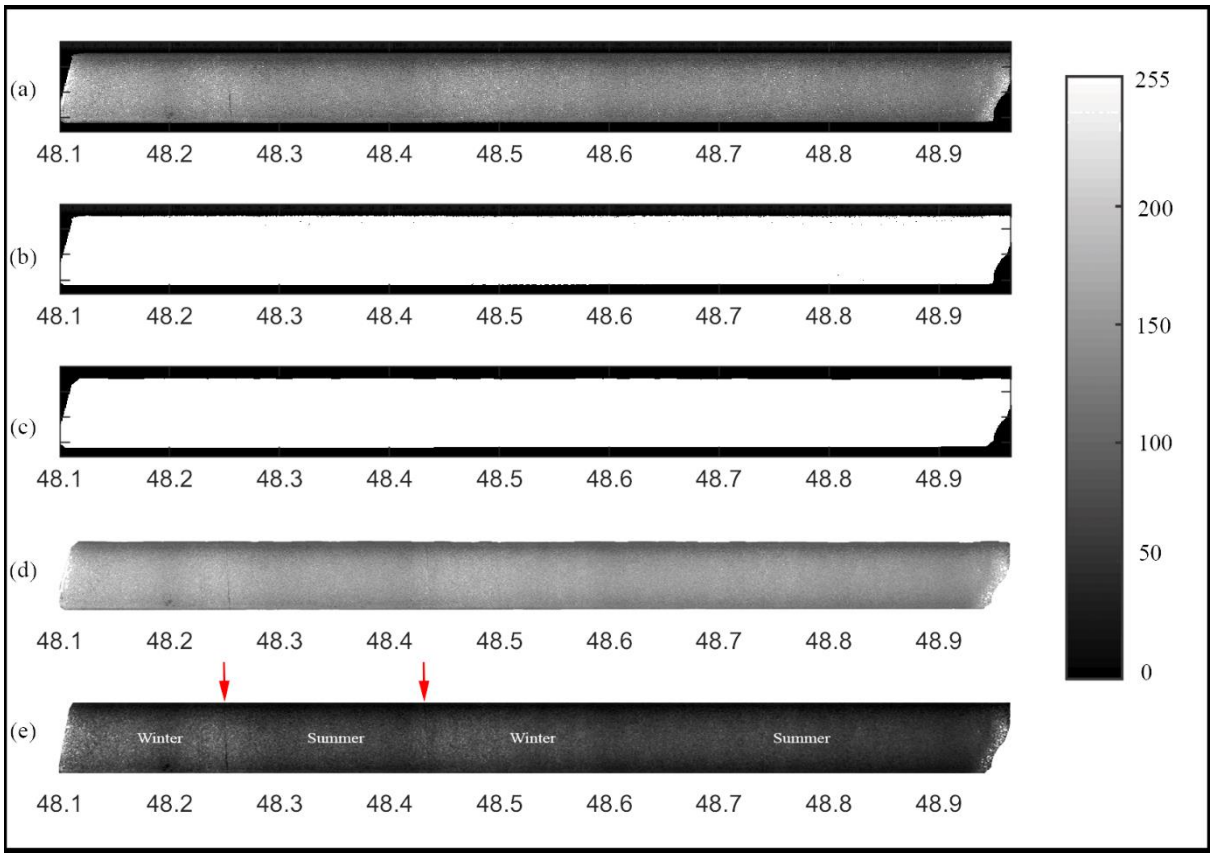

Figure 2.4 Line scan image processing steps from the raw image **(a)** to the final image **(e)** presented for a core sample from 48.1 to 48.97 m depth. The contrast of the final image is exaggerated to make the annual layer visible, and the approximate seasonal positions are labelled. The core section is 86 cm long and 10 cm wide. The identical greyscale is used for all panels. See text for image processing procedures corresponding to individual panels. Two minor melt layers are identified in **(e)** and indicated with red arrows.

2.3.5. Core Breaks

Core breaks impact the accurate counting of melt layers and lenses within ice cores. These breaks are fractures that occur for two main reasons: first, when the ice core is freed at the bottom of the borehole during drilling operations (Westhoff et al., 2020), and second, due to fractures in the brittle-zone ice (Neff, 2014). In our study, all core breaks are associated with the former reason. Drilling-related core breaks typically exhibit an approximately horizontal orientation. The frequency of core breaks depends on the smoothness of the drilling process and the quality of the ice. In favourable conditions with good ice quality, core breaks are observed at intervals of a few meters, which correlates with the length of the core barrel chamber utilized in the drilling system.

During line scanning, light is directed at an angle from beneath the core slab. Core breaks are characterized by rough break-surfaces, with a gap in between and another rough break-surface. As a result, when light passes through the void created by the core break, the intensity of light diminishes, leading to the casting of shadows on either side of the core break. Simultaneously, the edges of the core break become excessively bright due to this intensity loss. The appearance of these shadows can be misleading, and they may be mistakenly identified as melt layers. This issue becomes particularly problematic when a melt layer is situated in close proximity to a core break. However, there is a key distinction between the two: a core break casts a shadow on the edge of the core slab, while the edge remains consistently bright in the presence of a melt layer. To address this challenge, a methodology is established to disregard features in close proximity to core breaks and the edges of the images during analysis. This approach is necessary to avoid misinterpretations. However, it also implies that as the number of core breaks increases, the likelihood of overlooking bubble-free events, and consequently underestimating their count, becomes more significant. Hence, core breaks can introduce bias in the estimation of event occurrences.

2.3.6. Major Ions

Major inorganic anions (Cl^-, SO_4^{2-}, MSA^- and NO_3^-) and cations (Na^+, NH_4^+, K^+, Mg^{2+}, and Ca^{2+}) were measured in the samples using ICS 5000+ ion chromatograph (Thermo Dionex; Figure 2.5) equipped with a conductivity detector. Anions were separated on an AS11 (2 mm) column with potassium hydroxide as eluent and an AG11 (2 mm) guard column with AERS 500, 2 mm suppressor. Cations were separated on CS17 (0.4 mm)

capillary column with methane sulphonic acid as the eluent and the CG17 (0.4 mm) capillary guard column with CCES 300 capillary suppressor. 10 mg/l stock solution of Na^+, NH_4^+, K^+, Ca^{2+} and Mg^{2+} were mixed and then diluted with MiliQ ultrapure water to make standards for cation exchange chromatography; the anion standards were made from 10 ppm stock solutions of MSA^-, Cl^-, SO_4^{2-} & NO_3^-. The dilutions were conducted volumetrically and were freshly prepared within few days of each run and ranged from 5 ppb to 1 ppm. Eight standards were selected from this range for calibration. Before analysis, frozen ice core samples were melted in a Class-100 clean room. Detection limits achieved for the ions Na^+, K^+, Cl^-, SO_4^{2-}, and NO_3^- were 5 ppb and for Ca^{2+} and Mg^{2+} were 8 ppb. Analytical precision for all the ions was better than 10 %.

Figure 2.5 Dionex ICS5000 ion chromatograph (IC) used for the measurement of major ion composition in ice cores samples. The IC is housed in a class 100 clean room in NCPOR.

2.3.7. Stable Isotopes

Traditional water isotope analysis performed using IRMS technology requires extensive sample preparation and a skilled, experienced operator. Further, oxygen and hydrogen ratios are separately processed. Recent advances, like the cavity-enhanced laser absorption technique, measure all three isotopes simultaneously, directly from water-based samples. Accordingly, all ice core samples were analyzed for oxygen and hydrogen isotopic

ratios at NCPOR using Triple Isotope Water Analyzer (TIWA-45EP from Los Gatos Research, USA), which works on the principle of off-axis integrated cavity output spectroscopy (OA-ICOS; Figure 2.6). This instrument can simultaneously report all the stable isotopes of water (δ^2H, $\delta^{17}O$, $\delta^{18}O$). These isotopic ratios are further used to derive the second-order proxy, d-excess. The melted ice core samples were introduced in TIWA-45EP without sample conversion through PAL, HTC-xt auto-injector (CTC Analytics) equipped with a heated (≈85 °C) injector block (LGR). Using Hamilton 1.2 µL, zero dead volume syringe, samples were injected into the injector block and evaporated for direct isotope analysis. Measurements were completed at a speed of ~90 s per individual injection. To remove the sample-to-sample memory, a total of nine injections were made, in which the first three injections were removed. The last six injections were averaged to produce a single, high-throughput (HT) sample measurement. One commercially available working standard from LGR1C and two in-house laboratory standards (CDML1 and HL1) with known isotopic composition, spanning the entire range of our sample measurements (-46.19 ‰ to -19.49 ‰ for $\delta^{18}O$ and -362.85 ‰ to -154.0 ‰ for δD) were analyzed routinely as reference waters after every five ice core samples to check the instrument performance. Laboratory standards are calibrated on VSMOW/SLAP scale. The external precision obtained using our laboratory standard (CDML1 and HL1) for $\delta^{18}O$ was ± 0.046 ‰ and ± 0.068 ‰, respectively and for δD was ± 0.32 ‰ and ± 0.23 ‰ (n=30, 1σ standard deviation. Replicate analyses performed based on ten samples yield repeatability of ± 0.76 ‰ for δD and ± 0.09 ‰ for $\delta^{18}O$. All the raw instrumental OA-ICOS data were processed in LGR post-analysis software. Any measured injection with water number density outside the manufacturer's suggested range of 2 – 4.5 × 10^{16} H_2O molecules/cm^3 was discarded. Injections with incomplete evaporation were detected by examining the standard deviation of the measured water number density (σ_{nmeas}) as reported by the instrument (Berman et al., 2013). Processed raw data directly gives $\delta^{18}O$ and δD, which are further used to calculate deuterium excess (Dansgaard, 1964).

Figure 2.6 Triple Isotope Water Analyzer (TIWA-45EP) instrument at NCPOR ice core lab facility.

2.3.8. Diffusion correction of isotopic record

Polar ice core water isotope data exhibit inherent smoothing effects due to molecular diffusion processes occurring within the upper 60 – 80 meters of the ice sheet (Johnsen, 1977; Johnsen et al., 2000). The diffusion phenomenon in the firn layer reduces the high-frequency information contained in the ice cores' water-isotope signal. To address this, a parameter known as diffusion length is used to quantify the statistical vertical displacement of water molecules from their original positions (Johnsen, 1977; Johnsen et al., 2000). This parameter depends on various factors, including accumulation rate, temperature, surface pressure, and strain rate at the drilling site. In regions where significant melting does not occur during the summer months, a diffusion correction is conventionally applied to ice cores. This is crucial since seasonal melting can introduce substantial artefacts during the back-diffusion process. For our study, the diffusion-correction methodology developed by the University of Copenhagen (Johnsen et al., 2000) is used. The method employs maximum entropy methods to invert an observed power-density spectrum to determine the diffusive attenuation and correction factors. Importantly, this approach is entirely independent of firn diffusion and densification models. Upon applying the diffusion correction to the isotopic data, slight shifts in depth may occur for the winter minima and summer maxima, which are used to define mid-winter and mid-summer events, respectively, in the diffusion-corrected data compared to the raw isotopic record. This correction process helps enhance the accuracy

of the data (Figure 2.7) and allows for more reliable interpretations of climate and environmental changes based on the ice core records.

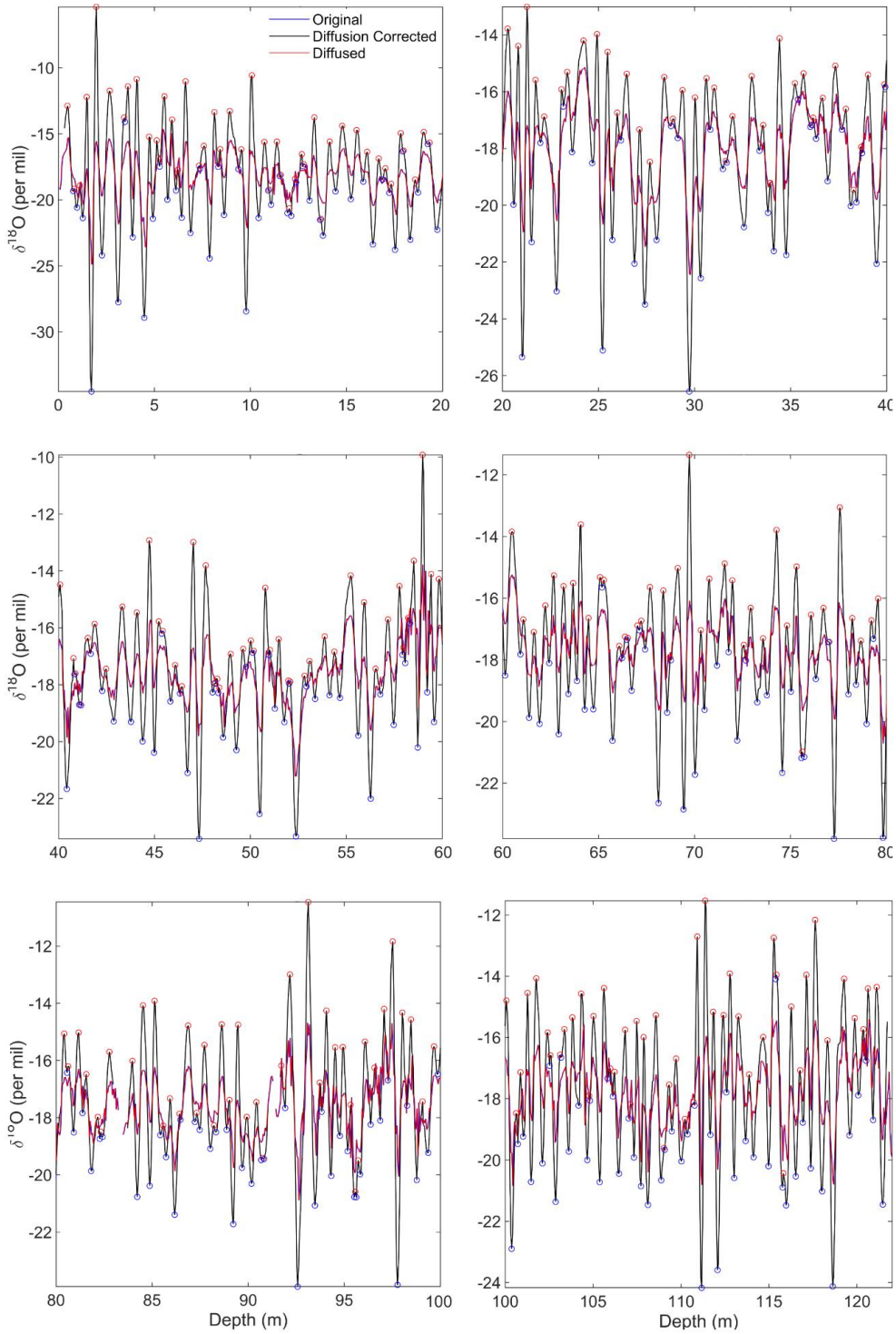

Figure 2.7 Diffusion correction of $d^{18}O$ records (raw: blue curve; corrected: black curve) for the DIR ice core. Algorithmically identified annual maxima(red circle) and minima (blue circle) from the diffusion corrected record.

2.4.Ice core chronology

Various proxies measured in ice cores exhibit seasonal periodicities that have been used to interpret annual layers and, in turn, obtain an age-depth scale for the ice cores. The individual proxies, however, peak in different seasons. Like sea-salt tracer can have their annual maxima in summer or winter months (depending on ice core sites and their proximity to open ocean), dust is usually highest in spring, while organic tracers like ammonium (NH_4^+) reach their maxima during summer months. High-accumulation sites like the ice rises studied in this doctoral work, can therefore be successfully dated using annual layer counting. A multiproxy dating approach, based on manual identification of annual layers in different proxies with strong annual signal is used in this work. The identification of annual layers in this doctoral work is primarily based on the concentration records of $\delta^{18}O$, sea-salt sodium (ssNa), non-sea-salt sulphate ($nssSO_4$), ammonium (NH_4), nitrate (NO_3) and visual stratigraphy (VS).

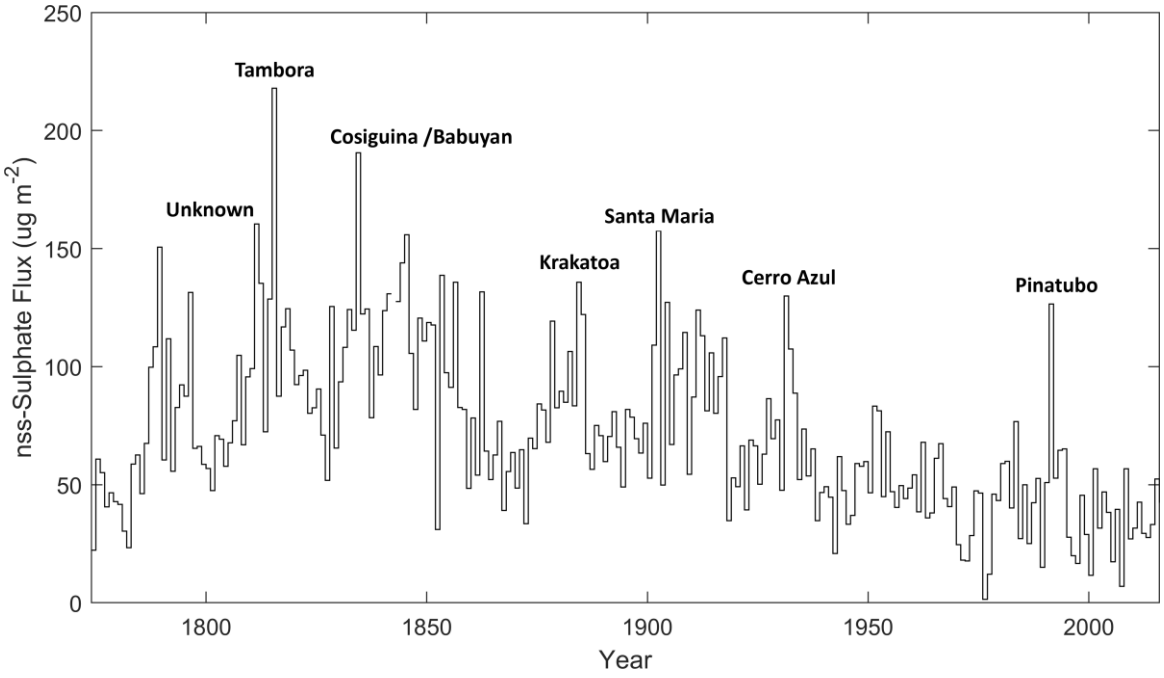

Figure 2.8 Volcanic events identified from the non-sea-salt sulphate flux records of the IND36/9 ice core. Only major volcanic events are marked and further used as time markers for reconstructing the chronology.

In this study, the concentrations of major ions, namely sodium (Na^+) and sulphate(SO_4^{2-}) is used, to estimate the non-sea-salt sulphate [$nssSO_4^{2-} = SO_4^{2-}$ - 0.252*(Na^+)] (Figure 2.8). This estimation served as a marker for historical volcanic eruption events (tie points) in the ice cores, which in turn improved the chronological

constraints of the core samples. To establish an absolute age marker for the ice core sections, the concentrations of tritium (^{3}H) was measured in selected segments (a total of 20 discrete samples) of the IND36/9 ice core. The measurements were performed using an Ultra Low-Level Liquid Scintillation Spectrometer at the National Institute of Hydrology (NIH, Roorkee, India). Analysis of the tritium profile revealed an anomalous peak at approximately 22.25 meters depth. This peak coincided with the well-known tritium peak associated with the "Tsar Bomba," the largest nuclear bomb test conducted in 1961. This peak was previously observed in various tritium records spanning the years 1961 to 1962 (Cauquoin et al., 2016). Taking into account a few months' lag due to long-range transport before registering its signal in the Antarctic snow/ice sheet, the age of this specific layer was assigned as 1962. By combining tie points based on both volcanic events and the nuclear bomb testing event, an independent means is obtained to enhance the accuracy of the ice core chronology and obtain a robust age depth relationship (Figure 2.9).

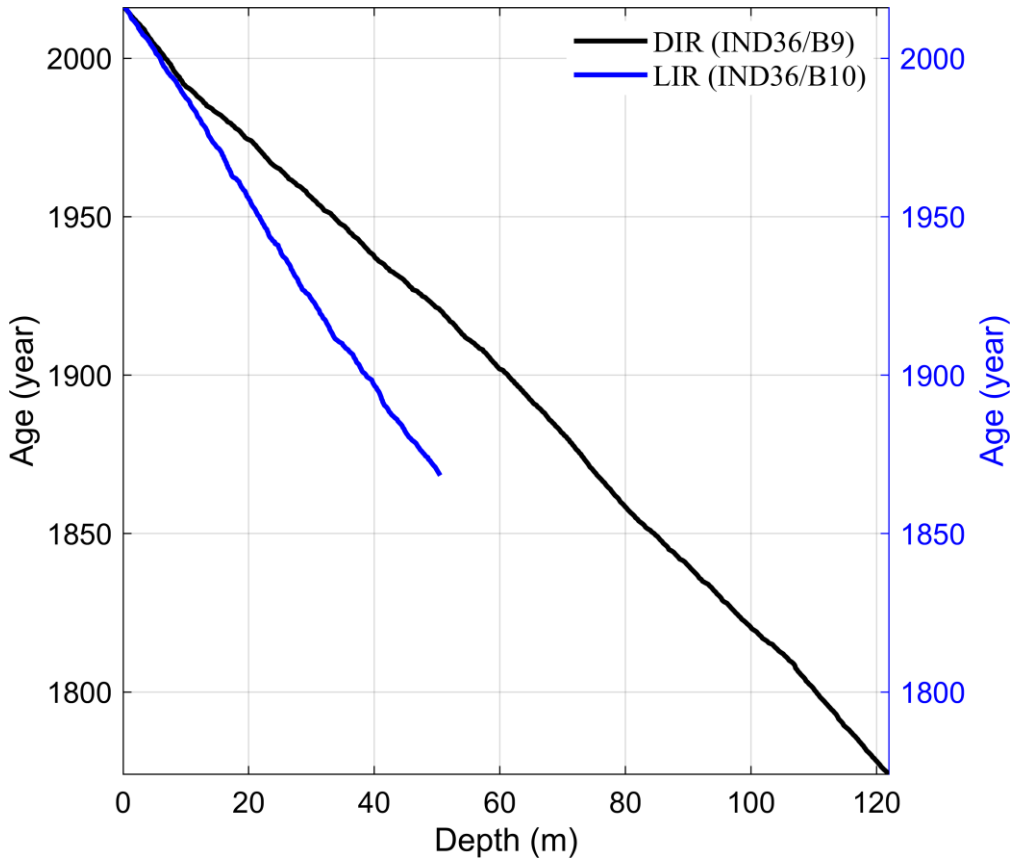

Figure 2.9 Age-depth scale of IND36/9 (black) and IND36/10 (blue) ice core. The larger slope for IND36/10 is due to its lower accumulation rates.

2.5. Surface mass balance estimation

To estimate the spatial and temporal pattern of SMB using the GPR data, five to six prominent reflectors (assumed to be isochrones) are identified and tracked along all the profiles collected over the ice rises and ice shelf individually. The tracked reflector layers were also used as tie-points to later constrain the chronology for the IND36/10 ice core with respect to age-depth relationship of the IND36/9 ice core. The bulk density of the ice cores was used up to a depth of 35 m and varied between 436 and 739 kg m^{-3} (Figure 2.10a,d). To compensate for the snow surface changes between the time of ice coring in 2016/17 and the time of radar data collection in 2017/18 over the ice shelf and Djupranen Ice Rise, surface height difference measured using a snow stake at both the ice core site between 2016/17 and 2017/18 seasons was added to the ice core data, so that radar data over Djupranen Ice Rise and Nivlisen Ice Shelf are referenced to the 2017/18 snow surface. Therefore, the SMB for Leningradkollen Ice Rise is before 2016, and SMB for the Nivlisen Ice Shelf and Djupranen Ice Rise is prior to 2017.

We accounted for depth-variable radio-wave propagation speed (v) using density data measured with the ice cores (Kovacs et al., 1995),

$$v(z) = \frac{c}{1+0.851\rho(z)} \quad (1)$$

where z is the depth, c is the speed of light in a vacuum (0.30 m ns^{-1}), and $\rho(z)$ is a depth-dependent density from the ice core. The measured densities from both the ice cores are in good agreement with the firn densification model (Herron and Langway (1980); Figure 2.10a, d). Assuming that ice core measured densities are horizontally invariable, the Leningradkollen ice core density curve was used (Figure 2.10d - f) to date and calculate mass from reflectors observed over Nivlisen Ice Shelf and Leningradkollen Ice Rise, whereas the Djupranen ice core density curve was used for the reflectors over Djupranen Ice Rise. The effect of different density curves obtained at the core sites is examined in chapter 5.

Each reflector's depth (z) at a given point was estimated from the two-way propagation time $t(z)$ and the depth-dependent propagation speed $v(z)$ obtained with Equation (1):

$$t\,(z) = \int_0^z \frac{2}{v(z)}\,\mathrm{dz}. \quad (2)$$

After converting travel time to depth, mass in each layer bounced by two reflectors is derived using the density curves (Figure 2.10a) and then divided by the age difference between these two reflectors (Waddington et al., 2007). Here, it is assumed that the reflector depths do not change over 30 – 100 m between the core sites and the closest radar data points.

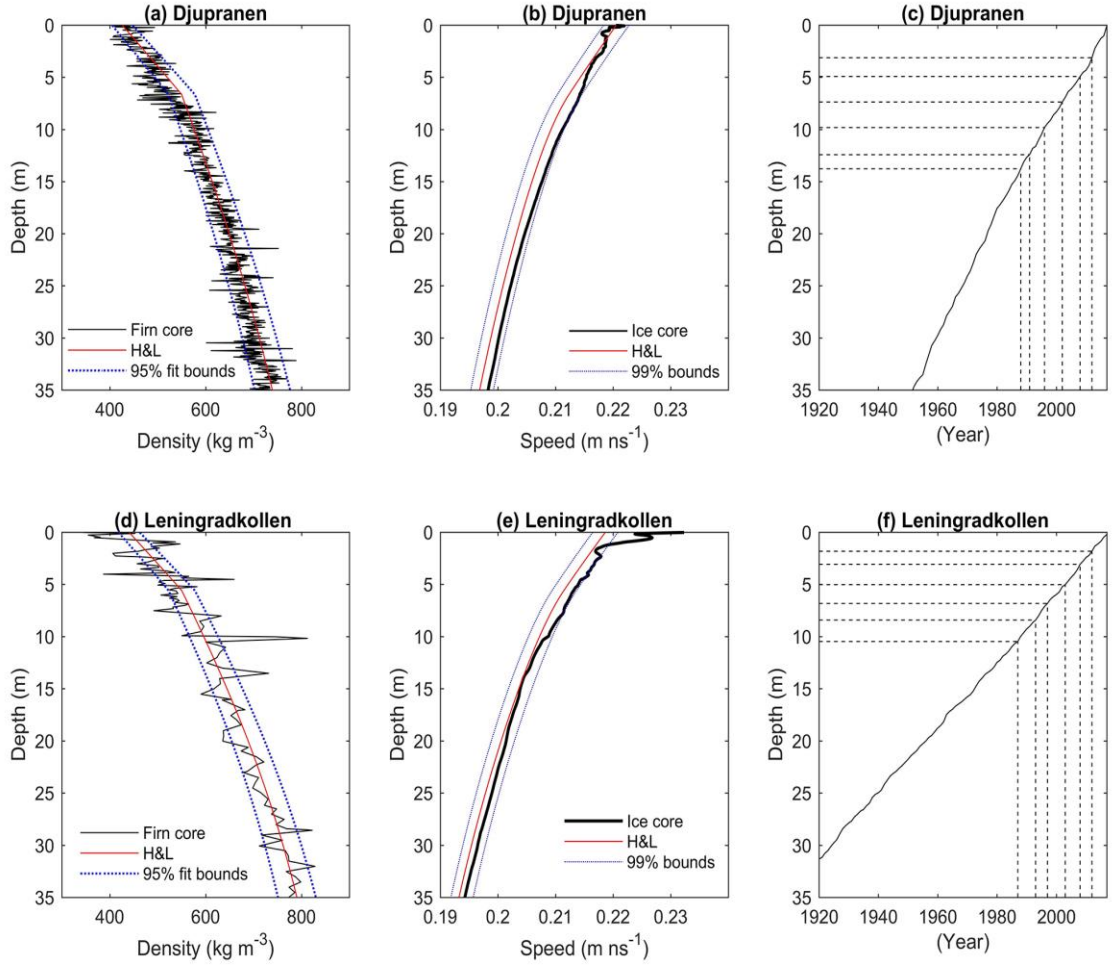

Figure 2.10 Ice core data used to constrain depth and age of radar reflectors, collected at the Djupranen (top row) and Leningradkollen (bottom row) ice rises. (a, d) Depth profile of measured density used to calculate depth profile of radio-wave propagation speed (black) shown in (b, e) as well as from the firn-densification model (Herron and Langway, 1980) constrained with ice-core data. (c, f) Depth profiles of age constrained by ice core data. Dotted lines show the correspondences between depths of six tracked radar reflectors and their ages.

Chapter 3

Application of visual stratigraphy from line scan images to constrain chronology and melt features of a firn core from coastal Antarctica

3.1. Introduction

Polar ice cores can provide annually resolved proxy records of past atmospheric temperature, composition, and circulation changes for thousands of years when instrumental records are not available. Ice core studies have enabled us to better understand human-induced warming on a global scale and the non-linear behaviour of the climate system at multiple timescales. However, the reliability of any paleoclimate data is most dependent on the accuracy of its chronology and constructing a robust age model is essential for interpreting past climatic records from polar ice cores (Legrand and Delmas, 1986; Sinclair et al., 2010). Considering the large spatial variability in Antarctic snowfall, the local estimation of snow accumulation rate is vital for estimates of the coastal Antarctic mass balance (Krinner et al., 2007), assessments of regional climate models, validations of satellite measurements (Stenni et al., 2000; Goursaud et al., 2017) and eventually deciphering interactions between the Antarctic Ice Sheet, atmosphere and ocean (Stenni et al., 2000; Sinclair et al., 2010).

Multiple and complementary methods are often used to establish more reliable ice core chronologies. When chronology for the past few centuries is established in coastal Antarctica, these methods are mainly a combination of annual layer counting, use of time markers and correlation with other dated time series, occasionally complemented with glaciological modelling (Stenni et al., 1999; Zhang et al., 2006; Thamban et al., 2013). High snow accumulation sites in the coastal region offer excellent opportunities to reconstruct sub-annual to annual climatic records by counting annual layers of stable water isotopes (Naik et al., 2010; Thamban et al., 2013; Philippe et al., 2016). However, there are many complicating factors like the damping effect due to diffusion processes during firnification, especially where the snow accumulation rate is lower than 0.2 m w.e. (Johnsen, 1977). More importantly, summer surface melting in coastal Antarctica can also induce post-depositional effects in the stable isotope records. Therefore, a multiproxy approach is preferred for dating an ice core , generally using a combination of stable isotopes and chemistry records. Such an approach has its limitations for coastal sites, which are influenced by storm activities and

summertime melting, making the annual layer counting using stable isotope and chemistry records very complicated.

Visual stratigraphy (VS) obtained by line scan imaging is a commonly acquired information in many ice core studies. Light scattering is caused by micro-inclusions, such as solid particulate matter and firn structure (or air bubbles enclosed in the ice matrix at greater depths), and its characteristics depend on the size and concentration of these inclusions which may change with the seasons, resulting in dark and bright bands. The VS can be acquired using many techniques ranging from simple ocular inspection to digital scanning at high resolution, using a variety of different light sources (Kameda et al., 1995; Alley et al., 1997; Pohjola et al., 2002; Takata et al., 2004; Svensson et al., 2005; McGwire et al., 2008a; Abram et al., 2013a; Morcillo et al., 2020). The high-resolution images obtained using digital scanning can differentiate the annual layers even at depths below bubble hydrate transition zone (Svensson et al., 2005; Svensson et al., 2008; Winstrup et al., 2012). Although VS has been extensively studied in ice cores from the Arctic and a few inland sites of Antarctica, studies from coastal Antarctica are limited. No studies have utilised VS as a proxy for annual layer counting of the firn section of ice cores from coastal Antarctica, where the climatic variability is higher due to the maritime influence and frequent episodes of extreme precipitation events, which in turn results in noise in the proxy records. These sites are also characterised by high accumulation rates and occasional to frequent melt features, which add complexities to the VS record, making it harder to obtain a clear annual signal. While micro-inclusions are the significant source of variability within VS data in deeper core sections, gradual densification processes and summer melting also contribute to VS data changes in the upper firn sections (Sjögren et al., 2007; Kinnard et al., 2008). Summer melting is significant in the coastal regions of Antarctica (Das and Alley, 2005; van den Broeke, 2005; Kaczmarska et al., 2006; Tedesco and Monaghan, 2009). Although there are several uncertainties related to the transport and re-freezing of melt water within the snowpack, the re-frozen ice can be easily differentiated from the surrounding firn and ice in the VS profiles as they appear as dark and transparent layers with few or no bubbles. While surface melting is affected by numerous factors like surface albedo and cloud type, summer temperature is the primary factor responsible for melting the glacial surface (Bertler et al., 2018). Melt layers in ice cores provide a valuable record of the summertime warming trend over recent times (Kaczmarska et al., 2006; Kelsey et al., 2010). Thus, a record of melt history from a coastal site can be a proxy for summer temperature trends in the past and

complement surface air temperature reconstructions using water-stable isotopes. In this study, VS profiles of a high-accumulation firn core from coastal Dronning Maud Land (DML) as studied to assess the suitability of VS method for annual layer counting in the snow and firn sections of coastal Antarctic ice cores.

3.2. Results and Discussion

3.2.1. Preliminary chronology and age constraints

A preliminary chronology for the IND36/9 ice core was developed using annual layer counting of $\delta^{18}O$ record, using winter troughs in the stable isotope record to identify the potential annual layers (Figure 3.1a). Next, this preliminary chronology was compared with the non-sea-salt sulphate ($nssSO_4^{2-} = SO_4^{2-} - 0.25Na^+$) records of the core to identify the well-known volcanic eruption events. The $\delta^{18}O$ measurements were made using a Triple Isotope Water Analyzer (TIWA-45EP, Los Gatos Research), with an external precision of ±0.1‰ (1σ), while ionic concentrations were measured using an ion-exchange chromatograph (Dionex ICS-5000) according to the method detailed by (Thamban et al., 2010).

Identification of volcanic eruptions with absolute certainty in ice cores from coastal regions is challenging due to the highly variable $nssSO_4^{2-}$ background signals attributed to the presence of a natural background caused by marine biogenic sulphur deposition (Philippe et al., 2016). To separate this natural background, the detection threshold method by Sigl et al. (2013) is used with a 100 sample running median (RM) and median absolute deviation (MAD) of the whole record (Figure 3.1b). RM and MAD are considered a robust measure of natural background as they are not strongly affected by the presence of outliers, as compared to mean and standard deviation. The detection threshold is thus defined as the sum of RM and three times MAD, and any $nssSO_4^{2-}$value exceeding this threshold is considered a potential volcanic eruption peak. While multiple values exceeding this threshold were observed in the core, only four volcanic marker events that are extensively reported in Antarctic ice cores were used. Accordingly, the $nssSO_4^{2-}$ anomaly peaks related to Pinatubo/Cerro Hudson (1991), El Chichón (1982), Agung (1963) and Cerro Azul (1932) volcanic eruptions were identified in the top 50 m of the ice core (Figure 3.1b). Previous studies have shown that the $nssSO_4^{2-}$ records in ice cores can have a delay of one to two years from the time of the volcanic eruption, but this delay may be different for different volcanic events and core locations (Li et al., 2012; Sigl et al., 2013; Emanuelsson et al.,

2022). To simplify, delay of one year is assumed for all identified volcanic events. To further constrain with an absolute age marker, the tritium concentrations were measured in a selected 12 m section (inset of Figure 3.1b). The tritium profile shows an anomalous peak at 27.25 m depth, coinciding with the well-known tritium anomaly attributed to the atomic bomb testing of Tsar Bomba in 1961 (Cauquoin et al., 2016).

3.2.2. Multiproxy approach and chronology validation

Three additional ionic records (ssNa$^+$, NO_3^- and NH_4^+) were used together with nssSO_4^{2-} and $\delta^{18}O$ records to refine the chronology between the volcanic and tritium tie points (Figure 3.1c). A multiproxy approach is needed because the climatic conditions in the coastal Antarctic sites are highly variable with the snowfall influenced by extreme precipitation events (Turner et al., 2019) and repeated occurrence of summertime melting (Lenaerts et al., 2016), which can disturb the annual signals in $\delta^{18}O$ records. Moreover, firn diffusion can also lead to smoothening of weak annual signals in stable isotope records. We, therefore, used multiple chemical proxy records for annual layer counting to account for the high degree of variability. Winters can be identified with more negative stable isotope values and low concentration of nssSO_4^{2-}, ssNa$^+$, NO_3^- and NH_4^+, and annual layers were marked as concurrent winter troughs.

To ascertain the robustness of the chronology, the StratiCounter program (Winstrup et al., 2012) is used using multiple proxies for the IND36/9 ice core. StratiCounter works on the statistical framework of Hidden Markov Models and the Expectation-Maximization algorithm, to automatically recognise annual layers in paleoclimate archives. It requires training data and user-defined annual layer counts. The StratiCounter chronology is constrained using volcanic events and the tritium anomaly identified in Figure 3.1b. These manual counts are used to provide a generalised framework. StratiCounter uses this generalised template for annual layers and applies an expectation-maximization algorithm to continuously update and refine the statistical description of an annual layer, which in turn allows for changes in layer characteristics with depth (Winstrup et al., 2012). To further decrease the dependence of StratiCounter on the initial manual counts, the program is re-run using an improved layer template derived from the algorithm output. Matching the volcanic events and tritium anomaly with the final chronology gives an estimated age error of ±2 years for the past century (supplementary Table ST1).

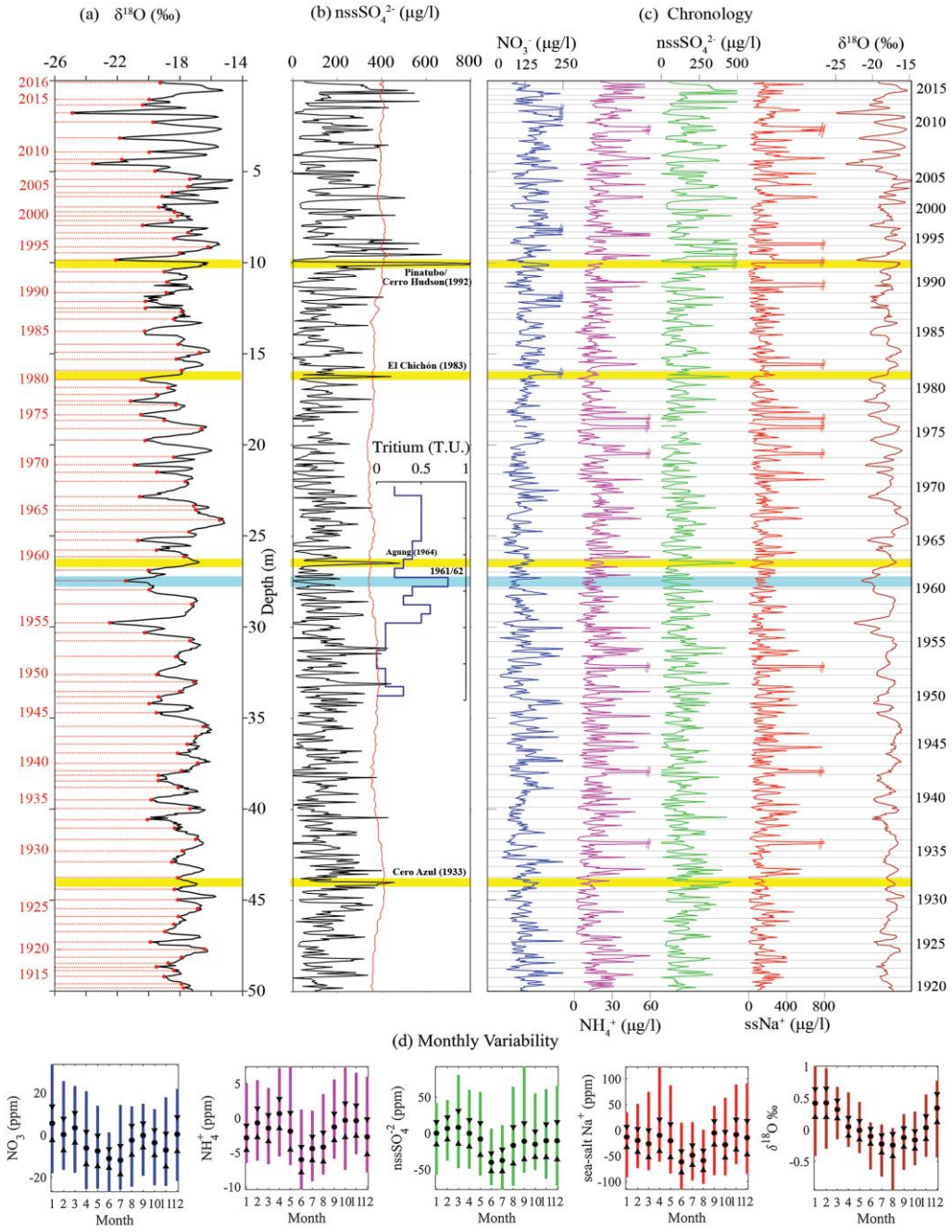

Figure 3.1 Establishment of chronology for IND36/9 core using multiple proxies. **(a)** A preliminary age model using $\delta^{18}O$ records. Annual layers based on the winter minima of the $\delta^{18}O$ record are marked with red dots and dotted red lines. **(b)** Measured $nssSO_4^{2-}$ records (black) exceeding the detection threshold (red curve) are considered potential volcanic events. Identified volcanic peaks (yellow bands and ages) and the tritium anomaly attributed to the atomic bomb testing of 1961 (blue band) were used as age tie points to constrain the chronology. The final chronology **(c)** is obtained by annual layer counting, taking into account the seasonal variability in $\delta^{18}O$, ssNa+, $nssSO_4^{2-}$, NO_3^- and NH_4^+. Grey bars represent the annual layers from StratiCounter. Note that the y-axes of the chemistry records have been cropped to show maximum variability and the cropped peaks are marked with breaks to differentiate them from missing data points. **(d)** Seasonality of chemical proxies and $\delta^{18}O$

for the whole studied section. The black dot shows the median and the black triangles show the 95% confidence interval of the median. Vertical bars show the interquartile range.

We then use this chronology to examine the seasonality of the proxies (Figure 3.1d). Anomalies of each month's value from the annual mean value is calculated. This is repeated for all the proxies for the period 1919–2016 (Figure 3.1d). Since the sampling resolution in the time domain is highly variable and identifying monthly separation in proxy data is debatable, monthly resolution is not claimed, but the median of all monthly values should represent the seasonality of the proxies. The troughs in the $\delta^{18}O$ record typically correspond to the troughs in most chemical species studied here. Although a high degree of variability is observed in the chemical species due to the close proximity of the core site to the open ocean, they are not biannual in nature.

While the accumulation history of the core site is outside the scope of this manuscript, several anomalously thick and sometimes thin annual layers were observed. This is possibly due to the highly variable precipitation regime of coastal DML, which has been observed to result in anomalous snowfall events, like in the year 2009, which was recorded both using satellite records (Boening et al., 2012) as well as station-based observations (Gorodetskaya et al., 2013). Regional climate models like RACMO2 also captured this event in their simulations(Lenaerts et al., 2013). A similar degree of variability in snow accumulation record from an ice core has also been observed at a nearby site in Fimbul Ice Shelf (Kaczmarska et al., 2004), with accumulation rates varying between 0.08 and 0.58 m w.e during 1737 – 2000.

3.2.3. Melt layer quantification and masking

Previous studies have used the melt layer's maximum thickness to calculate the total melt proportion in ice cores (Kaczmarska et al., 2006; Kinnard et al., 2008; Bertler et al., 2018). While this method may work well to understand the temporal variability of annual melt, it is prone to over-estimation of the melt proportion. In this study, a different approach is used by manually identifying and masking each melt layer in line scans using a simple algorithm for detecting connected pixels using a prescribed threshold. This image recognition algorithm comprises of two primary parts, threshold assignment and pixel connectivity procedure (Figure 3.2). First, an adaptive threshold is initially applied to the image by manually assigning a reference point within a melt layer (Figure 3.2b). The algorithm then separates the melt layers from the background by considering the empirical

distribution of the dark (melt layers) and bright (background) pixels. This results in a binary image (Figure 3.2c) of potential melt layers within the core section. Second, since the threshold-based segmentation is not definitive, an 8-neighbourhood pixel connectivity operation is carried out on the binary image. A pixel $P_{i+1,j+1}$ is said to be an eight neighbour of a pixel $P_{i,j}$ if the pixels share either an edge or a vertex, while a region is said to be 8-connected if every pixel in the region can be reached by a combination of moves in the two vertical, two horizontal and four diagonal directions. A mask is created that includes all pixel values that are 8-connected to the reference point and have a grey value within a tolerance range, where tolerance (scalar value) defines the range of pixel values to be included in the mask (grey value of reference point ± tolerance). The tolerance is by default set to 32, but this is adjusted according to each image section, depending on how well the grey values of melt layers are resolved in them. This helps in the identification of any stray pixels segmented during the thresholding process (Figure 3.2d). Finally, the holes in the binary mask are flood filled (Figure 3.2e), and the mask is morphologically eroded and then dilated to produce a smooth mask (Figure 3.2f). Because the reference point and tolerance were chosen manually, the mask results may vary from iteration to iteration. To ensure proper results, the melt masks were manually checked against raw images to ensure appropriate masking, and the procedure was repeated (Figure 3.2b-f) if any differences were identified. The threshold-based connected pixel recognition algorithm ensures that the morphology of the melt layer is well-preserved in the mask and since the VS record has a resolution of 51µm/pixel, even melt layers of sub-millimetre-scale would be morphologically well-resolved.

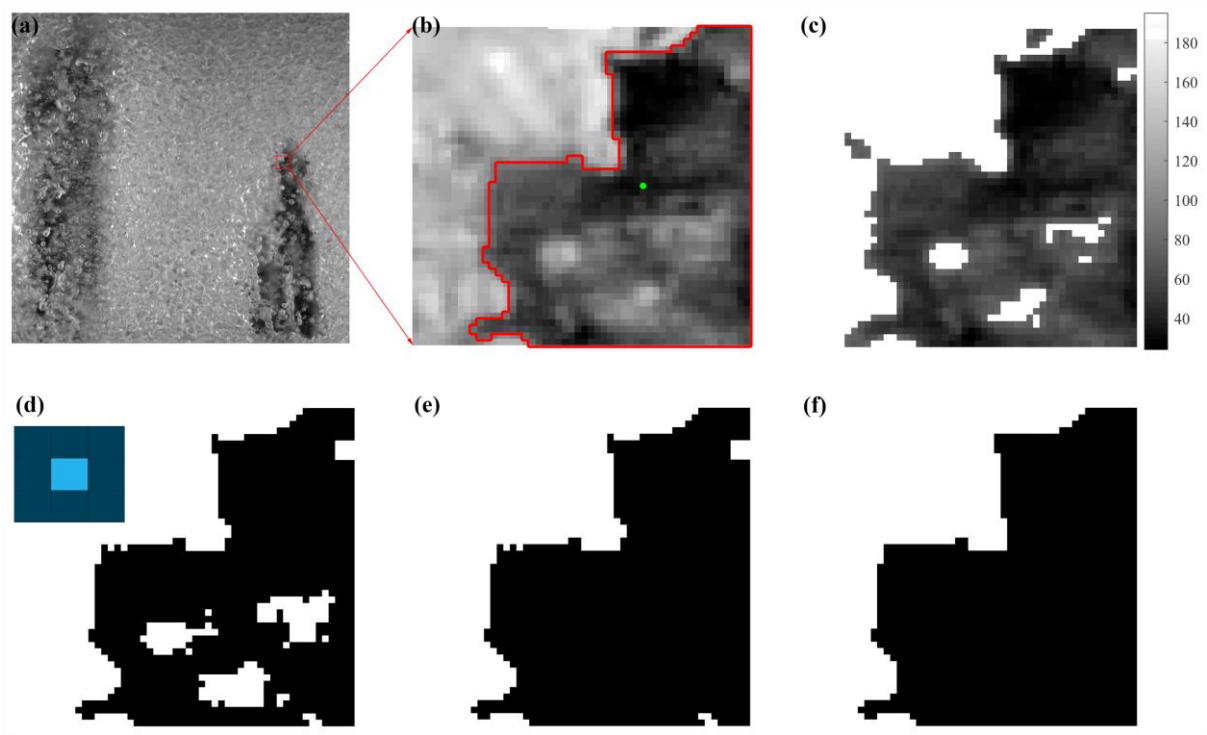

Figure 3.2 Melt layer masking with a threshold-based connected pixel algorithm. An ice core section with two visible melt is shown in panel **(a)** with the red square showing the section zoomed in for detailed reference in the following panels. Panels **(b)-(f)** show individual processing steps that are described in the text. The green dot in panel **(b)** represents the user input reference point, while the red polygon represents the final mask outline. For this section, a tolerance of 40 is utilised. Inset in panel **(d)** shows a schematic depiction of an 8-neighbourhood (dark blue) of a pixel (light blue).

These melt layers appear as clear, dark bands of ice with or without bubbles in VS record. This causes the core section's grey values (pixel intensity) to decrease abruptly, unlike the systematic and smooth changes shown in annual accumulation layers. Our study employed a melt layer mask to exclude the melt section from ice core images while preparing the VS record. This ensures that no bias is introduced in the VS records due to a higher melt in an ice core section. The melt layer mask created for the ice core was used to prepare and quantify the mass proportion of the melted and non-melted segments (Figure 3.2a). A melt layer was considered for calculating melt proportion only if it covers at least 50% width of the ice core (Abram et al., 2013a). The melt proportion is calculated as the percentage of the area of the core section comprised of melt layers by mass (assuming that the melt layer is consistent on the z-axis) to each annual layer identified using multi-proxy based chronology (Figure 3.1). The annual proportion of melt in the studied ice core varies between 0 and 4.4%, with a median melt proportion of 0.5% (Figure 3.3). The melt proportion is defined as the area of melt polygons, while other studies use the representative thickness of individual

melt layers. This methodological difference may affect the quantification of annual melt proportion. To examine this issue, the melt proportion using thickness was also calculated and compared with the melt proportion calculated with polygon area (Figure 3.3 and Figure 3.4). While both methods provide similar temporal change patterns, the melt proportion using layer thickness is overestimated by approximately two times compared to the estimates using melt layer polygons. The higher degree of overestimation generally occurs when the melt layers are not perfectly rectangular in shape or are not consistently well-formed through the width of the core.

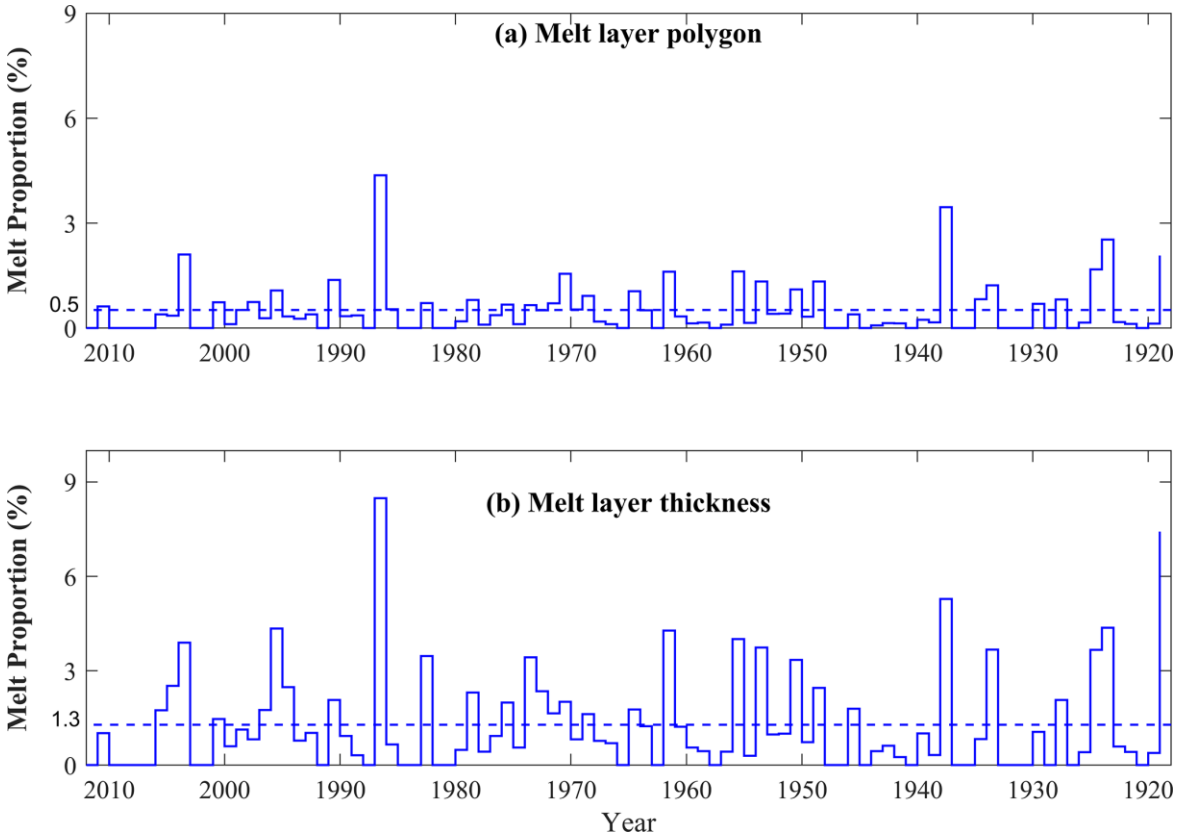

Figure 3.3 Melt layer distribution in the ice core was calculated using melt layer polygons **(a)** and melt layer thickness **(b)**. Estimated annual melt proportion (blue curve) plotted against the age. The blue dashed line shows the mean melt proportion (0.5% & 1.3% by using melt layer polygon and melt layer thickness, respectively) for the time period 1919 to 2011.

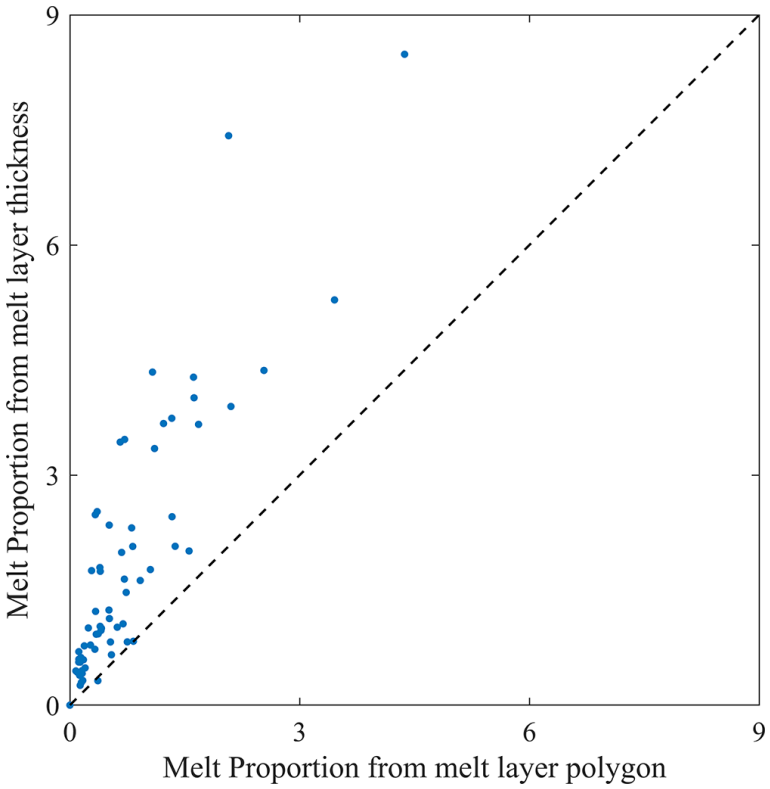

Figure 3.4 Scatter plot between annual melt proportion obtained using melt layer polygon and melt layer thickness. The dashed black line is the 1:1 correspondence line. All scatter points are restricted to the left of the black line, showing that melt proportion estimation using layer thickness is overestimated compared to the estimation from melt layer polygons.

Melt layers on polar ice sheets indicate warmer summer air temperatures and are a useful climatic proxy (Kelsey et al., 2010; Bertler et al., 2018). Melt layers appear as clear dark patches and are visually closer to ice than firn. These melt layers are primarily perpendicular to the length of the core, and their thickness can vary from less than a millimetre to several centimetres along the width of the core (Figure 3.5). Since most melt layers are sub-millimetre to less than a centimetre in width, they do not affect the VS record significantly. However, melt layers with thickness greater than a centimetre or the presence of multiple small melt layers at close intervals can significantly affect the VS record and create the illusion of an annual layer. The melt mask is used to remove all melt layer sections from the VS record. Melt frequency and melt percentage are two of the most common metrics for quantifying melt layers as they are not affected by annual layer thinning (Bertler et al., 2018). Melt percentage is used to quantify the melt layer record in this core. Using a melt layer polygon is therefore suggested to calculate annual melt proportion instead of melt layer thickness, as it would provide a better estimate of melt history from an ice core.

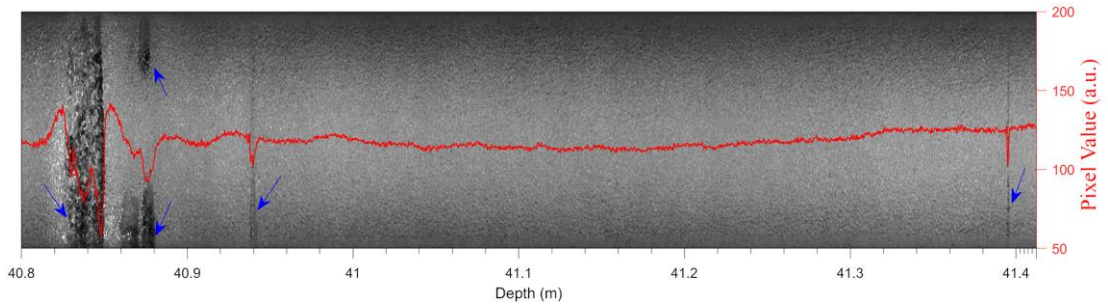

Figure 3.5 Line scan image profile of a core section of 0.65 m long and 7 cm wide. The greyscale highlights melt layers (marked with blue arrows) of sizes ranging from a few centimetres (first from left) to less than a millimetre (first from right). The mean pixel value along the width of the core is shown (solid red curve). A sharp fall in mean pixel values is observed when melt layers are present, even if less than a millimetre wide.

The occurrence of summertime melting is known to affect the isotopic composition of the near-surface snow. When snow particles come in contact with meltwater, isotopic fractionation occurs at the snow-melt interface. Melting in the early summer affects the highly depleted winter/spring snow, which is present at the surface. The meltwater may also percolate down and refreeze. Although a detailed analysis of the effect of surface melt on the $\delta^{18}O$ record is beyond the scope of the manuscript, the melt features observed in this study are on average 0.5% of the annual layer, with the highest melt proportion being 4.4%. Since the melt proportion at the present core site is low and no percolation of meltwater is observed in the studied section, the melt features do not significantly affect the use of stable isotope and chemical profiles from this ice core as a proxy of seasonal cycles. It is also safe to assume that the effect of summertime melting on the snowpack, if any, is restricted to the annual layer.

3.2.4. Effect of firn density on transmitted light intensity

The intensity of scattered light is maximum near the top, and it gradually decreases to less than half at 50m depth (Figure 3.6a). Firn density gradually increases over this depth range from 420 kg m^{-3} to about 840 kg m^{-3} (Figure 3.6b). The firn density controls this systematic depth trend of the scattered light intensity as has been previously observed by Kinnard et al. (2008) and Sjogren et al. (2007). This density effect is removed using circulant single spectrum analysis (Bógalo et al., 2021). This method works by extracting the underlying signals in a time series by identifying their frequency of oscillation in an automated way by simply introducing the data and a suitable window length. The VS record is used for this purpose and a window length of ten, giving six reconstructed components (RC). Increasing the window length above ten did not significantly affect the outcome and,

therefore, proceeded with the same. The first reconstructed component, RC1, replicated this general decreasing trend of VS with depth (Figure 3.6a) and has a clear dependence on density (Figure 3.6c). A second-order polynomial transfer function is derieved between density and RC1 (R^2= 0.92) (Figure 3.6c). The highest order component, RC6, shows largely random noise. Therefore, the sum of the intermediate four components, RC2-RC5, is considered as the representative component of VS variability attributed to the seasonal variability (Figure 3.6d).

Variations in several parameters, such as density and micro-inclusions, influence the intensity of light scattered through the ice core section. While density in the firn section has a long-term secular trend (Sjögren et al., 2007), micro-inclusions such as dust and sea salt inclusions exhibit seasonal variability (Svensson et al., 2005; Winstrup et al., 2012), which may be used to count annual layers. The quantity of air and air-ice contacts in the core substantially impacts the amount of light dispersed by the core. The density of the firn is likewise controlled by its air content; hence, there is a substantial link between density and the intensity of light transmitted through it. A non-linear relationship between the mean pixel intensity and density over the length of the ice cores has also been previously observed (Sjögren et al., 2007; Kinnard et al., 2008). A similar non-linear relationship is observed and once the trend due to the gradual increase in density is separated from the VS record, the resultant component would possibly represent the seasonal variability and can be used for annual layer counting.

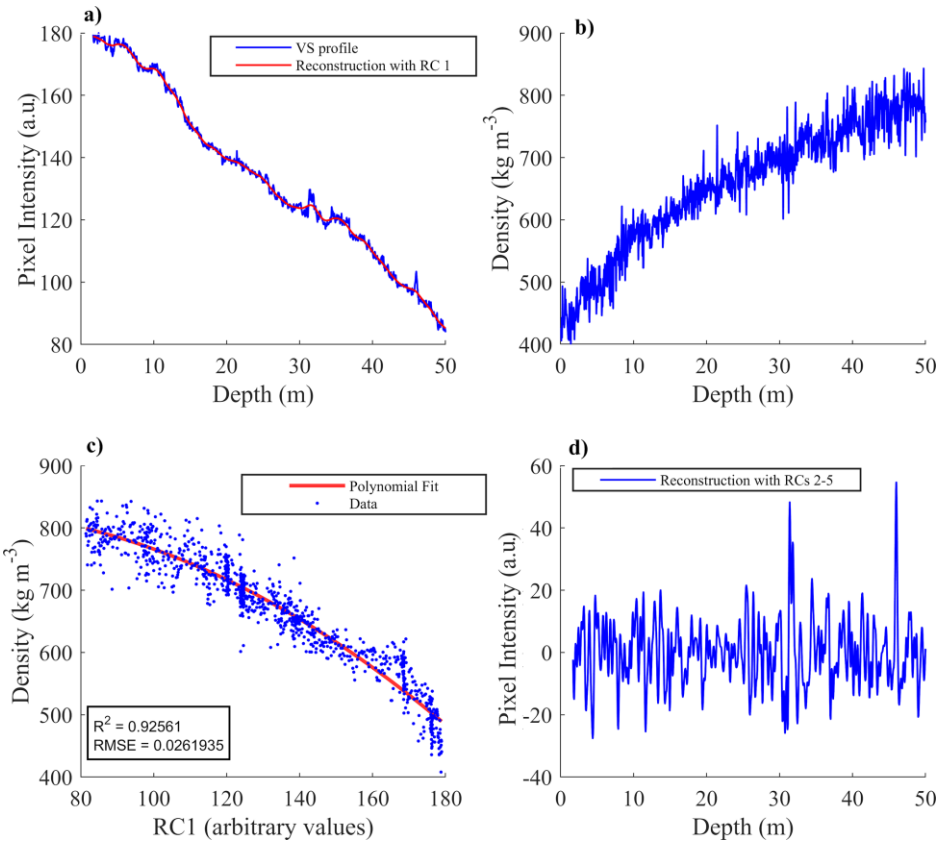

Figure 3.6 Depth profiles of the VS record and density. **(a)** Depth profiles of VS (blue curve) and the reconstructed component RC1 (red curve). **(b)** Depth profiles of the measured, 5-cm-resolution density data (blue). **(c)** Density dependence of RC1 scattering intensity (blue dots), which is fitted with a second-order polynomial transfer function (solid red curve). **(d)** The reconstructed seasonal component of VS as a cumulative sum of RC 2 to 5.

3.2.5. Visual stratigraphy from line scan images as a tool for firn core chronology

To examine the potential of high-resolution VS records as a reliable tool for annual layer counting in coastal Antarctica, an age-depth model is constructed based on layer counting of the VS record and then compared the age model against the nssSO_4^{2-} profile that has volcanic events and tritium marker horizons demarcated (Figure 3.7). Winters can be identified as peaks in the VS record. The processed VS record has relatively less noise, but still ambiguous peaks and shoulders are present. If all such ambiguous peaks and shoulders are identified as annual layers, it can result in significant overcounting. To ascertain the robustness of the VS age-depth model, StratiCounter is used for annual layer identification in the VS record. An initial annual layer template is provided for the algorithm, with certain and uncertain layers marked and constrained using the time markers identified in section 3.1. The age-depth model from VS is highly robust, with the error in the chronology being less than ± 2 years for the past century.

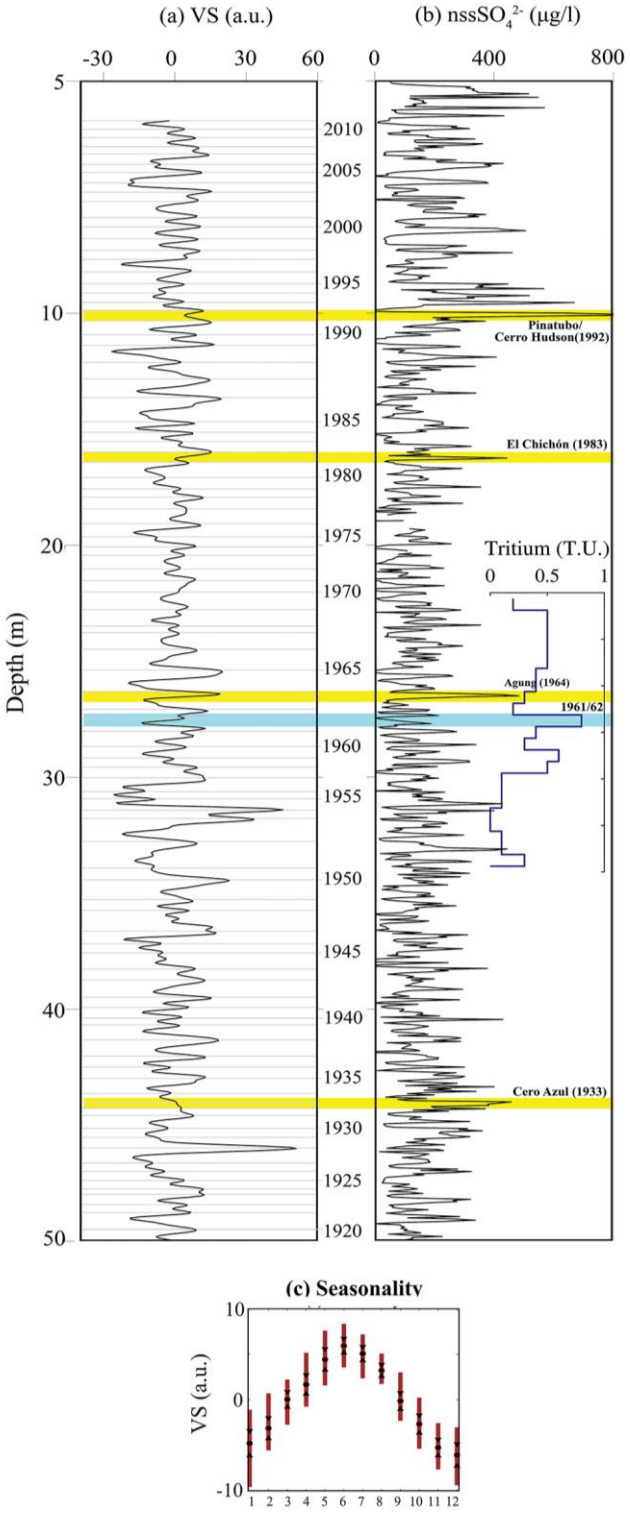

Figure 3.7 Comparison of age models using VS record and volcanic events. **(a)** Depth profile of VS (sum of the reconstructed components RC2-RC5). Annual layers (winter peaks) using the StratiCounter program are marked with gray bars and every fifth year is labelled. **(b)** Same as Figure 3.1b. **(c)** Seasonality plot of VS record plotted similar to Figure 3.1d. Note that the VS record uses arbitrary units (a.u.).

The seasonality of the VS record is calculated as explained in section 3.2 and shown in Figure 3.7c. The reported age model error for the majority of high-accumulation ice core records from coastal Antarctica for the past century is ±2 years or greater (Isaksson et al., 1999; Thamban et al., 2006; Naik et al., 2010; Thamban et al., 2013; Laluraj et al., 2014; Philippe et al., 2016). Therefore, the high-resolution VS profile studied here provides a reliable means to constrain the ice core chronology with similar accuracy to previous studies. Our study shows that VS profiles have high potential as a preliminary and supplemental age tool due to their clear seasonality (Figure 3.7c) and especially considering that analysis of isotopic and chemical proxies require more time and resources. Considering the extensive summertime melting in low elevation sites of coastal Antarctica, where annual layer counting and chronological constraints using stable isotope and chemical records are susceptible to larger uncertainties, the VS method would be advantageous when used in tandem with other proxies.

The ultra-high-resolution VS profile of the ice core also provides a detailed picture of the physical processes and environmental variability during the period. Throughout the length of the core, clear ice core layering is visible. The dark and bright horizons observed in the VS profiles are formed due to variation in micro-inclusions in the ice cores, and these micro-inclusions are known to have seasonal variations (Winstrup et al., 2012). However, in the top snow/firn section of the ice core, where annual layer thickness is large, the high resolution of VS data makes it challenging to differentiate annual signals from the noise. However, with proper filtering and downsampling, it is possible to extract the annual signals in the VS profile. Visual stratigraphy in ice cores can be challenging due to non-uniform firnification or depositional events and becomes less clear with increasing age and depth, owing to densification and other physical changes. Thus, identification of annual layers, solely based on VS can be tricky due to the presence of multiple peaks within an annual layer, however, when several of the above methods are combined, such discrepancies can be identified and removed. Hence, VS provides valuable support in the identification of seasonal cycles with higher confidence, in turn resulting in a more robust chronology.

Chapter 4

Influence of sea ice distribution on the climatic variability during the past 250 years in coastal Dronning Maud Land, East Antarctica

4.1 Introduction

Antarctic sea ice plays a pivotal role in shaping Antarctica's regional climate and circulation systems, exerting a profound influence on the surrounding ecosystem. Satellite observations initiated in the late (Zwally et al., 2002; Turner et al., 2009) revealed a consistent expansion of total Antarctic sea ice cover until 2014. However, subsequent data indicated a significant decline, leading to a halving of the increasing trend for 1979–2018 relative to 1979–2014 (Parkinson, 2019). Regional trends exhibit variability, with the Weddell Sea and Ross Sea sectors experiencing notable increases in sea ice extent (Parkinson and Cavalieri, 2012), while the Bellingshausen Sea witnesses a pronounced reduction (Hobbs et al., 2016). A rapid decrease in SIE initiated in summer 2016/17 around Antarctica was attributed to multiple factors like a negative phase of Southern Annular Mode (SAM), deepening of the Amundsen Sea Low (ASL) (Turner et al., 2017; Wang et al., 2019), persistence of El-Nino-induced warm waters (Stuecker et al., 2017), a strong negative phase of the Indian Ocean Dipole and La Niña (Wang et al., 2019; Purich and Doddridge, 2023), and passage of explosive polar cyclones (Jena et al., 2022).

Model simulations predict a 25% decline in Antarctic sea ice with limited regional heterogeneity (IPCC, 2013). This projection is attributed in part to the underestimation of the Southern Hemisphere westerly winds' intensification and position (Purich et al., 2016) and associated Ekman pumping of subsurface warm waters (Ferreira et al., 2015). Recent observations in the eastern Antarctic Peninsula support these model simulations(Etourneau et al., 2019). Given that observations of Antarctic sea ice conditions are confined to the satellite era post-1970, evaluating the significance of recent trends is challenging. Reliable past sea ice reconstructions are essential for optimising climate models tasked with predicting future changes, as historical sea ice area data heavily influence future warming simulations (Bracegirdle et al., 2015). Chemical or isotopic records from Antarctic ice cores (Abram et al., 2010; Thomas and Abram, 2016; Ejaz et al., 2021) and marine sediment cores from the Southern Ocean (Gersonde et al., 2005; Nair et al., 2019; Ghadi et al., 2020) offer insights into decadal to millennial-scale changes. Ice cores, drilled on the Antarctic ice sheet,

provide a unique proxy record, capturing sea ice information signatures due to particle transportation from the ocean surface to the atmosphere. Most importantly, ice cores offer higher temporal resolution compared to marine sediment cores.

In ice core studies, sea salt sodium ($ssNa^+$) is a key indicator of sea-ice variations (Wolff et al., 2003; Wolff et al., 2006). The formation of high salinity "frost flowers" and brine on sea ice surfaces (Rankin et al., 2000) contributes to $ssNa^+$. However, distinguishing this source from other dominant sources, such as sea spray aerosol, proves challenging (Curran et al., 1998; Abram et al., 2011). Laboratory experiments (Roscoe et al., 2011) highlight the stability of frost flowers in windy conditions, complicating the identification of their source. It was proposed that blowing snow over the sea ice, particularly rich in salts, could be a substantial source of $ssNa^+$ in several Antarctic sites (Yang et al., 2008). Despite the significant contribution from blowing snow, sea-salt aerosol from the open ocean remains noteworthy, especially during ice-free summer months (Röthlisberger et al., 2010).

This study used a 122m long ice core (IND36/9) from the summit of Djupranen ice rise in coastal Dronning Maud Land to understand better the role of sea ice variability in coastal Antarctica. Annual $ssNa^+$ flux from the ice core is used to reconstruct the past sea ice variability and understand its role in controlling the snow accumulation rates at the ice core site.

4.2 Results and discussion

4.2.1 Evaluating the sea ice proxies

Annual average concentrations of Sodium (Na), Calcium (Ca) and Chlorine (Cl) in the IND36/9 ice core are significantly (positive) correlated ($p<0.05$) with the mean winter (JJA) sea ice concentration (Fetterer, 2017) over the King Haakon Sea during 1979 - 2016 (Figure 4.1). Sulphate (SO_4) is however negatively correlated to the SIC over the Weddell Sea, possibly due to the higher productivity in the Weddell Sea region (Vernet et al., 2019). The correlations are stronger and more significant when converting ionic concentration to flux, accounting for yearly snowfall. The enhanced correlations may reflect the close relationship between sea ice and snow accumulation, driven by atmospheric circulation and winds and decreasing sea ice concentration, resulting in additional moisture supply.

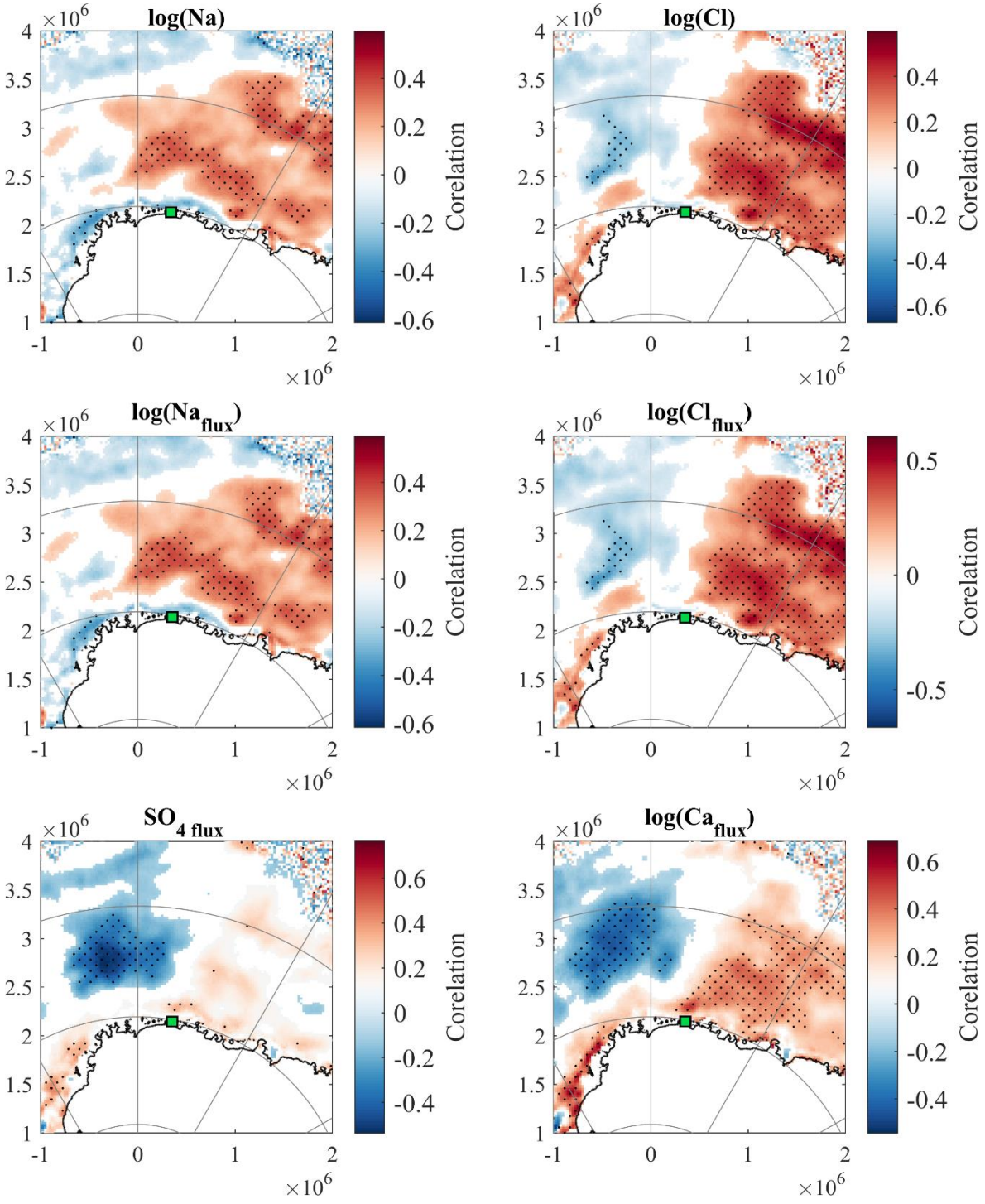

Figure 4.1 Spatial correlation of ice core proxies with mean JJA sea ice concentration during 1979 to 2016. Green square shows the ice core location.

The spatial correlations and trends are very similar when using either concentration or flux, but flux was used in this study to account for the accumulation rate variability and due to the improved statistical significance. In order to reconstruct the past SIC variability, Na measurements are used. Although there is an additional input from crustal dust of all the

metals found in sea salt, this is relatively much more important (requiring a larger and less certain correction) for elements like magnesium, potassium and calcium than sodium. Chloride is subject to fractionation due to the reaction of acids with sea salt to produce HCl, and this can be particularly important in coastal regions and variables. SO_4 can have a significant non-sea salt contribution from volcanic events, terrestrial dust and due to secondary aerosol formation, which is sometimes difficult to estimate accurately. Na is, therefore, the most reliable ionic marker for reconstructing past SIC variability (Wolff et al., 2010). The sea salt component of Na, $ssNa^+$, used for further sea ice reconstruction is calculated as:

$$ssNa^+ = \frac{R_c.Na^+ - Ca^{2+}}{R_c - R_m}$$

where, $R_c = 1.78$ and $R_m = 0.038$ (Rothlisberger et al., 2002).

Annual mean $ssNa^+$ concentrations are converted to a deposition flux by multiplying it with annual snow accumulation rate. Flux estimates from ice cores account for both wet and dry deposition, of which the contribution of these two depositional modes varies across Antarctica with elevation and distance from the source (Wolff, 2012). The ion chromatograph results for every ionic species' concentrations show them to be log-normally distributed (Moore et al., 2006), which is also consistent with ion chromatograph measurement errors being proportional to concentration. Therefore, log transform of the $ssNa_{flux}$ record (hereafter $ssNa_{flux}$) is used in this study for further analyses. The $ssNa_{flux}$ record is highly variable, with values ranging between 1.33 to 4.65 and mean value of 3.33 ± 0.64. Over the satellite period, annual $ssNa_{flux}$ shows a strong co-variability with the mean JJA SIC over the King Haakon Sea sector, especially during 2000-2016. However, there are multiple years with anomalously high $ssNa_{flux}$ associated with low SIC (Figure 4.2). This is possibly an influence of frequent polynya opening in the Weddell Sea (Campbell et al., 2019; Heuzé et al., 2021) which supply additional sea salt during the winter to early spring months.

The amount of sea salt transported from surrounding seas to Antarctic ice sheet is influenced by several factors, complicating both quantitative and qualitative interpretations. Beyond the expansion of production areas, three additional factors may contribute to an increase in sea salt: (a) heightened wind at the source, leading to greater uplift from open water sources and additional blowing snow over sea ice sources; (b) increased speed of transporting wind, resulting in more material reaching the Antarctic land; and (c) an extended

residence time of sea salt aerosol, possibly due to lower precipitation rates during dry cold periods. These factors must be considered for a comprehensive quantitative proxy but are extremely difficult to quantify.

It is wrong to exclude the impact of subtle variations in atmospheric sea salt loading caused by changes in transport, which low-resolution models may not adequately capture. Studies indicate that a decrease in the Southern Annular Mode (SAM) intensity during winter, marked by a decline in the westerly wind system, can lead to heightened sea salt levels at a coastal Antarctic ice core site (Goodwin et al., 2004). The El Niño-Southern Oscillation, with teleconnections to the Southern Ocean, may also contribute to variations in atmospheric sea salt loadings around Antarctica (Vance et al., 2013). Moreover, uncertainties persist regarding changes in the strength of interannual climate modes on longer timescales and the stationarity of their teleconnections. These aspects remain poorly constrained in both proxy records and climate simulations (Goodwin et al., 2004; Vance et al., 2013).

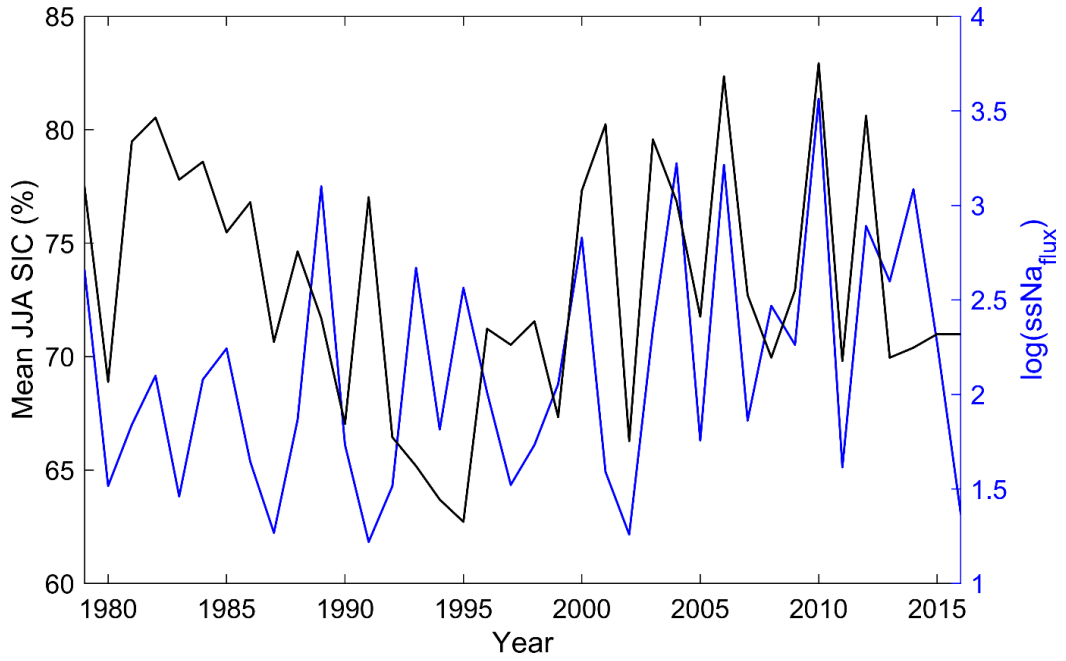

Figure 4.2 Time series of mean JJA SIC from NSIDC and log of annual $ssNa_{flux}$ from the ice core

4.2.2 Reconstruction of past sea ice concentration

To reconstruct the past SIC, the long-term trend in the $ssNa_{flux}$ record is separated using circulant single-spectrum analysis (Bógalo et al., 2021). This method works by extracting the underlying signals in a time series by identifying their frequency of oscillation in an automated way by simply introducing the data and a suitable window length. A window

length of ten is used, giving six reconstructed components (RCs; Figure 4.3a) and increasing the window length above ten decreases the variance explained. The first four reconstructed components (RCs 1 – 4) explain 83% of the total variability in the annual $ssNa_{flux}$ record and have a significant positive correlation with the mean JJA SIC (Figure 4.3b). However, only ~34% of the variance in SIC is explained by RCs 1 – 4.

In order to assess the approximate change in past sea ice cover using the ice core $ssNa_{flux}$ record, geometric mean regression (reduced major axis regression; Figure 4.3b,c) is used. This approach circumvents the presumption inherent in ordinary least squares regression, which assumes no error in the independent variable, such as satellite sea ice extent records. The geometric mean regression method accommodates errors in both parameters by determining the best-fit line that minimises errors in the x and y dimensions. Therefore, this considers measurement inaccuracies in SIC and the ice core record. These inaccuracies encompass errors in the annual layer identification, which depend on precise dating and cutting, and analytical errors arising from sample preparation and instrumental analyses. The reconstructed SIC is used to identify the long-term trends and the possible climatic factors influencing the SIC changes in the region. A Bayesian model averaging time-series decomposition algorithm (BEAST; Zhao et al. (2019)) is used to detect the change trends and abrupt changepoints in the reconstructed SIC timeseries. The BEAST (Bayesian Estimator of Abrupt change, Seasonal change, and Trend) algorithm detects three major, short-spanned and abrupt events while the overall reconstructed SIC shows a decreasing trend (Figure 4.4; top panel). The events (numbered I, II and III; Figure 4.4) are characterised by an abrupt decrease in the reconstructed SIC, followed by a rapid increase over a short time frame (12, 6 and 13 years, respectively). The exact mechanism behind these events is beyond the scope of this study and would require detailed insights and observation records of the physical processes driving the sea ice change. The abrupt events divide the reconstructed SIC into four major periods (excluding the events themselves). Between 1774 to 1800 CE, a sharp decrease in sea ice is observed, followed by a mostly stable period between 1812 to 1913 CE. There are smaller periods of intermediate increasing and decreasing SIC, however the decreasing trend becomes stronger from the early 1880s. The period between 1919 and 1987 CE shows a continued decrease in SIC, with a relatively stronger trend since the 1970s. The SIC trend after 2000 CE is unclear due to the short time period.

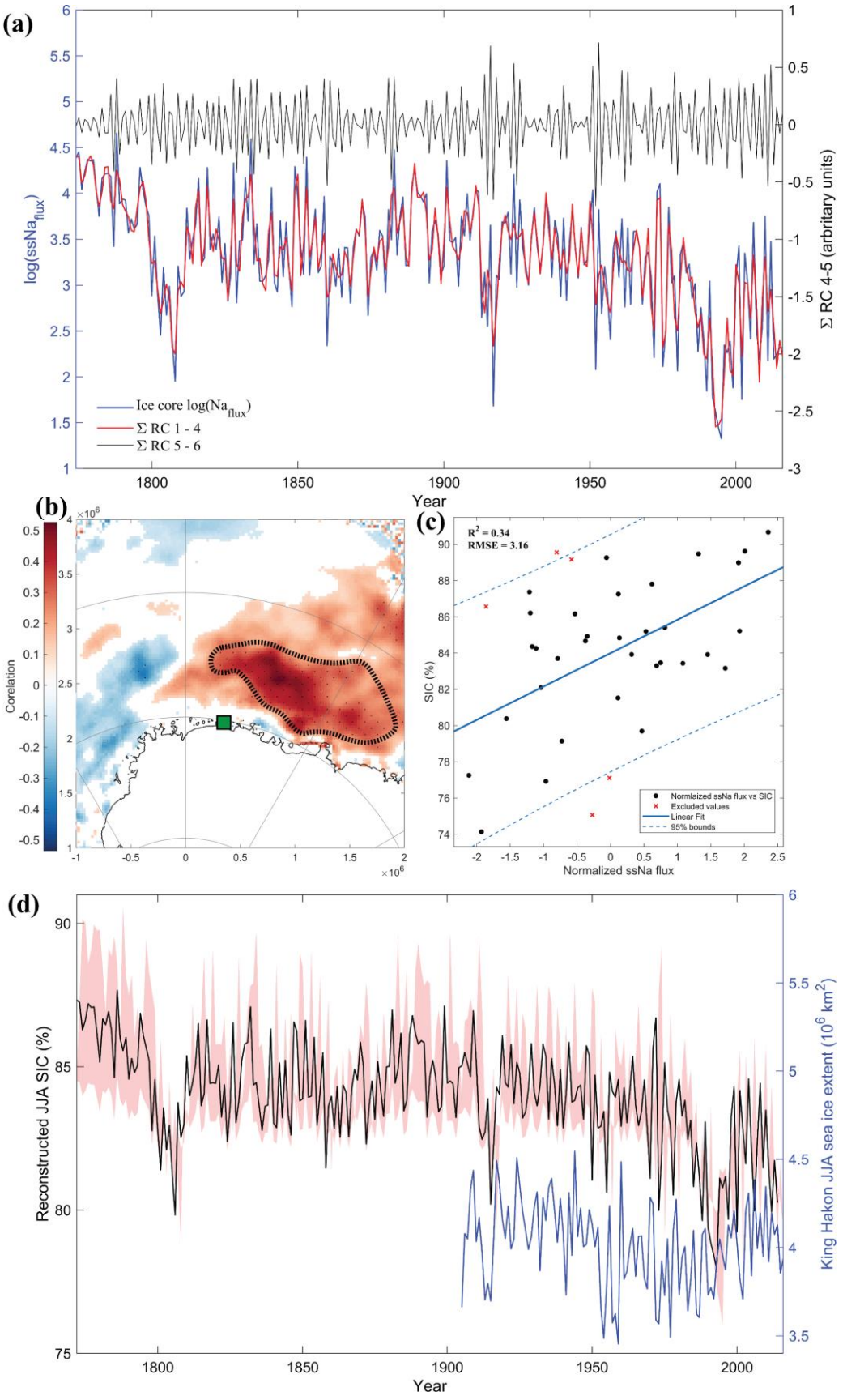

Figure 4.3 (a) Annual $ssNa_{flux}$ timeseries (blue curve) with the sum of RCs 1 – 4 (red curve), which is used for SIC reconstruction and sum of RCs 5 and 6 (black curve). **(b)** Spatial

correlation of annual mean JJA sea ice concentration (SIC) from NSIDC with ice core $ssNa_{flux}$. Black stipples show the regions of significant correlation at $p<0.01$. The dashed-black outline shows the region used for SIC reconstruction, and the green square symbol is the ice core location **(c)** Geometric mean regression fit (blue line) with 95% confidence bounds (dashed-blue lines) between ice core $ssNa_{flux}$ and mean JJA SIC over the outlined regions (black dots). **(d)** Reconstructed SIC record (black curve) with 95% uncertainty bound (red patch) on the left axis and the annual JJA sea ice extent over the King Haakon Sea from 1905 to 2016 (Fogt et al., 2022).

The interruption of the long-term circumpolar sea ice increase is evident in the record low sea ice observed between 2016 and 2019, marking a decline rate comparable to that observed over 30 years in the Arctic (Parkinson, 2019; Handcock and Raphael, 2020; Eayrs et al., 2021). Preceding the satellite sea ice record, studies utilising ice cores and whaling records highlight sharp declines, notably in the late (Kukla and Gavin, 1981; de la Mare, 1997; Curran et al., 2003; Cotté and Guinet, 2007; de la Mare, 2008). Fogt et al. (2022) found a decline in Antarctic sea ice from 1905 until the onset of satellite observations, particularly in the Ross, Amundsen, and King Haakon seas. The observed increasing trend during the satellite period is deemed unique in the context of the 20th century (Fogt et al., 2022). Simulations exploring multi-decadal sea ice trends, replicating the modest overall increase in Antarctic sea ice, also depict decreasing sea ice in the decades preceding the satellite record (Goosse et al., 2009), similar to the observations from this study. The successive overall increase prompts speculation about the responsiveness of Antarctic sea ice to abrupt changes in atmospheric or oceanic conditions, with the capacity to recover from declines over the ensuing decades (Parkinson, 2019; Eayrs et al., 2021).

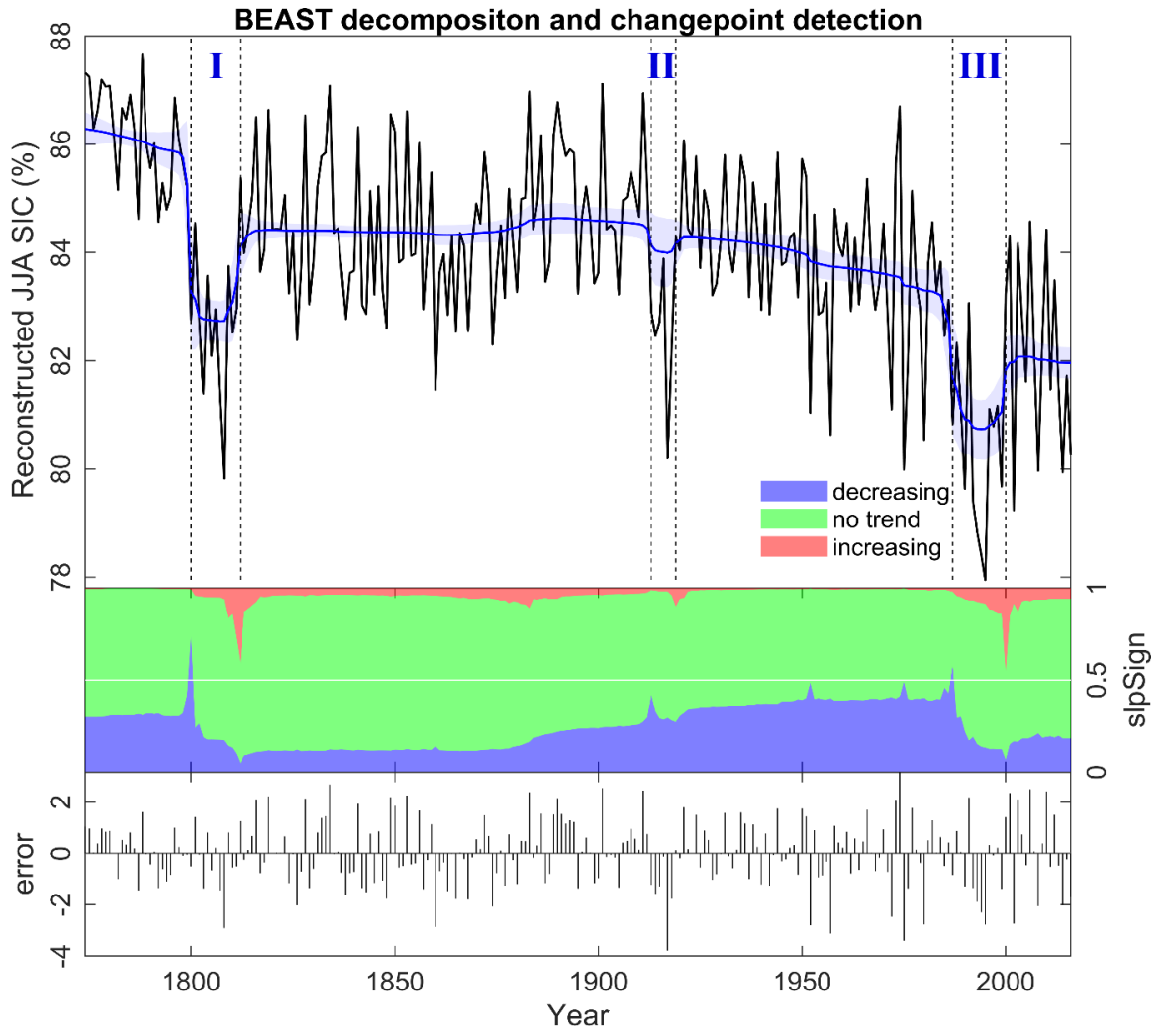

Figure 4.4 Trend variability in the reconstructed sea ice record. The top panel shows the reconstructed JJA SIC with the trend (blue curve) and 95% confidence bound (blue patch). Three abrupt events are detected are numbered I, II and III. Middle panel shows the intensity of the increasing (red patch), decreasing (blue patch) and no trend (green patch). Bottom panel shows the estimation errors.

4.2.3 Snow accumulation variability

Combining annual layer thickness data with gravimetric density measurements, annual snow accumulation rates were reconstructed for the IND36/9 ice core. The accumulation record shows large variability, ranging from 0.1 to 0.9 m w.e. with an average accumulation rate of 0.32 ± 0.16 m w.e. (Figure 4.5a) over the studied time period. Significant periods in the snow accumulation records are identified using the BEAST algorithm, as explained in Section 4.2.2. The significance of the trend and slope are calculated using Mann-Kendall and Sen's slope estimator test. The annual accumulation trend is separated over four different periods: no significant trend between 1774 – 1806, a slight decreasing trend ($p < 0.05$) between 1806 – 1888, no significant trend between 1888

– 1927 and finally, a large decreasing trend from 1927 – 2016 ($p < 0.01$). Wavelet analysis reveals a strong variability in the 3 – 8 years band, with the variance in the band being the strongest between 1800 – 1850 and 1900 – 2000 (Figure 4.5b, c). The mean accumulation rate of IND36/9 ice core falls within the reported range from DML and is comparable with that of the published records from the region (Kaczmarska et al., 2004; Naik et al., 2010; Philippe et al., 2016; Vega et al., 2016; Ejaz et al., 2021; Wauthy et al., 2023). The trends in the accumulation records in previous literature are, however, complex and conflicting within the coastal Dronning Maud Land (DML). Ice core records of S100 (Kaczmarska et al., 2004), Fimbul Ice Shelf (FIS) composite (Schlosser and Oerter, 2002), KC (Vega et al., 2016), IND33 (Ejaz et al., 2021) and TIR18 (Wauthy et al., 2023) showed a distinct decreasing trend in recent times. However, KM, BI (Vega et al., 2016), IC12 (Philippe et al., 2016) and FK17 (Wauthy et al., 2023) revealed an increasing trend. More interestingly, within the Princess Elizabeth Land itself, among the neighbouring ice cores (viz., IC12, FK17 and TIR18), two ice cores show an increasing trend while the other one shows a decreasing trend over the last century. Therefore, complex and local atmospheric and maritime processes can induce large variability in accumulation trends in the region.

Orography and orography-induced wind changes play a significant role in influencing surface mass balance (SMB) variability in coastal Antarctica (Lenaerts et al., 2014). Local variations in wind strength and direction also contribute to this variability. The impact of wind ablation and blowing snow, a major source of uncertainty in SMB modelling, is crucial for understanding spatial and interannual variability. In the escarpment zone of Antarctica, orographic uplift and associated wind erosion contribute to the highest snowfall and error in predicted snowfall trends (Genthon et al., 2009). Wind ablation, particularly in the escarpment area of DML, can entirely remove low to medium precipitation events, while high-precipitation events result in a net positive SMB (Gorodetskaya et al., 2015). Frezzotti et al. (2013) suggest that an increase in SMB, coupled with increased wind speed, may lead to higher SMB in areas with low wind speed and lower SMB in regions with high wind speed.

Frezzotti et al. (2013) proposed an increase in SMB at low-altitude sites and on the high ridges due to more frequent anticyclonic blocking events. However, they noted a decrease at intermediate altitudes, attributing it to stronger wind ablation in the escarpment areas. In DML, Altnau et al. (2015) reported a SMB increase over the plateau and a decrease on coastal sites, associating these changes with altered circulation patterns. Along a traverse

route from coast to Dome A, (Ding et al., 2011) observed increased SMB around 800–1128 km from the coast and a recent decrease towards the coast, suggesting that climate warming facilitates easier inland moisture transfer. Temporal and spatial SMB variability is primarily determined by atmospheric circulation, with sea-ice and ocean surface conditions playing a secondary role. A fully coupled climate model study by (Lenaerts et al., 2016) indicates that, in a warmer climate, DML is the most susceptible region to increased snowfall. Such a rise in coastal snowfall is attributed to the loss of sea ice cover in the southern Atlantic Ocean, enhancing atmospheric moisture uptake through evaporation. The prolonged exposure to open water results in higher near-surface temperatures, promoting evaporation and increasing moisture availability for ice sheet precipitation (Lenaerts et al., 2016).

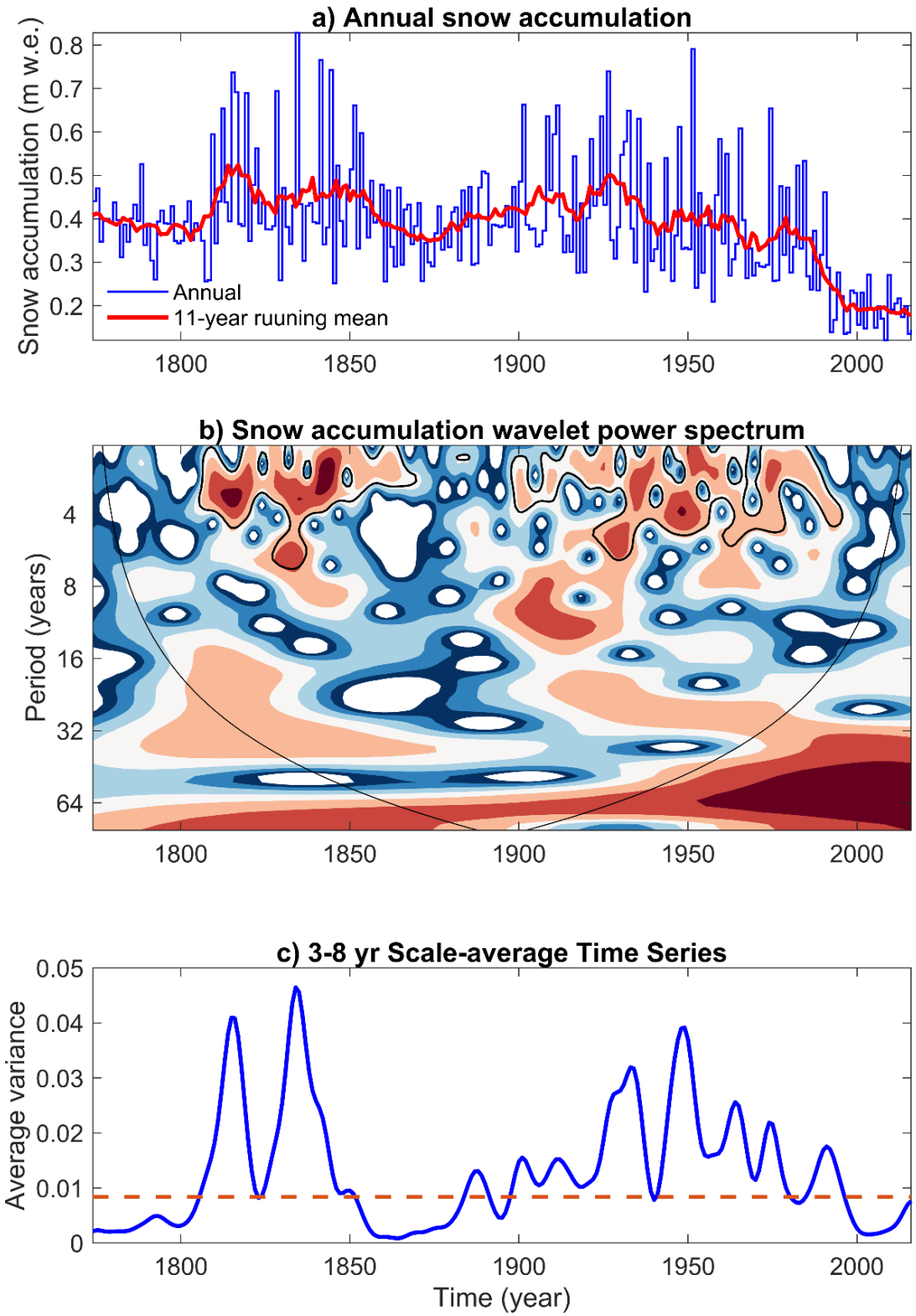

Figure 4.5 (a) Annual (blue curve) and 11-year running mean (red curve) snow accumulation rate reconstructed from the IND36/9 ice core. **(b)** Wavelet power spectrum of reconstructed annual snow accumulation. A strong variability is observed in the ENSO band (3 – 8 years). **(c)** The average variance of the 3 – 8 years band shows significant peaks throughout.

4.2.4 Influence of SAM and ENSO

To understand the control of Southern Annular Mode (SAM) and El Niño Southern Oscillation (ENSO) on sea-ice variability over the study area, the NSIDC winter (JJA) SIC record is correlated with the SAM index (Marshall, 2003) and Southern Oscillation Index (SOI). This spatial correlation map highlights a significant (95% level) positive correlation over the study area (Figure 4.6). This demonstrates the possible role of SAM and ENSO in influencing sea ice cover of the region. Power spectrum analysis (Schulz and Mudelsee, 2002) of the reconstructed SIC is used to understand the inherent periodicities (Figure 4.7a). Periodicities of 2, 2.5, 3.8 and 18 years were significant at the 95% $\chi 2$ levels. The periodicities observed in the power spectrum analysis indicate strong interannual to multi-decadal variability in the SIC over the past ~250 years. Wavelet analysis was performed using the method proposed by (Torrence and Compo, 1998) to investigate these periodicities further. The wavelet analysis demonstrated how these periodicities evolved at various frequency bands ranging from interannual to multi-decadal scales (Figure 4.7b,c). The analysis shows significant periodicities at 3–8 years band at discrete intervals, which became more pronounced in recent decades (Figure 4.7c).

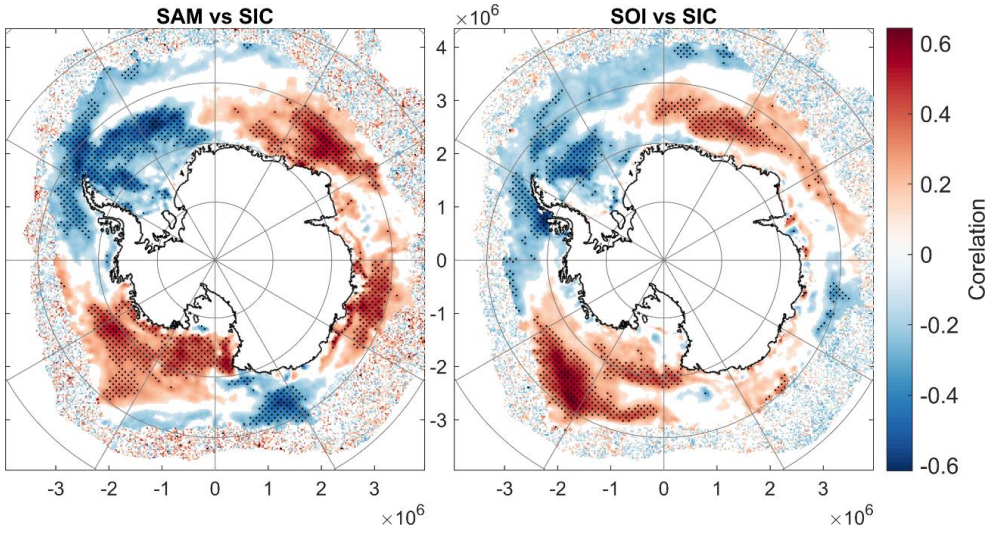

Figure 4.6 Spatial correlation of annual sea ice concentration from NSIDC with **(a)** ENSO (Southern Oscillation Index) and **(b)** SAM (Marshall Index) for the time period 1979 – 2016.

Interestingly, the scaled average variance at the ENSO band (3−8 years) showed a significant increase after ~1960 CE (Figure 4.7c). The increase in variance at the ENSO band is consistent with the findings of previous studies (Stammerjohn et al., 2008; Ejaz et al., 2021) that have reported a strengthening of the ENSO in recent decades. These findings suggest that the variability in the sea ice record is driven by a combination of interannual

and decadal variability and that the ENSO plays a significant role in the evolution of these periodicities over time. Several studies have indicated that the Southern Ocean's SST and the associated variability in SIC are subject to ENSO-related climate teleconnections through alterations in surface energy fluxes (Ciasto and England, 2011; Yeo and Kim, 2015). A recent study by Isaacs et al. (2021) suggested that ENSO affects SIC through similar mechanisms as the well-established link between ENSO and sea ice in West Antarctica (Kwok and Comiso, 2002; Yuan, 2004). The link in West Antarctica is driven by large-scale atmospheric circulation perturbations caused by tropical Pacific SST anomalies. This leads to the development of a southward-propagating wave train that results in low (high) pressure anomalies in the Amundsen Sea region during a La Niña (El Niño), and vice versa in the Weddell and King Haakon Sea. These circulation changes affect local heat fluxes and advection in various regions, subsequently influencing the SIC variability. It is possible that a southward-propagating atmospheric wave train could alter SIC by enhancing the meridional airflow. Given that the study area falls within the region studied by Isaacs et al. (2021), the sea ice variability at IND36/9 can be explained through a similar mechanism.

The SAM is another major factor influencing the sea ice variability around Antarctica. While SAM does not have an inherent periodicity band like ENSO, most of its effects could be explained by its annular form and the related changes in zonal winds. However, the departures from this annular pattern have large consequences for sea ice as they are associated with meridional exchanges and, thus, large heat transport. SAM is approximately zonally symmetric, although its structure/shape changes on various timescales (Fogt and Bromwich, 2006; Fogt and Marshall, 2020). The SAM remains the leading SH mode of variability outside the tropics on daily (Baldwin, 2001) to decadal timescales (Kidson, 1999). SAM induced changes in zonal winds tend to favour the equatorward expansion of the Antarctic-wide sea ice concentration through the oceanic Ekman effect (Hall and Visbeck, 2002), meridional winds and play a strong role in regional sea ice extent variability through wind-driven ice drift (expansion for southerly flow, and compaction for northerly flow). A recent study (Medley and Thomas, 2019) has shown that the SAM is also the dominant contributor to the interannual variability in snow accumulation rates at the regional scale, explaining more than 80% of the spatial snow accumulation variability in trends over the 1957–2000 CE period.

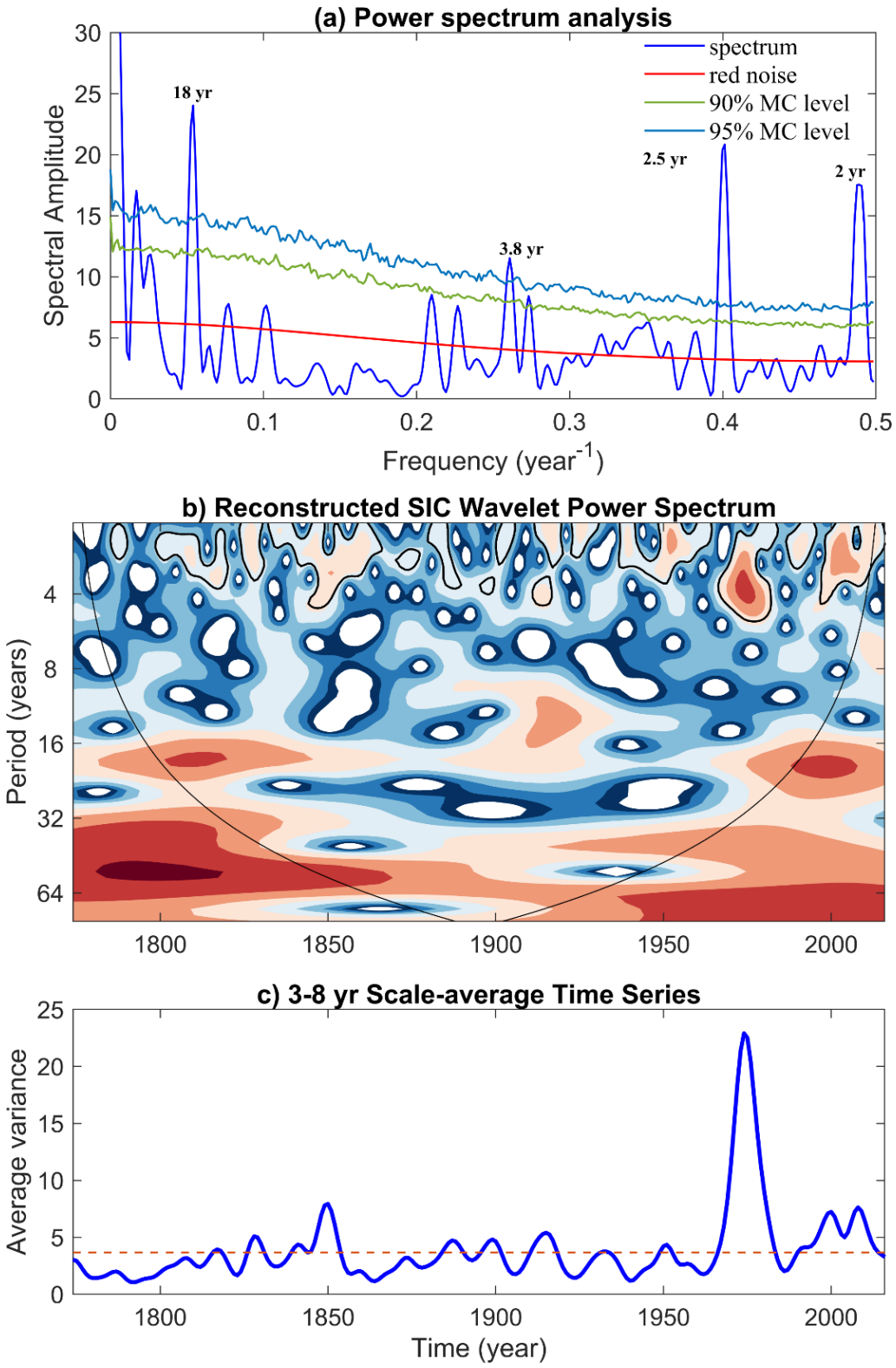

Figure 4.7 (a) Power spectrum analysis of the reconstructed SIC record of IND36/9 showing significant periodicities. **(b)** Wavelet power spectrum of reconstructed SIC. A strong

variability is observed with the reconstructed SIC record in the ENSO band (3 – 8 years). **(c)** The average variance of the 3 – 8 years band shows significant peaks over the time scale.

The annual snow accumulation rate from the IND36/9 ice core is significantly (negatively) correlated with 20th Century Reanalysis (20CR) indices for SAM ($r = - 0.36$, $p < 0.01$; 1851 – 2011) and SOI ($r = -0.28$, $p < 0.01$; 1851 – 2014). This shows that there is significant influence of SAM and ENSO on the snow accumulation rates at the ice core site. Their combined phase relationship also plays an important role. A slight decrease in snow accumulation is observed between 1806 and 1888 when the SAM and ENSO index are not in phase while the decreasing trend increases drastically (3.33 times) when the SAM and ENSO indices are in phase from 1927 onwards (Figure 4.8). Over the past century, ice and firn cores from coastal DML exhibited a nonlinear snow accumulation trend (Thomas et al., 2017). However, apart from the cores from Derwael Ice Rise (Philippe et al., 2016) and Lokeryggen Ice Rise (Wauthy et al., 2023), all cores show a negative trend in snow accumulation during the 20th century. Meanwhile, temperatures and stable isotope ratios are either increasing or constant (Isaksson and Melvold, 2002; Schlosser et al., 2010; Sinisalo et al., 2013; Altnau et al., 2015; Vega et al., 2016). This highlights the intricate interplay of dynamic and not thermodynamic processes, with atmospheric circulation and sea ice playing a significant role in influencing snow accumulation in the coastal areas of DML.

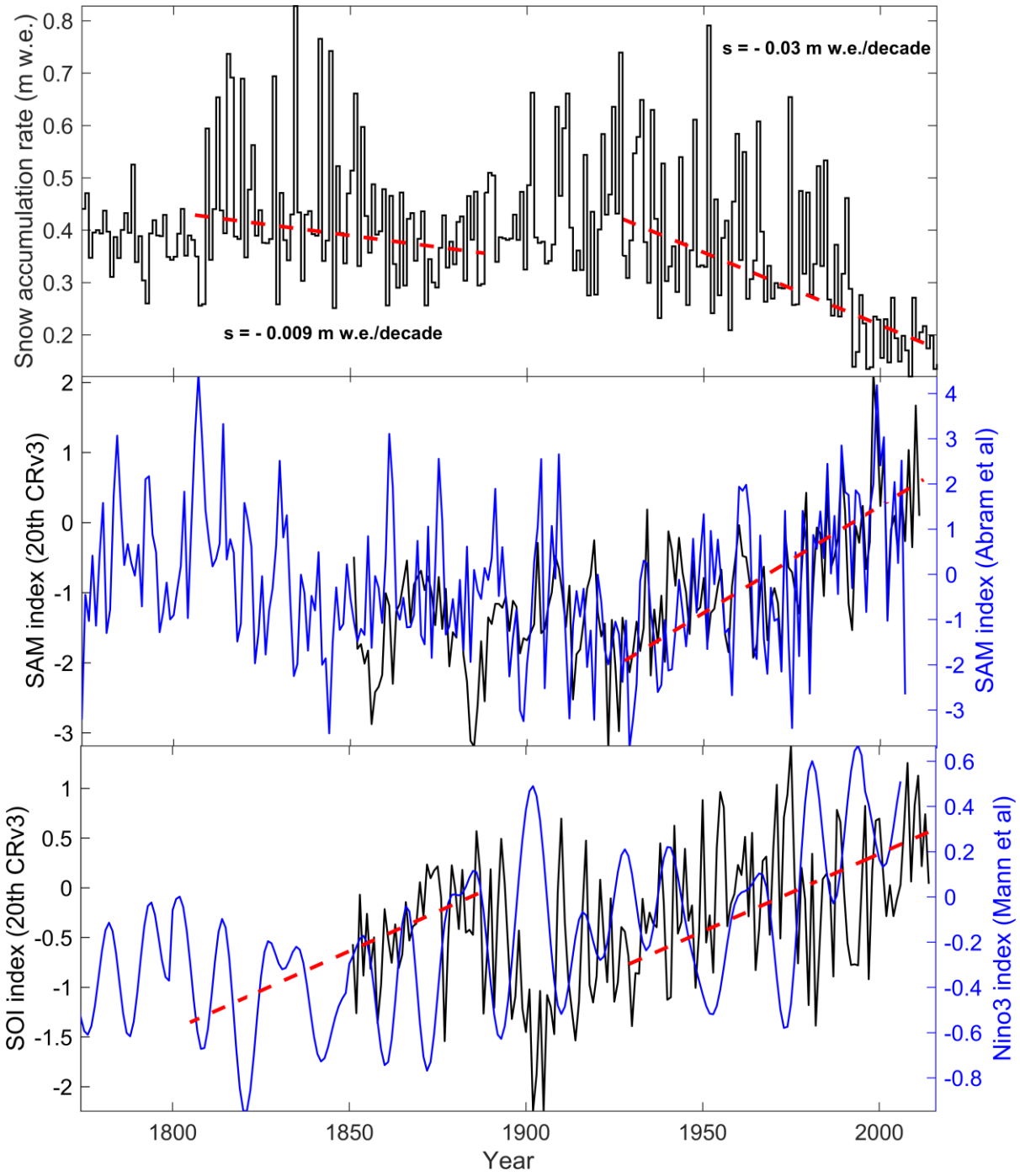

Figure 4.8 (a) Annual snow accumulation rates (black curve) with periods of significant trends marked (red dashed line). Significant trend periods are identified using BEAST algorithm similar to Figure 4.4. **(b)** SAM index from 20th Century Reanalysis (black curve) and Abram et al. (2014)(blue curve). The period of significant trend is marked (red dashed line). **(c)** El-Nino index from 20th Century Reanalysis (SOI Index; black curve) and Mann et al. (2009)(blue curve). Periods of significant trend are marked (red dashed line).

Chapter 5

Surface mass balance and summertime melt history from two coastal ice rises in Dronning Maud Land, East Antarctica

5.1 Introduction

Understanding the mass balance variability is crucial for deciphering the dynamic response of polar ice sheets towards climate change. A key component of the mas balance is the surface mass balance (SMB), influenced by two main components: how much snow accumulates annually (snow accumulation) and how much it melts during the summer (summertime melting). The annual snow accumulation acts like a climate archive, capturing changes in atmospheric conditions over time. It reflects precipitation patterns and provides a timeline of climate variability. On the other hand, summertime melting responds to higher temperatures and solar radiation. The interplay between these two components illustrates immediate climate conditions and offers insights into broader climatic shifts. For Antarctic sites, investigating how accumulation and melting interact is essential for reconstructing the region's climatic past.

Antarctic mass balance is challenging to measure and predict, directly impacting current estimates of sea-level rise and future projections (Fürst et al., 2016; The IMBIE team, 2018; Lenaerts et al., 2019). In the Antarctic coastal regions, ice-ocean interactions, SMB, and buttressing from locally grounded ice rises and rumples all affect ice shelf mass balance, which has a major control on mass discharge from the ice sheet through the grounding line (Matsuoka et al., 2015). SMB is often estimated using regional climate models or satellite observations of passive microwave, which have a spatial resolution of tens of kilometres in most cases (Lenaerts et al., 2017; van Wessem et al., 2018). This is not sufficient to capture the finer-scale topography of ice rises and rumples, which induce considerable local variations in SMB (Lenaerts et al., 2014; Wang et al., 2016; Kausch et al., 2020). Given the high rates of SMB and its high spatial variability due to local topographic variations at these locations, regional SMB estimates are poorly constrained. Moreover, the low elevation of these sites makes them prone to frequent summertime melting. Detailed observational constraints are necessary to evaluate and improve regional climate models.

The coastal region of Dronning Maud Land (DML) in East Antarctica is characterized by numerous small ice shelves bounded between distinct topographic features

(i.e. ice rises) with their own specific local flow, climate regime, and spatially varied SMB (Sinisalo et al., 2013; Lenaerts et al., 2014; Goel et al., 2017; Rignot et al., 2019; Goel et al., 2020). The specific local flow regime typically consists of the ice flowing from the stationary ice dome of the ice rise toward the ice shelf. Both snowfall and redistribution of snow by wind are largely controlled orographically at various spatial scales across the ice shelves and ice rises (King et al., 2004; Favier and Pattyn, 2015; Matsuoka et al., 2015; Callens et al., 2016; Kausch et al., 2020). SMB characteristics near the ice-rise summits are of particular interest since ice rises are close to the ocean and SMB is often much larger than inland sites giving higher temporal resolutions in the paleoclimate proxies over the past several millennia. Spatially resolved SMB at sub-decadal periods are needed to understand recent ice-rise and ice-shelf dynamics, but such ground-penetrating radar (GPR) based records are very limited in DML (Callens et al., 2014; Lenaerts et al., 2014; Goel et al., 2017).

Melt layers, on the other hand, are clear indicators of extreme summer warmth in the polar regions and ice cores drilled from the summit of low-elevation ice rises also provide a detailed record of summertime melting. These refrozen melt layers form when excess energy at or near the surface leads to melting, and meltwater percolates down through the snowpack until freezing at the 0° isotherm (Pfeffer et al., 1990; Pfeffer and Humphrey, 1996; Koerner, 1997; Winski et al., 2012). Upon burial and compaction into firn and ice, these refrozen melt layers are distinguishable as darker layers with few or no bubbles, surrounded by bubbly ice with well-defined grains. While melt layers are subject to uncertainties related to the transport and refreezing of meltwater within the snowpack (Pfeffer and Humphrey, 1996; Pfeffer and Humphrey, 1998), the direct physical link between melt and temperature (Ohmura, 2001) means that melt layers reflect warm season conditions on the ice sheet. This seasonal specificity helps develop climate calibrations and investigate mechanisms of climate change. Although melt can be affected by various factors such as cloud type and surface albedo (Keegan et al., 2014), it has been generally found that melt layers represent summer temperature conditions over the snow/ice surface (Herron et al., 1981; Alley and Anandakrishnan, 1995; Das and Alley, 2008; Kelsey et al., 2010; Abram et al., 2013a).

In this chapter, two ice cores drilled from the summit of two ice rises, viz., Djupranen ice rise (DIR) and Leningradkollen ice rise (LIR) in coastal Droning Maud Land, East Antarctica, were used. Since ice core-derived snow accumulation records are point measurements at specific locations and can be affected by multiple local factors, the ice cores records are combined with GPR surveys for broader spatial coverage. SMB is constrained

by shallow radar reflectors dated with ice core age-depth models. Annual melt estimates are obtained using the line-scan images of the ice cores. These results were compared with satellite and model-based observations over the ice rises. Further, the SMB results were analyzed in relation to surface topography (i.e., elevation) and compared them with SMB estimated with a regional climate model.

5.2 Results

5.2.1 Ice core chronology

The chronology and snow accumulation rates of the ice core from the DIR (IND36/9) is discussed in Chapter 4. Similarly, the age-depth relationship and density profiles of the IND36/10 ice core were used to calculate annual accumulation rates at the LIR (detail description in Chapter 2). The IND36/10 ice core is dated back to 1868 ± 4 years, and the accumulation rate shows large variability, ranging from 0.1 to 0.63 m w.e. with an average accumulation rate of 0.24 ± 0.1 m w.e. (Figure 1.1) over the total time period. The temporal variability in accumulation rates reveals relatively higher values until 1915 CE and thereafter a continuous decreasing trend (1915−2016 CE). The accumulation rate of IND36/10 ice core is consistently lower than that of IND36/9 for the common time period due to the significantly lower elevation of the LIR(170 m a.s.l.) as compared to DIR (326 m a.s.l.).

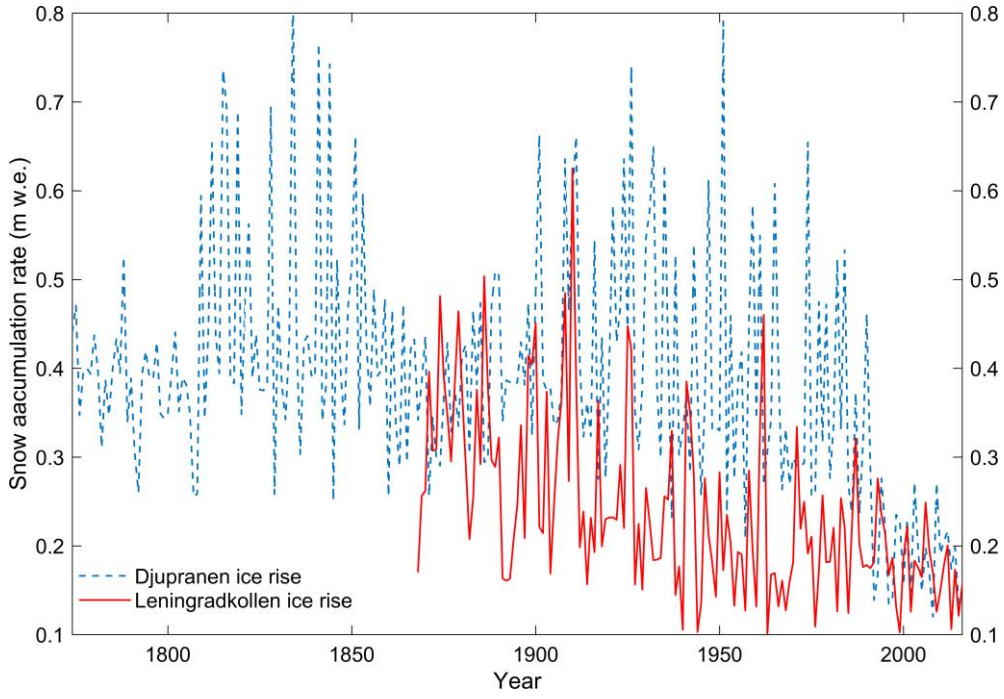

Figure 5.1 Annual snow accumulation for IND36/10 ice core (red curve) and IND36/9 ice core (blue dashed curve)

5.2.2 GPR stratigraphy

The ice radar data clearly shows clear stratigraphy almost all along the radar profiles, both over the ice shelf and ice rises (Figure 5.2b). Englacial reflectors along the 160-km-long profile between the two ice core sites have numerous undulations over short distances, and such undulations are more significant at locations toward the middle of the ice shelf where several ice-flow stripes are present (Figure 5.2a, b). The upper portion of the Nivlisen Ice Shelf experiences extensive surface melting in summer, and meltwater features advect downstream with the ice shelf (Kingslake et al., 2017). However, these melt features are located a few tens of kilometers upstream of our radar profile, and the ice shelf moves less than 100 m a^{-1} in this region (Rignot et al., 2011). The radargrams does not reveal any major stratigraphic disturbances caused by meltwater (Figure 5.2). On the eastern side (20 – 60 km from the Leningradkollen core site), the reflectors are relatively smooth with little variation in depth. However, the reflectors become deeper towards the western end of the ice shelf (> 70 km).

The study tracked six reflectors from the Leningradkollen ice core site towards the ice shelf. The reflectors are down-warped for ~1 km near the grounding line, with presence small surface cracks. Nonetheless, radar reflectors are still traceable (Figure 5.2d). These reflectors deepen towards the west, so the deepest three reflectors fall outside the radar's depth window at locations of ~70 – 140 km west of Leningradkollen (Figure 5.2b). At the Djupranen grounding line (Figure 5.2c), the reflector down-warping is more pronounced than at the Leningradkollen grounding line, and it was not possible to confidently track the top three reflectors across the grounding line. Here, crevasses were observed that are ~40 m deep and 2-3 m wide, which needed to be filled with snow to continue the over-snow traverse to the Djupranen Ice Rise.

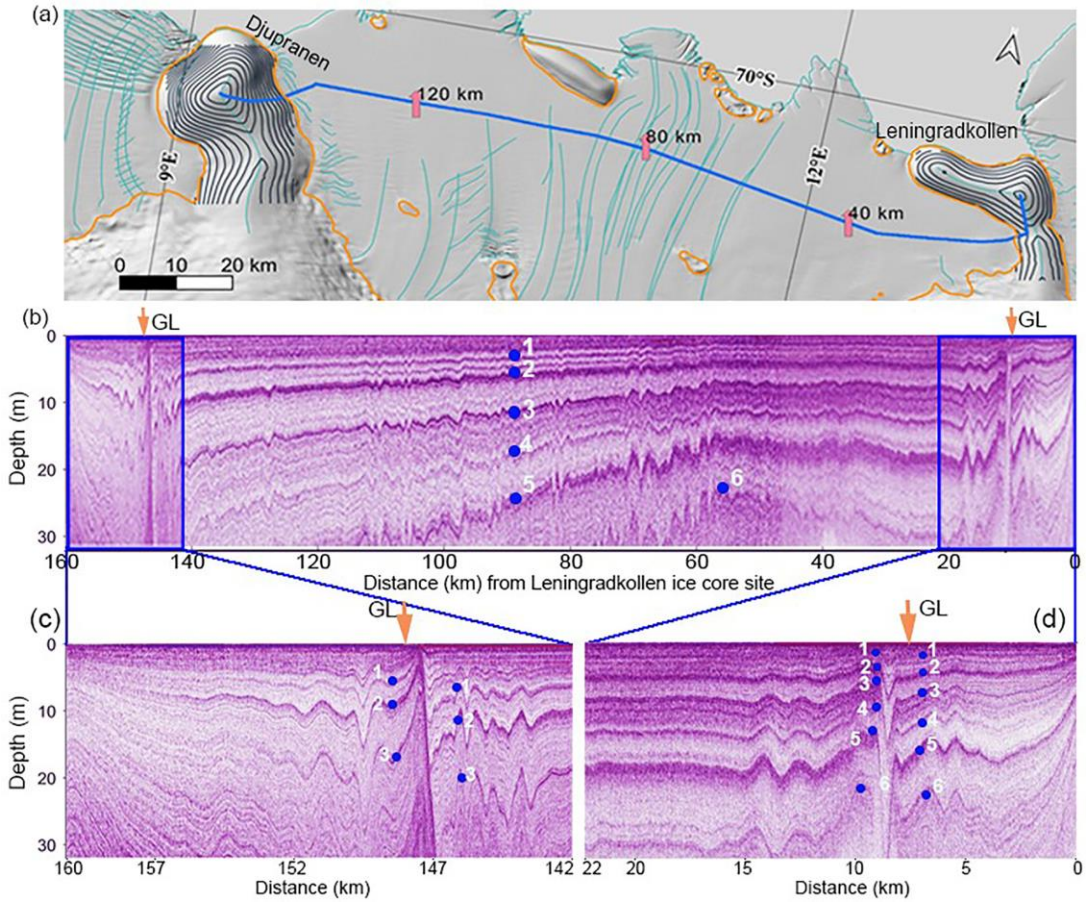

Figure 5.2 Firn stratigraphy detected with 250-MHz radar frequency. **(a)** Location of the radar profile in panel **(b)** shown together with ice surface features (Goel et al., 2020) and surface elevations of 20 m contour intervals reconstructed from the GNSS survey over the ice rises. Continental grounding line and ice rise outline were taken from (Bindschadler et al., 2011; Moholdt and Matsuoka, 2015), respectively. Pink markers show the distance from Leningradkollen core site along the profile. The background image is a hill-shade extracted from the Reference Elevation Model of Antarctica (REMA; Howat et al. (2019)). (b) Radargram across the ice shelf between the ice core sites at the summits of the two ice rises. The down-pointing arrows show the grounding line positions (GL; Bindschadler et al. (2011)). Close up views of the profiles between the core sites and GL regions are shown in panels **(c)** and **(d)**. Blue dots indicate the six reflectors tracked and dated using the ice.

The six reflectors tracked along the transect were dated as 3.7, 6.9, 11.3, 17.6, 23.7, and 30.9 years before December 2017 using the Leningradkollen ice core. Because the reflectors are not readily traceable over the Djupranen grounding line (Figure 5.2d), similarly prominent reflectors were picked up at the ice-rise side of the grounding line and tracked them to the Djupranen ice core site. These three reflectors are dated as 5.5, 7.1, and 12.2 years before December 2017 using the Djupranen ice core. As there are no other reflectors close to these depths that can be tracked for long distances from this grounding line, it is presumed that these three reflectors are identical to those tracked from the Leningradkollen

Ice Rise. In that case, the difference in ages of these reflectors (0.2 – 1.8 years) may be associated with uncertainties in ice core chronology and in radar reflector tracking, which are discussed in Section 5.2. Three more reflectors were picked over the Djupranen Ice Rise, which are dated as 20.4, 25.4, and 27.4 before December 2017. Separately, five reflectors were tracked over the LIR that are dated as 4.5, 8.3, 14.9, 19.7 and 29.3 years before December 2016. These reflectors give the best clarity and extent over the ice rises where the snow depositional conditions are much more variable than on the ice shelf.

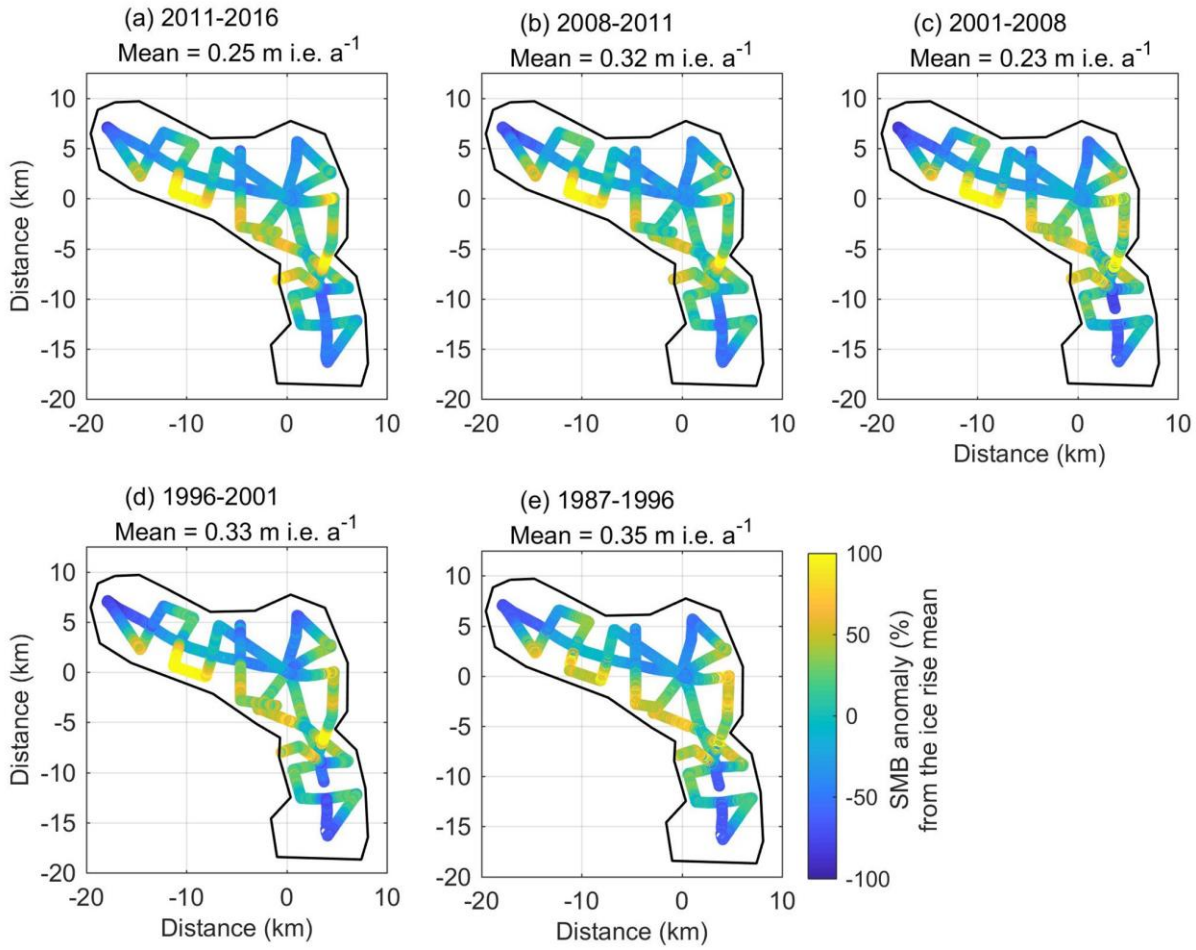

Figure 5.3 Overview of the spatial SMB variability relative to the mean SMB for the LIR during five different time periods. The mean annual SMB for each period is given above each panel and listed in Table 5.1.

5.2.3 SMB derived from radar data

Over the Leningradkollen Ice Rise, SMB was derived using the five reflectors spanning periods of 3 – 9 years between 1987 and 2016. Mean SMB over the ice rise ranges between 0.23 to 0.35 m i.e. a^{-1} over the five periods, while the spatial variability of SMB is large but relatively stable between periods (Figure 5.3). Lower SMB is found in the northern

slope of the east-west ridge, and the northeast side of the ice dome. There, SMB is only one-quarter of the ice-rise mean values. Correspondingly, higher SMB values were found in the southern slope of the east-west ridge, and the saddle between the seaward dome and the landward promontory. Across the east-west ridge, SMB varies by more than ±50% of the ice-rise mean within 10 km from the northern side facing the open ocean to the southern side facing the ice-shelf inlet.

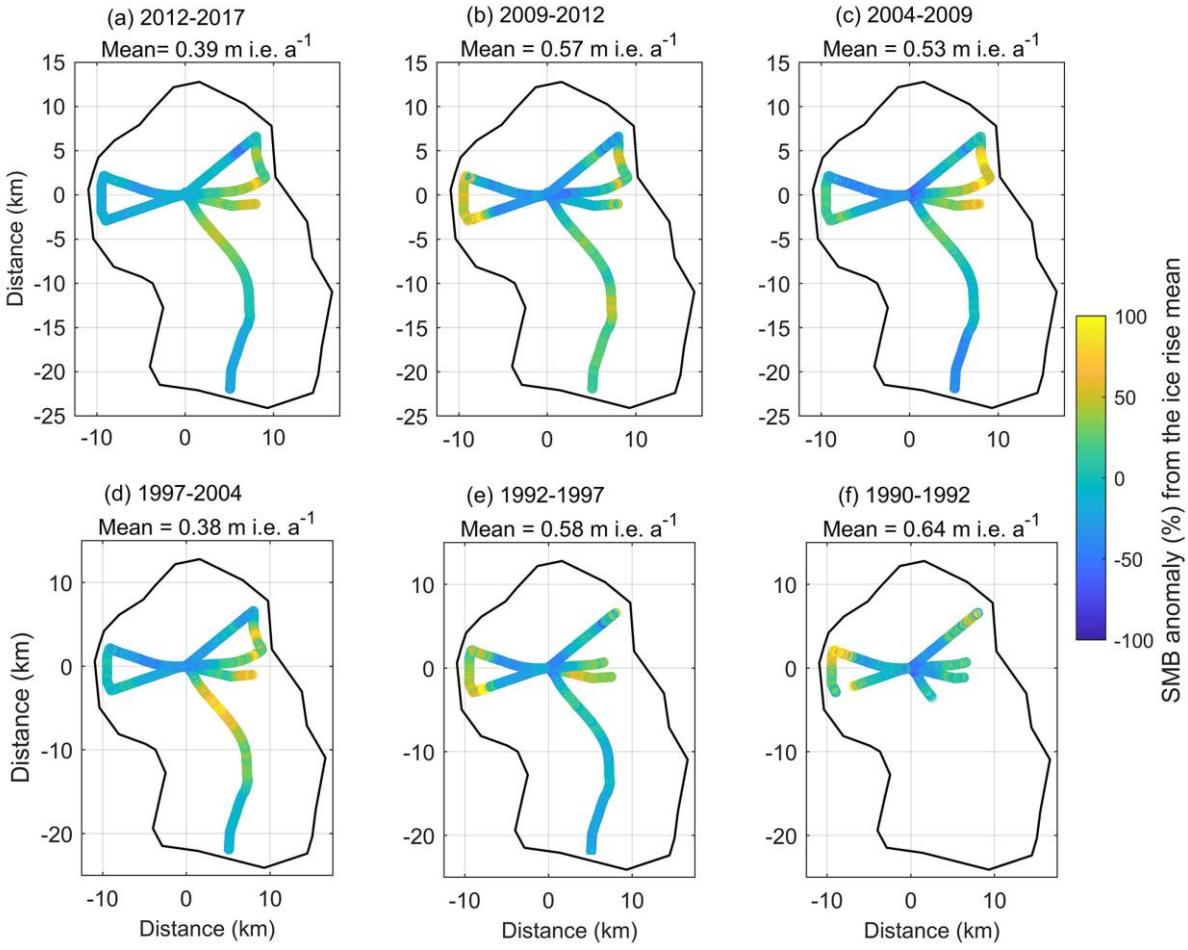

Figure 5.4 Overview of the spatial SMB variability relative to the mean SMB for the DIR during six different time periods. The mean annual SMB for each period is given above each panel and listed in

At Djupranen Ice Rise, SMB estimated over six periods spanning 2 – 9 years between 1990 and 2017 (Figure 5.4). The regional-mean SMB over DIR varies between 0.38 and 0.64 m i.e. a^{-1} over these periods, which is much larger than temporal variations of ice-rise mean SMB observed over LIR (Table 5.1). Anomalously high SMB is found near the grounding line east of the ice rise, which is the upwind side. Except for this, the spatial patterns over DIR are less persistent over time than those over Leningradkollen Ice Rise. For example,

high SMB is observed near the western, downwind grounding line for a few periods, but not for all periods. Similarly, SMB along the ridge from the seaward dome to the ice sheet is smaller for a few periods, but not for all periods. SMB for the 1990 – 1992 period is estimated only in small areas over the ice rise because the deepest reflector dated at 1990 CE deepens out of the radar window (to the depth ~35 m). In general, the ice rise has an east to west SMB contrast. The SMB over the eastern side of the ice rise is about 50 – 100% higher than the ice-rise mean.

Table 5.1 Summary of the regional-mean SMB derived with the radar data for the last three decades. Mean of RACMO2.3p2 SMB values are also shown for comparison. The radar-derived SMB values shown with * are derived only in a limited area of each region. RACMO results are available only to 2015, which are shown with # in the table. Nominal uncertainty of radar-derived SMB is ±11%.

Region	**Lower bounding Reflector ID**	**Period**	**GPR derived region mean SMB (m i.e. a^{-1})**	**RACMO2.3p2 modelled SMB (m i.e. a^{-1})**
Leningradkollen Ice Rise	1	2011–16	0.25	0.26#
	2	2008–11	0.32	0.29
	3	2001–08	0.23	0.24
	4	1996–2001	0.33	0.28
	5	1987–96	0.35	0.27
Djupranen Ice Rise	1	2012–17	0.39	0.50#
	2	2009–12	0.57	0.69
	3	2004–09	0.53	0.51
	4	1997–2004	0.38	0.69
	5	1992–97	0.58*	0.65
	6	1990–92	0.64*	0.61

5.2.4 SMB uncertainty due to variable firn density and densification

Surface density (mean in the top 1 m) were measured at 11 sites varies between 430 and 450 kg m^{-3}, or ±5%. The uncertainties in core diameter (±0.1 cm), core-length measurements (±0.3 cm), and weight measurement (±5 g) result in propagated uncertainty

of 4% in density of a 1 m snow core. Uncertainty of the stake heights is less than ±1 cm or 1.2% of the mean height difference. Although representative surface is chosen in its vicinity to install the markers, but local variability of SMB associated with microtopography cannot be evaluated. Therefore, stake-measured SMB has an uncertainty better than ±5%.

Uncertainty in the radar-derived SMB values is related to uncertainties in ice-core density and chronology, and uncertainties in the two-way travel time of reflectors. The density of the ice core samples was measured in a cold room; the error in measuring the dimensions (5×5×3.5 cm) of the samples was ±0.5 mm and the uncertainty of the weighing balance was ±0.1 g for measured mass up to 100 g of snow/firn. It results in a propagated uncertainty of 5% in the ice core density measurements. For the top 15 m snow/firn column of ice core, the uncertainty in chronology using independent methods is ±1 year, calculated as the difference between the minimum and maximum age estimates at a particular depth point. This is supplemented by the observation that the ages of the three shallowest reflectors dated by the two ice cores differ by 1.8, 0.2, and 0.9 years. This uncertainty affects the magnitude of SMB for corresponding periods but does not affect the spatial patterns of SMB.

Another uncertainty in the radar-derived SMB values is from the assumption of laterally uniform density. It is assumed that the density varies with depth as observed in the Djupranen ice core but does not vary laterally. This was examined in two ways. First, the study used Djupranen (instead of Leningradkollen) ice core density to calculate depths of tracked reflectors, assign the new ages of these reflectors using the Leningradkollen or Djupranen ice cores (as done in the primary analysis), and calculate SMB using the Djupranen (instead of Leningradkollen) ice core depth density data. The density profiles from the two ice rise summits are similar and have no systematic bias to each other; the density difference between the two cores at a given depth is 25 kg m^{-3} on average, and the standard deviation of this difference is ±46 kg m^{-3}. This brings an uncertainty of 5% between two ice core densities. The radio-wave propagation speed averaged from the surface to 10 m depth derived with the Djupranen density differs by 1.4 % from our original estimate. However, this variation in the radio-wave propagation speed causes no change in the age estimate from the original ages. As a consequence, similar SMB is found for all reflectors with no change in spatial patterns. The surface density to 3 m ranges from 465 kg m^{-3} at the LIR summit to 505 kg m^{-3} at the western side of DIR with a mean and standard deviation of 484 ±12 kg m^{-3}.

To evaluate the uncertainty in reflector tracking, cross-over analysis was carried out. There are 15 cross-over sites over LIR, and 3 sites over Djupranen Ice Rise, whereas the ice shelf has no cross-over profile. At these 18 locations, the mean cross-over error is 1.0 ns (or approximately 10 cm in firn) with a standard deviation of 0.4 ns (4 cm). This mean cross-over error constitutes 6% of the depth uncertainty for the shallowest reflector but the relative magnitude is smaller for deeper reflectors. Combining the sources of uncertainty as a root-sum-square, an uncertainty of ±11% was determined for the radar-derived SMB estimates. Local SMB uncertainties might be higher than this due to unaccounted density variations in areas such as the ice shelf margins and the high-accumulation zone near DIR.

5.2.5 Annual melt estimation from line scan data

Melt layers are observed in 175 out of 249 years in IND36/9 and 124 out of 149 years in IND37/B10 ice core (Figure 5.5). Some sections of the cores show several ice layers clustered together, while in other places, only single and relatively thin yet distinctive layers are found. Layers covering at least 50% of the scanned section width were considered as a melt layer. As melt layers are advected downward, they thin along with the surrounding ice matrix, such that melt layers deeper in the core may be many times thinner than when they were formed near the surface (Das and Alley, 2008). This is corrected using a thinning function following Nye (1963); however, it is worth noting that the thinning of the deepest layers is less than 10%. Using the thinning function, the thickness of each melt layer is adjusted to its original surface thickness. To interpret these results in terms of local climatology, an age is assigned to each melt layer using the depth-age scales for the respective ice cores. This allows us to calculate the total amount of melt during each calendar year. For each year, all melt layers (1 through n) of thickness λ_i are added. Layer thicknesses are then scaled by the density of ice ρ_{ice}. Several large melt events are observed in both the ice cores over the instrumental observation period. For example, the largest melt event in the IND36/9 ice core is observed in 1985, which is also present in the IND36/10 ice core. However, the 1985/86 melt event in IND36/10 ice core is not the largest, but there is continuously high summertime melting recorded during these years. This is consistent with previous observations from the nearby S100 ice core and nearby Novolazarevskaya station data (Kaczmarska et al., 2006). However, a strong correlation is not observed between annual melt and mean summer temperature. Since the mean summer temperature might not necessarily indicate favourable melting conditions, 3-hourly temperature outputs from UK Met Office Unified Model (METUM) version 11.1 regional atmospheric model is used. As

van den Broeke et al. (2004) pointed out, the best indicator of melting would be the number of hours with positive air temperatures throughout the season. Since temperatures from METUM are available at 3-hour time steps, it is difficult to compare between temperatures and melt layer proportions due to the short melting intervals in a day. No direct connection between the melt layer proportions derived from the ice cores and the positive degree hours (PDH; Figure 5.5a) is observed. For example, the PHD values during the years 2004 – 2006 is higher than those observed during 1985 – 1987, but the melt proportions are much higher during 1985 – 1987. On a decadal scale, an increasing trend is visible in summertime melting over the 20th century (Figure 5.5b). However, the average melt is significantly lower from 1980 to 2000 CE at both ice core sites, after which it increases again. Similar trends are also observed from regional atmospheric model simulations (Orr et al., 2023). The trends are however always larger for the IND37/B10 ice core as compared to the IND36/9 ice core.

5.2.6 Uncertainty in melt estimation

When a melt lens is situated behind air bubbles or oriented perpendicular to the imaging plane, it can pose challenges in visibility within the 2D line scan images, often leading to potentially missing entire layers. However, significant events are unlikely to be overlooked in the analysis since they are readily apparent in line scan images. Further, the analysis was repeated twice to reduce the potential for manual errors. Additionally, it is worth noting that the limited diameter of the ice core can result in the omission of bubble-free layers within the ice sheet's stratigraphy, given that the spatial distribution of a melt lens or layer is not uniform over larger areas, it is essential to recognize that the ice core, with a diameter of 10 cm, represents a relatively narrow sample of the overall ice column. Keegan et al. (2014) have shown that significant melt events, such as the one in 1889 CE in Greenland, are observable in most shallow cores and snowpits, indicating their widespread occurrence. Consequently, for more substantial events, it can be reasonably assumed that the analysis is representative of the majority of the regions. However, it is important to acknowledge that smaller events may be localized to the particular ice core site.

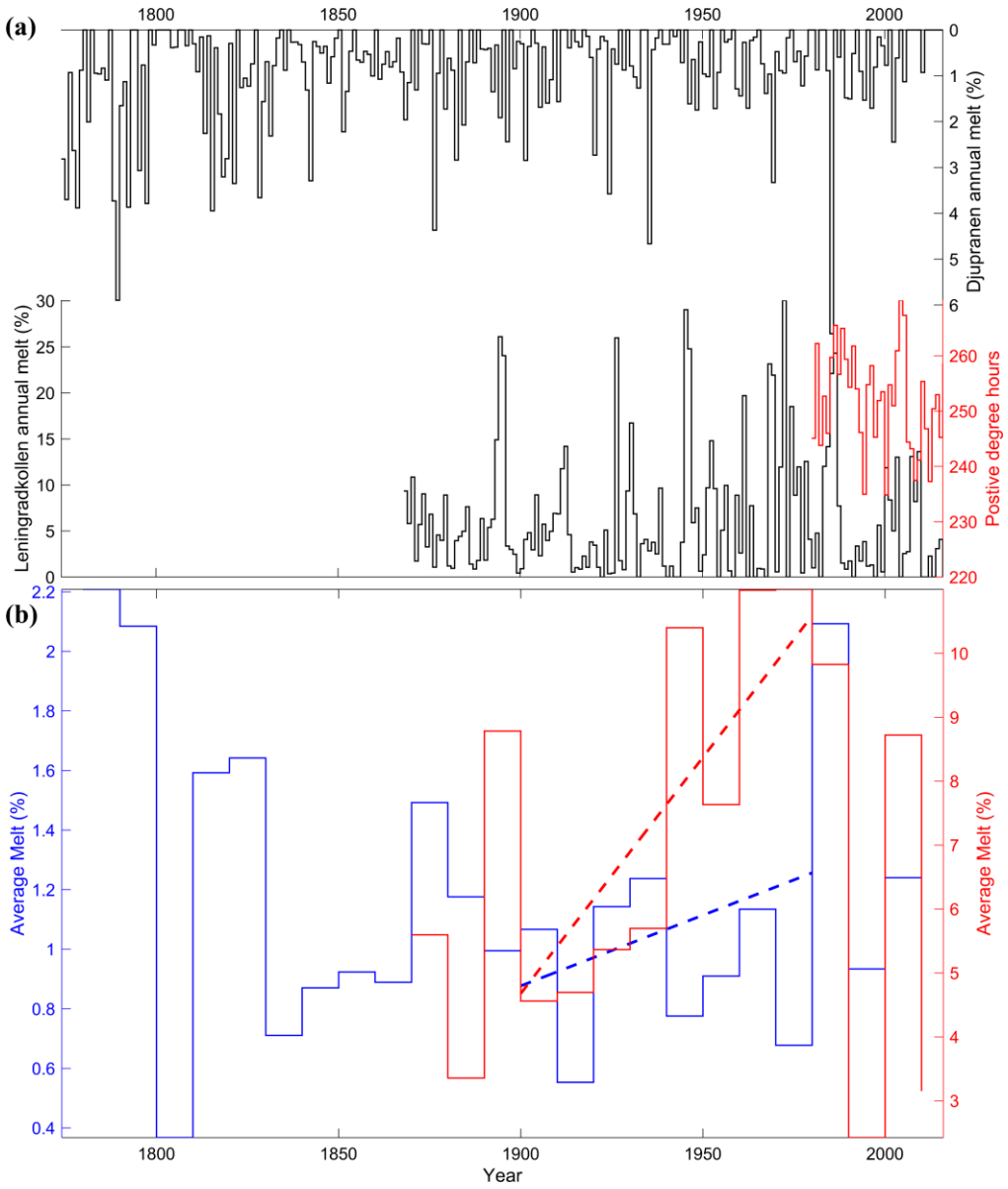

Figure 5.5 (a) Annual melt proportion from IND36/9 (upper panel) and IND36/10 ice core (black curve; lower panel). Annual positive degree hours (PHD) are shown using the red curve in the lower panel. **(b)** Decadal average melt from IND36/9 (blue curve) and IND36/10 (red curve). Dashed lines represent the significant trend between 1900 to 1980 CE.

5.3 Discussion

5.3.1 Spatial SMB pattern

The Antarctic coast is characterized by varying surface topography that interacts with wind and moisture to promote precipitation and snow redistribution, resulting in an inhomogeneous distribution of SMB (Lenaerts et al., 2012; Rignot et al., 2019). Elevation differences between ice shelves and ice rises play an important role in controlling spatial SMB distribution in the coastal DML region (Lenaerts et al., 2014; Drews et al., 2015). This

study revealed a strong east-west SMB gradient over the Nivlisen Ice Shelf with local variations being 1 – 2 orders of magnitude smaller than the regional variation. Such a large and monotonic difference is potentially caused by a strong regional orographic effect of the Leningradkollen and the Djupranen ice rises, similar to those observed at other Antarctic ice rises (King et al., 2004; Lenaerts et al., 2014).

While large-scale surface topography dominates SMB variations, notable small scale <500 m SMB undulations were also observed. These undulations have SMB amplitudes of 0.05 – 0.2 m i.e. a^{-1} over a length of 500 m. The east-west profile over the ice shelf crosses along-flow stripes seen in satellite imagery, and ice surface depressions of 4 – 7 m were also observed at many of these locations at the downstream of mid-ice shelf rumples spread over 10 km along the profile at 60 – 120 km from the Leningradkollen Ice Rise. Local SMB anomalies have been observed over similar local topographic features in other parts of Antarctica (Drews et al., 2015; Drews et al., 2020; Kausch et al., 2020). In an attempt to explore small scale variations, local anomalies in SMB were determined together with surface elevation. This revealed a spatial correspondence between the resulting surface and SMB anomalies, with surface undulations of 10 – 25 cm leading to SMB variations within 5 – 15 mm i.e. a^{-1}. However, as the scale of these variations is within the uncertainty range of these data, conclusive inferences cannot be made. The SMB variations on the ice rises are more complex but relatively stable over time which indicates persistent climate conditions with respect to surface topography, at least for the Leningradkollen Ice Rise. At the larger scale, both ice rises act as wind barriers against the dominating easterly winds, with the majority of the precipitation coming from northeasterly storms.

5.3.2 Comparison with a regional climate model

Regional atmospheric climate models often have a spatial resolution of tens of kilometers, which is typically too coarse to fully resolve individual ice rises along the coast. Along the DML coast, the regional climate model RACMO2.3p2 ANT/DML is available with a spatial resolution of 5.5 km from 1979 to 2015 (Lenaerts et al., 2017). This model resolves most of the promontories and several isle ice rises, although their surface topography is coarsely prescribed.

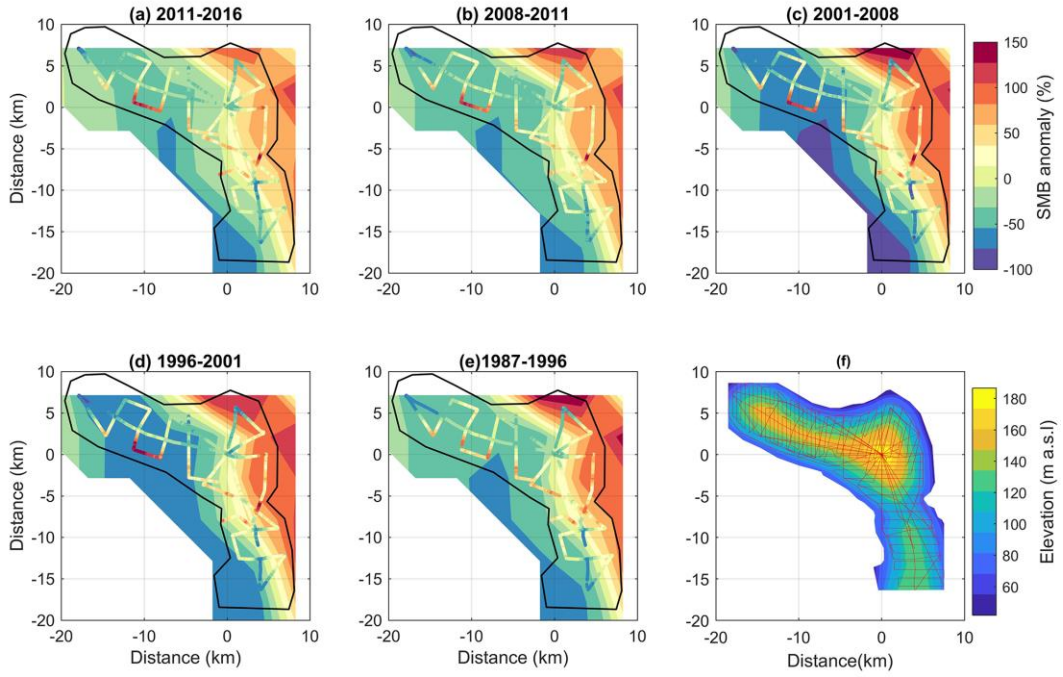

Figure 5.6 Overview of SMB anomaly over five periods **(a-e)**, and ice-surface topography of LIR(f). **(a-e)** Stripes show radar-derived SMB and background shows model-derived SMB, both as percentage anomalies from each ice-rise mean. **(f)** Ice surface elevation interpolated from GNSS survey (red lines).

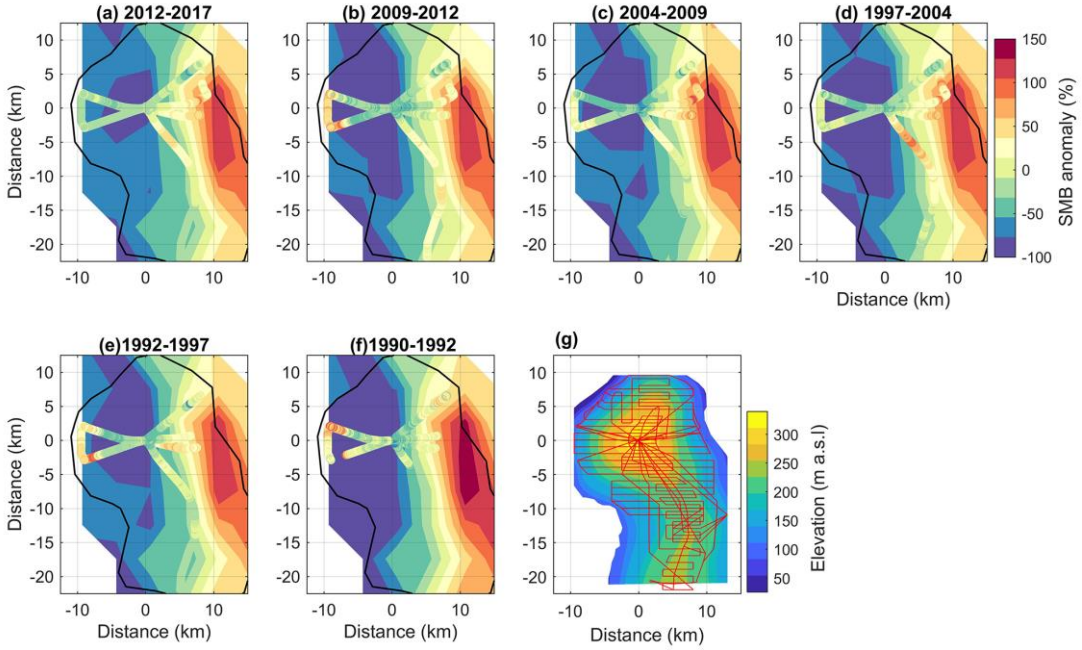

Figure 5.7 Overview of SMB anomaly **(a-f)** and ice-surface topography **(g)** of the Djupranen Ice Rise. **(a-f)** Stripes show radar-derived SMB and background shows model-derived SMB,

both as percentage anomalies from each ice-rise mean. **(g)** Ice surface elevation reconstructed from GNSS survey (red lines).

To compare the observed and modelled SMB, a distance-weighted mean of modelled SMB was derived at each radar point using the model's four closest cells. RACMO2.3p2 SMB could be extracted for all radar SMB periods except that RACMO2.3p2 only extends to the end of 2015. For DIR a total of 55 RACMO2.3p2 grid cells are obtained, and for Leningrad Ice Rise a total of 33 grid cells (Figure 5.6 and Figure 5.7). The RACMO2.3p2 SMB indicates consistently lower SMB on the leeward (western) side, whereas the radar-derived SMB show more complex patterns and smaller-scale variability.

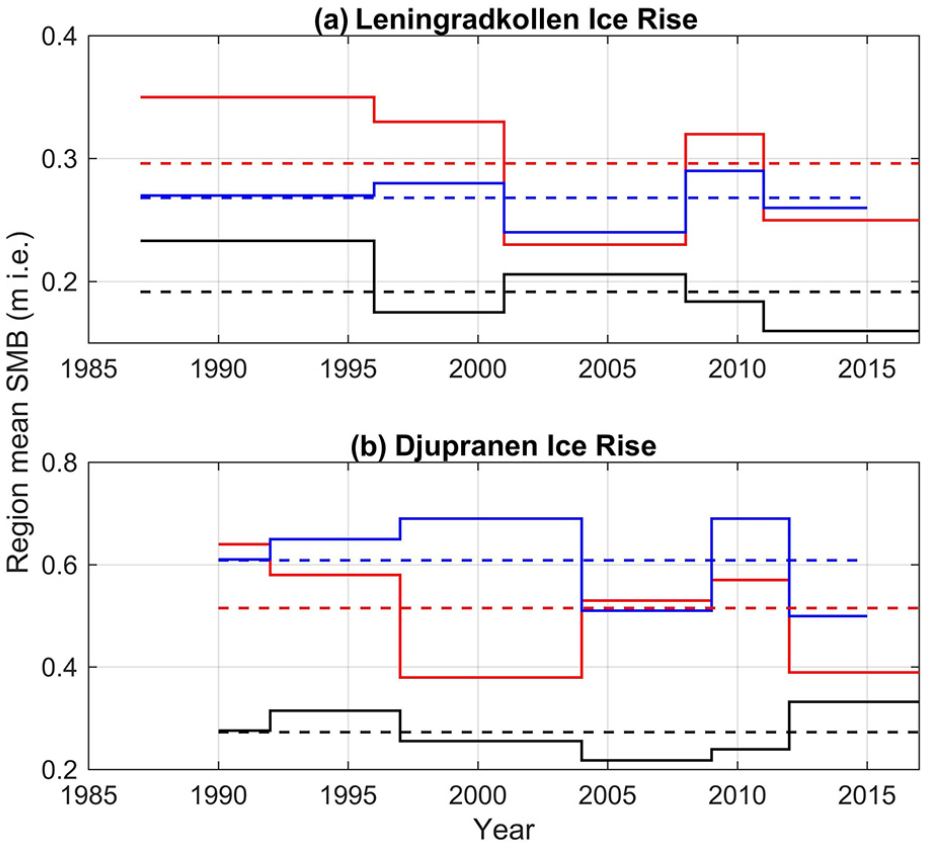

Figure 5.8 SMB changes in the past three decades over the **(a)** Nivlisen Ice Shelf, **(b)** LIR and **(c)** Djupranen Ice Rise. In each panel, red lines show radar-derived SMB, and blue lines show RACMO2.3p2 modelled SMB (RACMO data are available only to 2015), both averaged over these regions. Black lines in the panels **(b)** and **(c)** show SMB at the ice-rise summits derived from the ice cores. Dashed horizontal lines show the mean over the entire period obtained from these three methods.

Since the RACMO2.3p2 model has a 5.5-km cell size, any orographic effect is modelled only for approximated topography, which could be the main cause of discrepancies between modelled and observed SMB patterns. Therefore, SMB values averaged over the

ice shelf and each ice rise were compared (Figure 5.8 and Table 5.1). These regional mean values are derived from all measured SMB values and all modelled SMB values constructed at the radar-observation locations. Ice core SMB represents only the vicinity of the ice rise summit. When these mean values are averaged over the entire period, modelled SMB values are smaller than radar-derived SMB values over the ice shelf and LIR by about 20 – 50%. Modelled SMB values are smaller than radar-derived SMB values for most of the individual periods, but the magnitude is different. Over DIR, modelled SMB values are larger than radar-derived values, but less than 20% different. This magnitude relation remains the same for individual periods in most cases. Further, the ice-core SMB values are 50 – 80% smaller than the radar-derived and modelled SMB for both ice rises. A large temporal variability has been observed among all SMB observations, which has been explained mainly by topographic differences of the ice rises and the surrounding ice shelf (Kausch et al., 2020). This study revealed that the ice-core records from the ice-rise summits do not necessarily represent ice-rise-wide SMB changes, and also climate models do not match either the core-based SMB at the summits or radar-derived SMB over the ice rise.

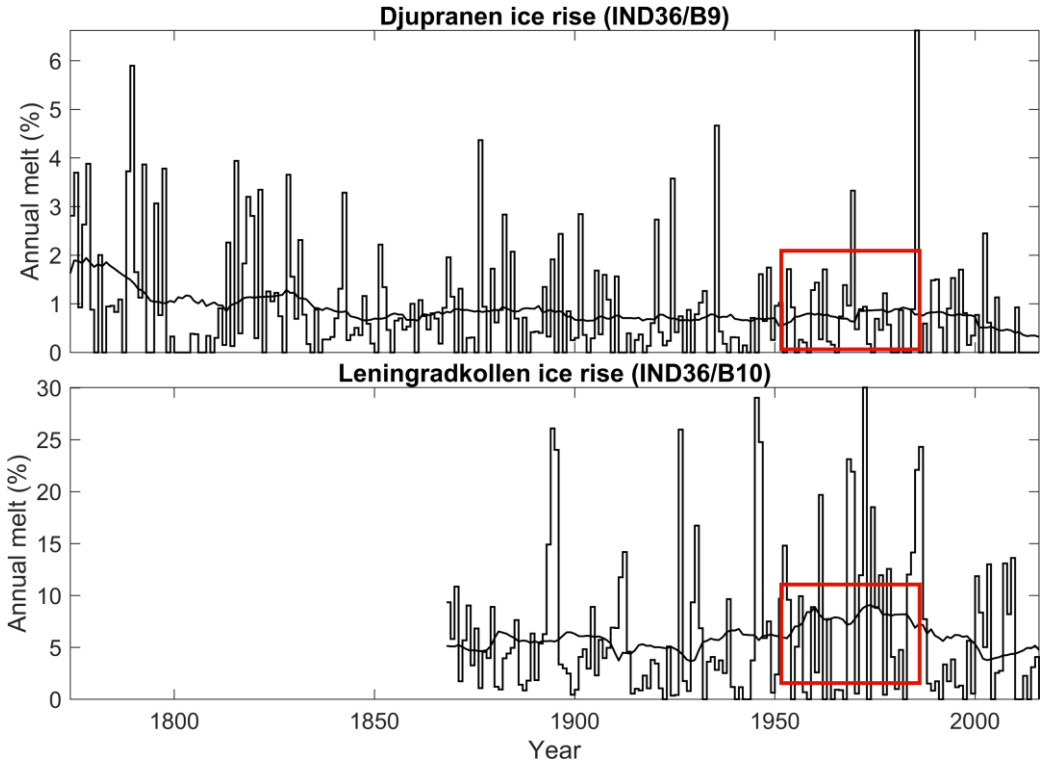

Figure 5.9 Annual summertime melt (black curve) and 30-year running mean of annual summertime melt (thick black curve) for the two ice cores. The red box shows a period of increased melting in the IND36/10 ice core which is not reflected in the IND36/9 ice core.

5.3.3 Summertime melting over the past centuries

The IND36/9 and IND36/10 ice core records show no direct control of PDH or temperature on the observed annual melt proportions. The observed heterogeneity in between the melt records from the two ice rises (Figure 5.9) could be attributed to the elevation difference. The lower elevation of LIR has significantly higher melting proportion (up to 30%) compared to the higher-altitude DIR site (<7%), accentuating the effects of even the smallest melt events . This elevation-induced amplification underscores the need for a nuanced interpretation of the melt records, taking into account the topographical influences that contribute to the observed heterogeneity. The elevation-induced amplification at LIR also results in stronger trends in summertime melting on a decadal timescales. Another factor to consider would be the localized melt events that are not substantial on the regional scale.

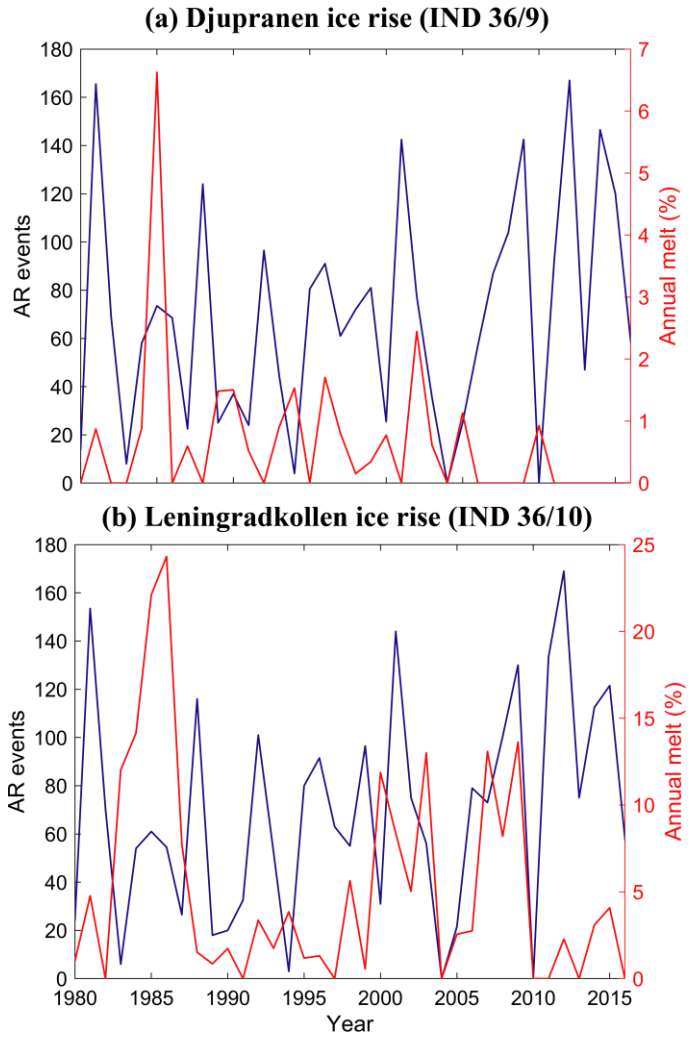

Figure 5.10 Annual melt from ice core and AR events on the Djupranen ice rise **(a)** and Leningradkollen ice rise **(b)**.

The occurrence of summertime melt on the Dronning Maud Land (DML) coast has proven challenging to explain using traditional climate data and proxies derived from ice cores (Kaczmarska et al., 2006). The microclimate at the core location and the morphology of the local snow surface are important factors in controlling the variability of interannual melts (van den Broeke et al., 2004) and are difficult to constrain from reanalysis datasets. However, understanding whether a melt event is local or regional would require a network of firn/ice cores. Due to frequent precipitation events caused by cyclonic systems passing through, and air temperatures rising above 0°C during summer months, it is also reasonable to assume that some precipitation may be in the form of rain (Vignon et al., 2021). This can lead to the freezing of both raindrops and meltwater within the snowpack, creating ice layers, which are indifferentiable from each other. The penetration of shortwave radiation also may cause sub-surface melting, while the surface remains frozen due to outgoing long wave radiation (Liston et al., 1999).

Additionally, it has been observed that snow precipitation in the summer can increase surface albedo and reduce ablation. van den Broeke et al. (2004) report high spatial and temporal variations in albedo and surface radiation balance for coastal DML, despite having a seemingly homogeneous snow surface. This suggests that differences could be explained by cloud cover, snow age, and solar zenith angle, as clouds play a crucial role in temporal albedo variations. A strong correlation has been observed between albedo and cloud cover, which offsets the warming effect that clouds usually have over highly reflective surfaces. Furthermore, clouds and precipitation events are frequent in the coastal region of DML, and near the coast, sublimation and melt cause extended periods of surface ablation in summer (van den Broeke et al., 2004; Lenaerts et al., 2016).

Many of the melt periods observed in our ice cores also coincide with documented evidence of atmospheric rivers (ARs) landfall over the ice rises (Figure 5.10). ARs are narrow bands of increased water vapor transport, which transport heat and moisture from mid to high latitudes and are known to potentially trigger melting events in Antarctica (Nicolas et al., 2017; Turner et al., 2022). Wille et al. (2019) showed that between 40-80% of the surface melt on the western Antarctic Peninsula between 1979 and 2017 was caused by ARs that made landfall during winter months (March – October). The yearly AR occurrences calculated from the ARTMIP dataset (Shields et al., 2018; Rutz et al., 2019) shows that the strongest melt features in the ice cores were associated with increased ARs during the year. However, the years with most ARs were not necessarily the years with most

melt. The physical mechanisms relating ARs to surface melt are complex and are beyond scope of this study. Therefore interpreting summertime melt in ice core records is highly complex due to the multiple interplay of factors involved.

Chapter 6

Summary and conclusions

This thesis addresses the potential and challenges involved in the reconstruction of climatic history using ice cores from coastal Antarctica. Ice cores drilled from the summit of two coastal ice rises fringing the Nivlisen Ice Shelf in Dronning Maud Land (DML) were studied to obtain valuable insights into the past climate and sea ice dynamics of the region. The proximity of the ice rises to the open ocean poses a challenge for employing traditional ice core proxies for annual layer counting. To overcome this, this study explores the application of visual stratigraphy records obtained from line-scan images of the ice cores to establish a reliable chronology and as a proxy for climate variability. Visual stratigraphy, together with the traditional proxies, is used to establish a robust chronology for the ice cores. Down core variations in the annual flux of Na^+ is used to reconstruct the sea ice variability over the coastal Antarctica during the past ~250 years. The reconstructed sea ice variability record is the longest from the DML region. It provides valuable insights into the past changes in the sea ice cover over the King Haakon Sea, and its linkages with the well-known climatic modes like Southern Annular Mode (SAM) and El Niño Southern Oscillation (ENSO). This study also uses line-scan images of the ice cores to obtain annual summertime melt histories over the two ice rises and reconstructs the longest melt history from the region. On an annual timescale, no linear relationship exists between temperature with the annual melt records reconstructed from the ice cores, indicating the complex factors influencing the surface melt and its past variability. Comparison between the snow accumulation records of the coastal ice rises studied here and that reported in literature indicate the influence of localised extreme events and maritime processes governing the accumulation trends in the coastal Dronning Maud Land (DML).

The key findings of this doctoral thesis are summarized in the following sections.

6.1 Application of visual stratigraphy from line scan images to constrain chronology and summertime melting

Traditional methods of annual layer counting using stable isotope and major ion chemistry records are laborious, potentially susceptible to artefacts related to summertime melting and harder to interpret for annual layer counting in the coastal region due to the proximity to the maritime processes, increased summer warmth and the influence of storm

activities. Visual stratigraphy profiles reconstructed using line-scan images from the firn section of an ice core are proposed as an important supplemental dating tool in coastal regions of Antarctica. Also, visual stratigraphy profiles can be used to develop a preliminary chronology in a short analysis time, while the other chemical and isotope methods require more time and resources to acquire. The visual stratigraphy profile of the firn section of the ice core is dominantly affected by the temporal changes in density, but automated signal extraction procedures can separate it to distil the seasonal signals attributed to the dust and sea salt inclusions. The line scan images can also be used to identify and quantify the melt layers routinely noticed in ice cores from low elevation sites of Antarctica. Such melt layers can be appropriately masked during the pre-processing of the line scan images, enabling us to reconstruct the chronology of ice cores from coastal Antarctica. This study demonstrate that quantifying annual melt proportion using only the thickness of the melt layer can lead to overestimations and propose using the melt layer polygon area for calculating annual melt proportions. The reconstructed visual stratigraphy profile of the top 50 m section of an ice core from coastal Dronning Maud Land revealed an excellent match with the chronology of the ice core based on a multi-proxy approach, supported with independent age markers of volcanic events and tritium anomaly, with the highest error being ±2 years for the past century. This study concludes that ultra-high-resolution visual stratigraphy records could be valuable in reconstructing the chronology of ice cores from coastal Antarctica.

6.2 Sea ice variability over the King Haakon Sea for the past ~250 years

A 122m long ice core (IND36/9) from the summit of Djupranen ice rise in coastal DML is used to reconstruct the past sea ice variability and annual snow accumulation rates and to understand the role of large-scale climatic factors in controlling the sea ice variability and snow accumulation in the study area. A significant positive correlation between annual Na, Ca and Cl records and winter (JJA) SIC over the King Haakon Sea is observed, both using concentration and flux. To reconstruct the past SIC variability, log-transform of annual Na_{flux} is used, which is the most reliable proxy available at the ice core site. The long-term trend is separated using circulant single-spectrum analysis, which gets rid of the additional noise in the dataset. The first four reconstructed components together explain 83% of the total variability in the annual Na_{flux} record and have a significant positive correlation with the mean JJA SIC during 1979 to 2016. Geometric mean regression is used to quantify the approximate change in past sea ice cover using the ice core Na_{flux} record. The BEAST algorithm is used to detect sudden changepoints and trends in the reconstructed SIC. The

reconstructed sea ice record shows an overall decreasing trend, punctuated with three abrupt and short-lived events of rapid decrease followed by an increase in SIC. The annual snow accumulation rates range from 0.1 to 0.9 meters water equivalent, with an average of 0.32 ± 0.16 meters water equivalent. The trend in accumulation rates shows periods of stability (1774 – 1806 CE), a slight decrease (1806 – 1888 CE), and a strong decrease (1927 – 2016 CE) over the last ~250 years. Spectral and wavelet analysis of the reconstructed SIC and snow accumulation record is performed to understand the inherent periodicities and possible influence of ENSO and SAM. Wavelet analysis revealed strong variability in the ENSO band (3 – 8 years), especially after ~1960 CE. Snow accumulation records show accelerated decrease since the late 1920s, concurrent with the in-phase shift of SAM and ENSO, emphasizing the intricate interplay of dynamic processes with local atmospheric circulation and sea ice playing a significant role in influencing snow accumulation in the coastal areas of DML.

6.3 Surface mass balance and summertime melt history over the two ice rises

Ground penetrating radar (GPR) and Global Navigation Satellite System (GNSS) surveys were used to measure spatial variations in SMB over the last three decades and the ice topography of two ice rises studied here, viz., Djupranen and Leningradkollen. The GNSS survey shows that the surface was smooth on the eastern windward side of the ice rises, while it was rough on the western leeward side. There is a strong spatial SMB gradient between low SMB in the inlet of the ice shelf facing the Leningradkollen Ice Rise (0.25 m i.e. a^{-1}) and high SMB in the west towards the more elevated Djupranen Ice Rise (0.75 m i.e. a^{-1}) for the most recent periods 2010 – 2017. This east-west pattern was maintained for the entire observational period of the last three decades (1986 – 2017). The ice rises have their own contrasting SMB patterns owing to distinct ice rise topographies. The spatial-mean SMB over the Leningradkollen Ice Rise was 0.30 m i.e. a^{-1} between 1987 and 2016, whereas the spatial-mean SMB over Djupranen Ice Rise was 0.51 m i.e. a^{-1} during 1990 – 2017. The comparison of radar-derived SMB with modelled SMB from RACMO2.3p2 at 5.5 km resolution shows that while the model capture the main gradient across the ice shelf, the complex coastal topography of the region influences the precipitation patterns, leading to SMB biases on the coastal ice rises. Model estimates of SMB do not match the regional-mean SMB estimates from GPR, or the SMB estimates derived from ice cores collected at the ice-rise summits. The highly variable SMB in the coastal regions of Antarctica needs to be better captured in climate models, in particular by an improved representation of the

kilometre-scale topography of these regions. Improved models of coastal SMB are necessary for improved estimates of ice-shelf mass balance and to improve our understanding of the future evolution of ice rises.

The ice cores were also examined for reconstructing a summertime melt records. On a decadal scale, an increasing trend is visible in summertime melting on both cores over the 20th century. However, the study revealed that the summertime melting over the Leningradkollen ice rise is consistently higher as compared to the Djupranen ice rise, although there are elevation-induced discrepancies on the inter-annual timescale. The uncertainties in density measurements, layer identification, and melt masking result in additional complications. Many of the melt periods observed in our ice cores also coincide with documented evidence of atmospheric rivers (ARs) landfall over the ice rises. However, on an annual timescale, no straightforward relationship between temperature and annual melt from the ice cores is evident, indicating that the observed melt events are a result of the complex interplay of factors like microclimate, local snow surface morphology, topographical influences, precipitation event type, and cloud cover.

6.4 Future perspectives

The Antarctic Ice Sheet (AIS) represents the largest source of uncertainty in future sea level rise projections. Under the high carbon emission scenarios estimate by the recent Ice Sheet Model Intercomparison for CMIP6 (ISMIP6), AIS contributions range from -5 to 43 cm of sea level equivalent by 2100 CE. Coastal regions, where the AIS interacts with the ocean, are fundamental to our understanding of the linkages between Antarctica and the global climate system. Coastal ice rises in Antarctica also offer unique sites to investigate oceanic and atmospheric dynamics, and their linkages with global/regional systems. Relatively high surface mass balance (SMB) and close proximity to the coastal storms make ice cores from these ice rises ideal to examine ocean-atmosphere interactions. Sea ice around Antarctica provides critical buttressing for its ice shelves and is an important tipping point within the global climate system. The dramatic lows of Antarctic sea ice extent since 2016/17 is associated with various regional climatic factors and localised extreme events. Therefore, it is critically important to better understand the past tipping points in sea ice loss and its impact on the air-sea exchange of CO_2 within the Southern Ocean.

Majority of Antarctic ice cores studies are focussed on inland regions of Antarctica and there is a lack of long and continuous high-resolution climate records from coastal

region, despite its importance. Ice core records from the DML coast of Antarctica have been shown to reconstruct accumulation, summertime melting, sea ice, dust influx, and other climate variables on an annual to decadal timescale. However, the temporal coverage of all these cores is limited to few centuries and many of these records provide conflicting differences. Most importantly, most of these do not have sea ice records. While some ice cores show an increasing trend in snow accumulation since the beginning of the 20th century, majority of them show a decreasing or no significant trend. The highly complex and variable topography of the region, which influences the wind directions and precipitation patterns, and the influence of the extreme precipitation events, has apparently influenced the complex records in the coastal Antarctica. It is, therefore, important to identify multiple ice core sites from coastal ice rises at sufficiently high elevations, which are also placed at the suitable climatic and oceanic settings. Considering the critical need to have extended sea ice and climatic records from coastal Antarctica, future studies must work towards obtaining more multiple, high-resolution and long ice core records from this region to better understand the processes controlling the local, regional and possibly global climate variability.

References

Abram, N. J., et al.: Ice core evidence for a 20th century decline of sea ice in the Bellingshausen Sea, Antarctica, J Geophys Res-Atmos, 115, D23101, 2010.

Abram, N. J., Mulvaney, R., and Arrowsmith, C.: Environmental signals in a highly resolved ice core from James Ross Island, Antarctica, Journal of Geophysical Research, 116, 2011.

Abram, N. J., et al.: Acceleration of snow melt in an Antarctic Peninsula ice core during the twentieth century, Nat Geosci, 6, 404-411, 2013a.

Abram, N. J., Wolff, E. W., and Curran, M. A. J.: A review of sea ice proxy information from polar ice cores, Quaternary Sci Rev, 79, 168-183, 2013b.

Abram, N. J., et al.: Evolution of the Southern Annular Mode during the past millennium, Nature Climate Change, 4, 564-569, 2014.

Alley, R. B. and Anandakrishnan, S.: Variations in melt-layer frequency in the GISP2 ice core: implications for Holocene summer temperatures in central Greenland, Annals of Glaciology, 21, 64-70, 1995.

Alley, R. B., et al.: Visual-stratigraphic dating of the GISP2 ice core: Basis, reproducibility, and application, Journal of Geophysical Research: Oceans, 102, 26367-26381, 1997.

Altnau, S., et al.: Climatic signals from 76 shallow firn cores in Dronning Maud Land, East Antarctica, Cryosphere, 9, 925-944, 2015.

Baldwin, M. P.: Annular modes in global daily surface pressure, Geophys Res Lett, 28, 4115-4118, 2001.

Berman, E. S., et al.: Measurement of δ18O, δ17O, and 17O-excess in water by off-axis integrated cavity output spectroscopy and isotope ratio mass spectrometry, Analytical chemistry, 85, 10392-10398, 2013.

Bertler, N. A. and Barrett, P. J.: Vanishing polar ice sheets, Springer, 2010.

Bertler, N. A. N., et al.: El Nino suppresses Antarctic warming, Geophys Res Lett, 31, L15207, 2004.

Bertler, N. A. N., et al.: The Ross Sea Dipole - temperature, snow accumulation and sea ice variability in the Ross Sea region, Antarctica, over the past 2700 years, Clim Past, 14, 193-214, 2018.

Bindschadler, R., et al.: The Landsat Image Mosaic of Antarctica, Remote Sensing of Environment, 112, 4214-4226, 2008.

Bindschadler, R., et al.: Getting around Antarctica: new high-resolution mappings of the grounded and freely-floating boundaries of the Antarctic ice sheet created for the International Polar Year, Cryosphere, 5, 569-588, 2011.

Bindschadler, R. A., Roberts, E. P., and MacAyeal, D. R.: Distribution of Net Mass Balance in the Vicinity of Crary Ice Rise, Antarctica, Journal of Glaciology, 35, 370-377, 1989.

Boening, C., et al.: Snowfall-driven mass change on the East Antarctic ice sheet, Geophys Res Lett, 39, 2012.

Bógalo, J., Poncela, P., and Senra, E.: Circulant singular spectrum analysis: A new automated procedure for signal extraction, Signal Processing, 179, 107824, 2021.

Bracegirdle, T. J., et al.: The importance of sea ice area biases in 21st century multimodel projections of Antarctic temperature and precipitation, Geophys Res Lett, 42, 2015.

Brook, E. J.: Ice Core Methods | Overview. In: Encyclopedia of Quaternary Science, Elias, S. A. (Ed.), Elsevier, Oxford, 2007.

Callens, D., et al.: Transition of flow regime along a marine-terminating outlet glacier in East Antarctica, The Cryosphere, 8, 867-875, 2014.

Callens, D., et al.: Temporally stable surface mass balance asymmetry across an ice rise derived from radar internal reflection horizons through inverse modeling, Journal of Glaciology, 62, 525-534, 2016.

Campbell, E. C., et al.: Antarctic offshore polynyas linked to Southern Hemisphere climate anomalies, Nature, 570, 319-325, 2019.

Cauquoin, A., et al.: Modeling the global bomb tritium transient signal with the AGCM LMDZ-iso: A method to evaluate aspects of the hydrological cycle, J Geophys Res-Atmos, 121, 12612-12629, 2016.

Ciasto, L. M. and England, M. H.: Observed ENSO teleconnections to Southern Ocean SST anomalies diagnosed from a surface mixed layer heat budget, Geophys Res Lett, 38, 2011.

Clark, I. and Fritz, P.: Tracing the carbon cycle, Environmental isotopes in hydrogeology, 111-134, 1997.

Cotté, C. and Guinet, C.: Historical whaling records reveal major regional retreat of Antarctic sea ice, Deep Sea Research Part I: Oceanographic Research Papers, 54, 243-252, 2007.

Cuffey, K. M. and Steig, E. J.: Isotopic diffusion in polar firn: implications for interpretation of seasonal climate parameters in ice-core records, with emphasis on central Greenland, Journal of Glaciology, 44, 273-284, 1998.

Cuffey, K. M. and Paterson, W. S. B.: The physics of glaciers, Oxford, 2010.

Curran, M. A. J., Jones, G. B., and Burton, H.: Spatial distribution of dimethylsulfide and dimethylsulfoniopropionate in the Australasian sector of the Southern Ocean, J Geophys Res-Atmos, 103, 16677-16689, 1998.

Curran, M. A. J., et al.: Ice Core Evidence for Antarctic Sea Ice Decline Since the 1950s, Science (New York, N.Y.), 302, 1203-1206, 2003.

Dahl-Jensen, D., et al.: Past accumulation rates derived from observed annual layers in the GRIP ice core from Summit, Central Greenland, 1993, 517-532.

Dansgaard, W.: Stable isotopes in precipitation, Tellus, 16, 436-468, 1964.

Dansgaard, W. and Johnsen, S. J.: A flow model and a time scale for the ice core from Camp Century, Greenland, Journal of Glaciology, 8, 215-223, 1969.

Das, S. B. and Alley, R. B.: Characterization and formation of melt layers in polar snow: Observations and experiments from West Antarctica, Journal of Glaciology, 51, 307-312, 2005.

Das, S. B. and Alley, R. B.: Rise in frequency of surface melting at Siple Dome through the Holocene: Evidence for increasing marine influence on the climate of West Antarctica, Journal of Geophysical Research: Atmospheres, 113, D02112, 2008.

de la Mare, W. K.: Abrupt mid-twentieth-century decline in Antarctic sea-ice extent from whaling records, Nature, 389, 57-60, 1997.

de la Mare, W. K.: Changes in Antarctic sea-ice extent from direct historical observations and whaling records, Climatic Change, 92, 461-493, 2008.

Diener, T., et al.: Acceleration of Dynamic Ice Loss in Antarctica From Satellite Gravimetry, Frontiers in Earth Science, 9, 2021.

Ding, M., et al.: Spatial variability of surface mass balance along a traverse route from Zhongshan station to Dome A, Antarctica, Journal of Glaciology, 57, 658 - 666, 2011.

Dixon, D., et al.: A 200 year sub-annual record of sulphate in West Antarctica, from 16 ice cores, Ann Glaciol-Ser, 39, 545-556, 2004.

Dixon, D., et al.: A 200 year sulphate record from 16 Antarctic ice cores and associations with Southern Ocean sea-ice extent, Annals of Glaciology, 41, 155-166, 2005.

Doran, P. T., et al.: Valley floor climate observations from the McMurdo dry valleys, Antarctica, 1986-2000, J Geophys Res-Atmos, 107, 4772, 2002.

Drews, R., et al.: Evolution of Derwael Ice Rise in Dronning Maud Land, Antarctica, over the last millennia, J Geophys Res-Earth, 120, 564-579, 2015.

Drews, R., et al.: Atmospheric and Oceanographic Signatures in the Ice Shelf Channel Morphology of Roi Baudouin Ice Shelf, East Antarctica, Inferred From Radar Data, J Geophys Res-Earth, 125, e2020JF005587, 2020.

Eayrs, C., et al.: Rapid decline in Antarctic sea ice in recent years hints at future change, Nat Geosci, 14, 460-464, 2021.

Eisen, O., et al.: Ground-based measurements of spatial and temporal variability of snow accumulation in east Antarctica, Reviews of Geophysics, 46, RG2001, 2008.

Ejaz, T., et al.: Sea Ice Variability and Trends in the Western Indian Ocean Sector of Antarctica During the Past Two Centuries and Its Response to Climatic Modes, J Geophys Res-Atmos, 126, e2020JD033943, 2021.

Emanuelsson, B. D., et al.: Ice Core Chronologies from the Antarctic Peninsula: The Palmer, Jurassic, and Rendezvous Age-Scales, Geosciences, 12, 2022.

Etourneau, J., et al.: Ocean temperature impact on ice shelf extent in the eastern Antarctic Peninsula, Nature communications, 10, 304-304, 2019.

Faria, S. H., Freitag, J., and Kipfstuhl, S.: Polar ice structure and the integrity of ice-core paleoclimate records, Quaternary Sci Rev, 29, 338-351, 2010.

Favier, L. and Pattyn, F.: Antarctic ice rise formation, evolution, and stability, Geophys Res Lett, 42, 4456-4463, 2015.

Ferreira, D., et al.: Antarctic Ocean and Sea Ice Response to Ozone Depletion: A Two-Time-Scale Problem, Journal of Climate, 28, 1206-1226, 2015.

Fisher, D. A., Reeh, N., and Clausen, H.: Stratigraphic noise in time series derived from ice cores, Annals of Glaciology, 7, 76-83, 1985.

Fogt, R. L. and Bromwich, D. H.: Decadal Variability of the ENSO Teleconnection to the High-Latitude South Pacific Governed by Coupling with the Southern Annular Mode, Journal of Climate, 19, 979-997, 2006.

Fogt, R. L. and Marshall, G. J.: The Southern Annular Mode: Variability, trends, and climate impacts across the Southern Hemisphere, Wires Clim Change, 11, 2020.

Fogt, R. L., et al.: A regime shift in seasonal total Antarctic sea ice extent in the twentieth century, Nature Climate Change, 12, 54-62, 2022.

Frezzotti, M., et al.: A synthesis of the Antarctic surface mass balance during the last 800 yr, Cryosphere, 7, 303-319, 2013.

Fürst, J. J., et al.: The safety band of Antarctic ice shelves, Nature Climate Change, 6, 479-482, 2016.

Garbe, J.: PISM version as used in Garbe et al.(Nature, 2020) publication (Version v1. 0-hysteresis-antarctica), 2020.

Genthon, C., et al.: Do climate models underestimate snow accumulation on the Antarctic plateau? A re-evaluation of/from in situ observations in East Wilkes and Victoria Lands, Annals of Glaciology, 50, 61-65, 2009.

Gersonde, R., et al.: Sea-surface temperature and sea ice distribution of the Southern Ocean at the EPILOG Last Glacial Maximum—a circum-Antarctic view based on siliceous microfossil records, Quaternary Sci Rev, 24, 869-896, 2005.

Ghadi, P., et al.: Antarctic sea-ice and palaeoproductivity variation over the last 156,000 years in the Indian sector of Southern Ocean, Marine Micropaleontology, 160, 101894, 2020.

Goel, V., Brown, J., and Matsuoka, K.: Glaciological settings and recent mass balance of Blåskimen Island in Dronning Maud Land, Antarctica, The Cryosphere, 11, 2883-2896, 2017.

Goel, V., et al.: Characteristics of ice rises and ice rumples in Dronning Maud Land and Enderby Land, Antarctica, Journal of Glaciology, 66, 1064-1078, 2020.

Goel, V., et al.: Synthesis of field and satellite data to elucidate recent mass balance of five ice rises in Dronning Maud Land, Antarctica, Frontiers in Earth Science, 10, 2022.

Gonfiantini, R.: Standards for stable isotope measurements in natural compounds, Nature, 271, 534-536, 1978.

Goodwin, I., et al.: Mid latitude winter climate variability in the South Indian and southwest Pacific regions since 1300 AD, Climate Dynamics, 22, 783-794, 2004.

Goosse, H., et al.: Consistent past half-century trends in the atmosphere, the sea ice and the ocean at high southern latitudes, Climate Dynamics, 33, 999-1016, 2009.

Gorodetskaya, I. V., et al.: Meteorological regimes and accumulation patterns at Utsteinen, Dronning Maud Land, East Antarctica: Analysis of two contrasting years, Journal of Geophysical Research: Atmospheres, 118, 1700-1715, 2013.

Gorodetskaya, I. V., et al.: Cloud and precipitation properties from ground-based remote-sensing instruments in East Antarctica, Cryosphere, 9, 285-304, 2015.

Goursaud, S., et al.: A 60-year ice-core record of regional climate from Adélie Land, coastal Antarctica, The Cryosphere, 11, 343-362, 2017.

Gow, A. J.: On the Accumulation and Seasonal Stratification Of Snow at the South Pole, Journal of Glaciology, 5, 467-477, 1965.

Hall, A. and Visbeck, M.: Synchronous Variability in the Southern Hemisphere Atmosphere, Sea Ice, and Ocean Resulting from the Annular Mode*, Journal of Climate, 15, 3043-3057, 2002.

Hammer, C. U.: Acidity of polar ice cores in relation to absolute dating, past volcanism, and radio-echoes, Journal of Glaciology, 25, 359-372, 1980.

Handcock, M. S. and Raphael, M. N.: Modeling the annual cycle of daily Antarctic sea ice extent, The Cryosphere, 14, 2159-2172, 2020.

Herron, M. M. and Langway, C. C.: Firn Densification: An Empirical Model, Journal of Glaciology, 25, 373-385, 1980.

Herron, M. M., Herron, S. L., and Langway, C. C.: Climatic signal of ice melt features in southern Greenland, Nature, 293, 389-391, 1981.

Heuzé, C., et al.: Spaceborne infrared imagery for early detection of Weddell Polynya opening, The Cryosphere, 15, 3401-3421, 2021.

Hobbs, W., et al.: Century-scale perspectives on observed and simulated S outhern O cean sea ice trends from proxy reconstructions, Journal of Geophysical Research: Oceans, 121, 7804-7818, 2016.

Hogg, A. E., et al.: Extending the record of Antarctic Ice Shelf thickness change, from 1992 to 2017, Advances in Space Research, 68, 724-731, 2021.

Howat, I. M., et al.: The Reference Elevation Model of Antarctica, The Cryosphere, 13, 665-674, 2019.

IPCC, C. C.: The Physical Science Basis: Working Group I Contribution to the Intergovernmental Panel on Climate Change Fifth Assessment Report (AR5)–Changes to the Underlying Scientific/Technical Assessment. Cambridge University Press, Cambridge, UK, 2013.

Isaacs, F. E., et al.: ENSO Modulates Summer and Autumn Sea Ice Variability Around Dronning Maud Land, Antarctica, Journal of Geophysical Research: Atmospheres, 126, 2021.

Isaksson, E., et al.: Accumulation and proxy-temperature variability in Dronning Maud Land, Antarctica, determined from shallow firn cores, Annals of Glaciology, 29, 17-22, 1999.

Isaksson, E. and Melvold, K.: Trends and patterns in the recent accumulation and oxygen isotopes in coastal Dronning Maud Land, Antarctica: interpretations from shallow ice cores, Annals of Glaciology, 35, 175-180, 2002.

Jena, B., et al.: Record low sea ice extent in the Weddell Sea, Antarctica in April/May 2019 driven by intense and explosive polar cyclones, npj Climate and Atmospheric Science, 5, 19, 2022.

Johnsen, S.: Stable isotope homogenization of polar firn and ice, Isotopes and impurities in snow and ice, 118, 210-219, 1977.

Johnsen, S. J., et al.: Diffusion of stable isotopes in polar firn and ice: the isotope effect in firn diffusion, 2000, 121-140.

Jones, R. S., et al.: Regional-scale abrupt Mid-Holocene ice sheet thinning in the western Ross Sea, Antarctica, Geology, 49, 278-282, 2021.

Jouzel, J. and Merlivat, L.: Deuterium and oxygen 18 in precipitation: Modeling of the isotopic effects during snow formation, Journal of Geophysical Research: Atmospheres, 89, 11749-11757, 1984.

Kaczmarska, M., et al.: Accumulation variability derived from an ice core from coastal Dronning Maud Land, Antarctica, Annals of Glaciology, 39, 339-345, 2004.

Kaczmarska, M., et al.: Ice core melt features in relation to Antarctic coastal climate, Antarct Sci, 18, 271-278, 2006.

Kageyama, M., et al.: Quantifying ice-sheet feedbacks during the last glacial inception, Geophys Res Lett, 31, 2004.

Kameda, T., et al.: Melt features in ice cores from Site J, southern Greenland: some implications for summer climate since AD 1550, Annals of Glaciology, 21, 51-58, 1995.

Karl, T. R. and Trenberth, K. E.: Modern Global Climate Change, Science, 302, 1719-1723, 2003.

Kaspari, S., et al.: Sources and transport pathways of marine aerosol species into West Antarctica, Annals of Glaciology, 41, 1-9, 2005.

Kausch, T., et al.: Impact of coastal East Antarctic ice rises on surface mass balance: insights from observations and modeling, The Cryosphere, 14, 3367-3380, 2020.

Keegan, K. M., et al.: Climate change and forest fires synergistically drive widespread melt events of the Greenland Ice Sheet, Proceedings of the National Academy of Sciences of the United States of America, 111, 7964-7967, 2014.

Kelsey, E., et al.: Ice Layers as an Indicator of Summer Warmth and Atmospheric Blocking in Alaska, Journal of Glaciology, 56, 715-722, 2010.

Kidson, J. W.: Principal modes of Southern Hemisphere low-frequency variability obtained from NCEP–NCAR reanalyses, Journal of Climate, 12, 2808-2830, 1999.

King, J. C. and Turner, J.: Antarctic meteorology and climatology, 1997.

King, J. C., et al.: Wind-borne redistribution of snow across an Antarctic ice rise, J Geophys Res-Atmos, 109, 2004.

Kingslake, J., et al.: Full-depth englacial vertical ice sheet velocities measured using phase-sensitive radar, J Geophys Res-Earth, 119, 2604-2618, 2014.

Kingslake, J., et al.: Widespread movement of meltwater onto and across Antarctic ice shelves, Nature, 544, 349-352, 2017.

Kinnard, C., et al.: Stratigraphic analysis of an ice core from the Prince of Wales Icefield, Ellesmere Island, Arctic Canada, using digital image analysis: High-resolution density, past summer warmth reconstruction, and melt effect on ice core solid conductivity, J Geophys Res-Atmos, 113, 2008.

Koerner, R. M.: Some comments on climatic reconstructions from ice cores drilled in areas of high melt, Journal of Glaciology, 43, 90-97, 1997.

Kovacs, A., Gow, A. J., and Morey, R. M.: The in-situ dielectric constant of polar firn revisited, Cold Reg Sci Technol, 23, 245-256, 1995.

Kreutz, K. J., et al.: Sea level pressure variability in the Amundsen Sea region inferred from a West Antarctic glaciochemical record, Journal of Geophysical Research: Atmospheres, 105, 4047-4059, 2000.

Krinner, G., Genthon, C., and Jouzel, J.: GCM analysis of local influences on ice core δ signals, Geophys Res Lett, 24, 2825-2828, 1997.

Krinner, G., et al.: Simulated Antarctic precipitation and surface mass balance at the end of the twentieth and twenty-first centuries, Climate Dynamics, 28, 215-230, 2007.

Krischke, A., Oechsner, U., and Kipfstuhl, S.: Rapid Microstructure Analysis of Polar Ice Cores, Optik & Photonik, 10, 32-35, 2015.

Kukla, G. and Gavin, J.: Summer ice and carbon dioxide, Science (New York, N.Y.), 214, 497-503, 1981.

Küttel, M., et al.: Seasonal climate information preserved in West Antarctic ice core water isotopes: relationships to temperature, large-scale circulation, and sea ice, Climate Dynamics, 39, 1841-1857, 2012.

Kwok, R. and Comiso, J. C.: Southern Ocean climate and sea ice anomalies associated with the Southern Oscillation, Journal of Climate, 15, 487-501, 2002.

Laluraj, C. M., Thamban, M., and Satheesan, K.: Dust and associated geochemical fluxes in a firn core from coastal East Antarctica and its linkages with Southern Hemisphere climate variability over the last 50 years, Atmospheric Environment, 90, 23-32, 2014.

Langway, C. C.: Stratigraphic analysis of a deep ice core from Greenland, NA, NA, 1967.

Legrand, M. and Mayewski, P.: Glaciochemistry of polar ice cores: A review, Reviews of Geophysics, 35, 219-243, 1997.

Legrand, M. R. and Delmas, R. J.: The ionic balance of Antarctic snow: A 10-year detailed record, Atmospheric Environment (1967), 18, 1867-1874, 1984.

Legrand, M. R. and Delmas, R. J.: Relative contributions of tropospheric and stratospheric sources to nitrate in Antarctic snow, Tellus B: Chemical and Physical Meteorology, 38, 236-249, 1986.

Lemieux-Dudon, B., et al.: Consistent dating for Antarctic and Greenland ice cores, Quaternary Sci Rev, 29, 8-20, 2010.

Lenaerts, J. T. M., et al.: A new, high-resolution surface mass balance map of Antarctica (1979-2010) based on regional atmospheric climate modeling, Geophys Res Lett, 39, 2012.

Lenaerts, J. T. M., et al.: Recent snowfall anomalies in Dronning Maud Land, East Antarctica, in a historical and future climate perspective, Geophys Res Lett, 40, 2684-2688, 2013.

Lenaerts, J. T. M., et al.: High variability of climate and surface mass balance induced by Antarctic ice rises, Journal of Glaciology, 60, 1101-1110, 2014.

Lenaerts, J. T. M., et al.: Present-day and future Antarctic ice sheet climate and surface mass balance in the Community Earth System Model, Climate Dynamics, 47, 1367-1381, 2016.

Lenaerts, J. T. M., et al.: Meltwater produced by wind-albedo interaction stored in an East Antarctic ice shelf, Nature Climate Change, 7, 58, 2017.

Lenaerts, J. T. M., et al.: Observing and Modeling Ice Sheet Surface Mass Balance, Reviews of geophysics (Washington, D.C. : 1985), 57, 376-420, 2019.

Li, R., et al.: A continuous 293-year record of volcanic events in an ice core from Lambert Glacier basin, East Antarctica, 24, 293-298, 2012.

Liston, G. E., et al.: Below-surface ice melt on the coastal Antarctic ice sheet, Journal of Glaciology, 45, 273-285, 1999.

Löfverström, M., et al.: Evolution of the large-scale atmospheric circulation in response to changing ice sheets over the last glacial cycle, Clim Past, 10, 1453-1471, 2014.

MacAyeal, D. R., et al.: Force, mass, and energy budgets of the Crary Ice Rise complex, Antarctica, Journal of Glaciology, 33, 218-230, 1987.

Magudeeswaran, V. and Singh, J. F.: Contrast limited fuzzy adaptive histogram equalization for enhancement of brain images, International Journal of Imaging Systems and Technology, 27, 98-103, 2017.

Mahalinganathan, K. and Thamban, M.: Potential genesis and implications of calcium nitrate in Antarctic snow, The Cryosphere, 10, 825-836, 2016.

Mann, M. E., et al.: Global signatures and dynamical origins of the Little Ice Age and Medieval Climate Anomaly, science, 326, 1256-1260, 2009.

Marshall, G. J.: Trends in the Southern Annular Mode from Observations and Reanalyses, Journal of Climate, 16, 4134-4143, 2003.

Marshall, H.-P., Koh, G., and Forster, R. R.: Ground-based frequency-modulated continuous wave radar measurements in wet and dry snowpacks, Colorado, USA: an analysis and summary of the 2002–03 NASA CLPX data, Hydrological Processes, 18, 3609-3622, 2004.

Martin, S., Yu, Y., and Drucker, R.: The temperature dependence of frost flower growth on laboratory sea ice and the effect of the flowers on infrared observations of the surface, Journal of Geophysical Research: Oceans, 101, 12111-12125, 1996.

Masson-Delmotte, V., et al.: A Review of Antarctic Surface Snow Isotopic Composition : Observations, Atmospheric Circulation, and Isotopic Modeling, Journal of Climate, 21, 3359-3387, 2008.

Matsuoka, K., et al.: Antarctic ice rises and rumples: Their properties and significance for ice-sheet dynamics and evolution, Earth-Sci Rev, 150, 724-745, 2015.

McGwire, K. C., et al.: An integrated system for optical imaging of ice cores, Cold Reg Sci Technol, 53, 216-228, 2008a.

McGwire, K. C., et al.: Dating annual layers of a shallow Antarctic ice core with an optical scanner, Journal of Glaciology, 54, 831-838, 2008b.

Medley, B. and Thomas, E.: Increased snowfall over the Antarctic Ice Sheet mitigated twentieth-century sea-level rise, Nature Climate Change, 9, 34-39, 2019.

Meese, D., et al.: The Greenland Ice Sheet Project 2 depth-age scale: methods and results, Journal of Geophysical Research: Oceans, 102, 26411-26423, 1997.

Moholdt, G. and Matsuoka, K.: Inventory of Antarctic ice rises and rumples (version 1), Norwegian Polar Institute, Tromsø, Norway. 2015.

Moore, J., et al.: Sulphate source inventories from a Svalbard ice core record spanning the Industrial Revolution, J Geophys Res-Atmos, 111, 2006.

Morcillo, G., Faria, S. H., and Kipfstuhl, S.: Unravelling Antarctica's past through the stratigraphy of a deep ice core: an image-analysis study of the EPICA-DML line-scan images, Quaternary International, 566-567, 6-15, 2020.

Mouginot, J., et al.: Comprehensive Annual Ice Sheet Velocity Mapping Using Landsat-8, Sentinel-1, and RADARSAT-2 Data, Remote Sensing, 9, 364, 2017.

Naik, S. S., et al.: A century of climate variability in central Dronning Maud Land, East Antarctica, and its relation to Southern Annular Mode and El Niño-Southern Oscillation, Journal of Geophysical Research, 115, 2010.

Nair, A., et al.: Southern Ocean sea ice and frontal changes during the Late Quaternary and their linkages to Asian summer monsoon, Quaternary Sci Rev, 213, 93-104, 2019.

Neff, P. D.: A review of the brittle ice zone in polar ice cores, Annals of Glaciology, 55, 72-82, 2014.

Nicolas, J. P., et al.: January 2016 extensive summer melt in West Antarctica favoured by strong El Niño, Nature communications, 8, 15799, 2017.

Nye, J. F.: On the theory of the advance and retreat of glaciers, Geophysical Journal International, 7, 431-456, 1963.

Ohmura, A.: Physical Basis for the Temperature-Based Melt-Index Method, Journal of Applied Meteorology, 40, 753-761, 2001.

Orr, A., et al.: Characteristics of surface "melt potential" over Antarctic ice shelves based on regional atmospheric model simulations of summer air temperature extremes from 1979/80 to 2018/19, Journal of Climate, 36, 3357-3383, 2023.

Parish, T. R.: Surface winds over the Antarctic continent: A review, 26, 169-180, 1988.

Parkinson, C. L. and Cavalieri, D. J.: Antarctic sea ice variability and trends, 1979–2010, The Cryosphere, 6, 871-880, 2012.

Parkinson, C. L.: A 40-y record reveals gradual Antarctic sea ice increases followed by decreases at rates far exceeding the rates seen in the Arctic, Proc Natl Acad Sci U S A, 116, 14414-14423, 2019.

Parrenin, F., et al.: New modeling of the Vostok ice flow line and implication for the glaciological chronology of the Vostok ice core, Journal of Geophysical Research: Atmospheres, 109, 2004.

Parrenin, F., et al.: 1-D-ice flow modelling at EPICA Dome C and Dome Fuji, East Antarctica, Clim Past, 3, 243-259, 2007.

Pavlis, N. K., Holmes, S., and Kenyon, S.: The development and evaluation of the Earth Gravitational Model 2008 (EGM2008), Journal of Geophysical Research: Solid Earth, 117, 2012.

Pfeffer, W. T., Illangasekare, T. H., and Meier, M. F.: Analysis and modeling of melt-water refreezing in dry snow, Journal of Glaciology, 36, 238-246, 1990.

Pfeffer, W. T. and Humphrey, N. F.: Determination of timing and location of water movement and ice-layer formation by temperature measurements in sub-freezing snow, Journal of Glaciology, 42, 292-304, 1996.

Pfeffer, W. T. and Humphrey, N. F.: Formation of ice layers by infiltration and refreezing of meltwater, Annals of Glaciology, 26, 83-91, 1998.

Philippe, M., et al.: Ice core evidence for a 20th century increase in surface mass balance in coastal Dronning Maud Land, East Antarctica, The Cryosphere, 10, 2501-2516, 2016.

Pohjola, V. A., et al.: Effect of periodic melting on geochemical and isotopic signals in an ice core from Lomonosovfonna, Svalbard, J Geophys Res-Atmos, 107, 2002.

Pratap, B., et al.: Three-decade spatial patterns in surface mass balance of the Nivlisen Ice Shelf, central Dronning Maud Land, East Antarctica, Journal of Glaciology, 68, 174-186, 2022.

Purich, A., et al.: Evidence for link between modelled trends in Antarctic sea ice and underestimated westerly wind changes, Nature communications, 7, 10409-10409, 2016.

Purich, A. and Doddridge, E. W.: Record low Antarctic sea ice coverage indicates a new sea ice state, Communications Earth & Environment, 4, 314, 2023.

Rankin, A., Auld, V., and Wolff, E.: Frost flowers as a source of fractionated sea salt aerosol in the polar regions, Geophys Res Lett, 27, 3469-3472, 2000.

Rignot, E., Mouginot, J., and Scheuchl, B.: Ice Flow of the Antarctic Ice Sheet, Science (New York, N.Y.), 333, 1427-1430, 2011.

Rignot, E., et al.: Ice-shelf melting around Antarctica, Science, 341, 266-270, 2013.

Rignot, E., et al.: Four decades of Antarctic Ice Sheet mass balance from 1979-2017, Proceedings of the National Academy of Sciences of the United States of America, 116, 1095-1103, 2019.

Roscoe, H. K., et al.: Frost flowers in the laboratory: growth, characteristics, aerosol, and the underlying sea ice, Journal of Geophysical Research, 116, D12301, 2011.

Röthlisberger, R., et al.: Potential and limitations of marine and ice core sea ice proxies: an example from the Indian Ocean sector, Quaternary Sci Rev, 29, 296-302, 2010.

Rutz, J. J., et al.: The Atmospheric River Tracking Method Intercomparison Project (ARTMIP): Quantifying Uncertainties in Atmospheric River Climatology, Journal of Geophysical Research: Atmospheres, 124, 13777-13802, 2019.

Scambos, T. A., et al.: The link between climate warming and break-up of ice shelves in the Antarctic Peninsula, Journal of Glaciology, 46, 516-530, 2000.

Schlosser, E. and Oerter, H.: Shallow firn cores from Neumayer, Ekströmisen, Antarctica: a comparison of accumulation rates and stable-isotope ratios, Annals of Glaciology, 35, 91-96, 2002.

Schlosser, E., et al.: Characteristics of high-precipitation events in Dronning Maud Land, Antarctica, Journal of Geophysical Research: Atmospheres, 115, 2010.

Schneider, D. P., et al.: Antarctic temperatures over the past two centuries from ice cores, 33, 2006.

Schneider, D. P. and Noone, D. C.: Spatial covariance of water isotope records in a global network of ice cores spanning twentieth-century climate change, Journal of Geophysical Research: Atmospheres, 112, 2007.

Schröder, L., et al.: Four decades of Antarctic surface elevation changes from multi-mission satellite altimetry, The Cryosphere, 13, 427-449, 2019.

Schulz, M. and Mudelsee, M.: REDFIT: estimating red-noise spectra directly from unevenly spaced paleoclimatic time series, Computers & Geosciences, 28, 421-426, 2002.

Shepherd, A., Wingham, D., and Rignot, E.: Warm ocean is eroding West Antarctic ice sheet, Geophys Res Lett, 31, 2004.

Shields, C. A., et al.: Atmospheric River Tracking Method Intercomparison Project (ARTMIP): project goals and experimental design, Geosci. Model Dev., 11, 2455-2474, 2018.

Shindell, D. T. and Schmidt, G. A.: Southern Hemisphere climate response to ozone changes and greenhouse gas increases, Geophys Res Lett, 31, 2004.

Sigl, M., et al.: A new bipolar ice core record of volcanism from WAIS Divide and NEEM and implications for climate forcing of the last 2000 years, Journal of Geophysical Research: Atmospheres, 118, 1151-1169, 2013.

Sime, L. C., et al.: Interpreting temperature information from ice cores along the Antarctic Peninsula: ERA40 analysis, Geophys Res Lett, 36, 2009.

Sinclair, K. E., Bertler, N. A. N., and Trompetter, W. J.: Synoptic controls on precipitation pathways and snow delivery to high-accumulation ice core sites in the Ross Sea region, Antarctica, Journal of Geophysical Research, 115, 2010.

Sinclair, K. E., et al.: Twentieth century sea-ice trends in the Ross Sea from a high-resolution, coastal ice-core record, Geophys Res Lett, 41, 3510-3516, 2014.

Sinisalo, A., et al.: Surface mass balance on Fimbul ice shelf, East Antarctica: Comparison of field measurements and large-scale studies, J Geophys Res-Atmos, 118, 11625-11635, 2013.

Sjögren, B., et al.: Determination of firn density in ice cores using image analysis, Journal of Glaciology, 53, 413-419, 2007.

Slater, T., et al.: Earth's ice imbalance, The Cryosphere, 15, 233-246, 2021.

Smith, E., et al.: Detailed Seismic Bathymetry Beneath Ekström Ice Shelf, Antarctica: Implications for Glacial History and Ice-Ocean Interaction, Geophys Res Lett, 47, 2020.

Stammerjohn, S., et al.: Trends in Antarctic annual sea ice retreat and advance and their relation to El Niño–Southern Oscillation and Southern Annular Mode variability, Journal of Geophysical Research: Oceans, 113, 2008.

Stenni, B., et al.: 200 years of isotope and chemical records in a firn core from Hercules Névé, northern Victoria Land, Antarctica, Annals of Glaciology, 29, 106-112, 1999.

Stenni, B., et al.: Snow accumulation rates in northern Victoria Land, Antarctica, by firn-core analysis, Journal of Glaciology, 46, 541-552, 2000.

Stenni, B., et al.: Antarctic climate variability on regional and continental scales over the last 2000 years, Clim Past, 13, 1609-1634, 2017.

Stuecker, M. F., Bitz, C. M., and Armour, K. C.: Conditions leading to the unprecedented low Antarctic sea ice extent during the 2016 austral spring season, Geophys Res Lett, 44, 9008-9019, 2017.

Svensson, A., et al.: Visual stratigraphy of the North Greenland Ice Core Project (NorthGRIP) ice core during the last glacial period, J Geophys Res-Atmos, 110, 2005.

Svensson, A., et al.: A 60 000 year Greenland stratigraphic ice core chronology, Clim Past, 4, 47-57, 2008.

Takata, M., et al.: Stratigraphic analysis of Dome Fuji Antarctic ice core using an optical scanner, Ann Glaciol-Ser, 39, 467-472, 2004.

Tedesco, M. and Monaghan, A. J.: An updated Antarctic melt record through 2009 and its linkages to high-latitude and tropical climate variability, Geophys Res Lett, 36, 2009.

Thamban, M., et al.: Aerosol perturbations related to volcanic eruptions during the past few centuries as recorded in an ice core from the Central Dronning Maud Land, Antarctica, Curr. Sci., 91, 1200-1207, 2006.

Thamban, M., et al.: Glaciochemistry of surface snow from the Ingrid Christensen Coast, East Antarctica, and its environmental implications, 22, 435-441, 2010.

Thamban, M., et al.: Antarctic Climate Variability During the Past Few Centuries Based on Ice Core Records from Coastal Dronning Maud Land and Its Implications on the Recent Warming. In: Earth System Processes and Disaster Management, Sinha, R. and Ravindra, R. (Eds.), Springer Berlin Heidelberg, Berlin, Heidelberg, 2013.

The firn symposium team: Firn on Ice Sheets, Nature Reviews Earth & Environment, 2023.

The IMBIE team: Mass balance of the Antarctic Ice Sheet from 1992 to 2017, Nature, 558, 219-222, 2018.

Thomas, E. R. and Abram, N. J.: Ice core reconstruction of sea ice change in the Amundsen-Ross Seas since 1702 A.D, Geophys Res Lett, 43, 5309-5317, 2016.

Thomas, E. R., et al.: Regional Antarctic snow accumulation over the past 1000 years, Clim Past, 13, 1491-1513, 2017.

Thompson, D. W. J. and Solomon, S.: Interpretation of Recent Southern Hemisphere Climate Change, Science, 296, 895-899, 2002.

Torrence, C. and Compo, G. P.: A practical guide to wavelet analysis, Bulletin of the American Meteorological society, 79, 61-78, 1998.

Trenberth, K. E. and Solomon, A.: The global heat balance: Heat transports in the atmosphere and ocean. 1994.

Turner, J.: The El Nino-southern oscillation and Antarctica, Int J Climatol, 24, 1-31, 2004.

Turner, J., et al.: Non-annular atmospheric circulation change induced by stratospheric ozone depletion and its role in the recent increase of Antarctic sea ice extent, Geophys Res Lett, 36, 2009.

Turner, J., et al.: Unprecedented springtime retreat of Antarctic sea ice in 2016, Geophys Res Lett, 44, 6868-6875, 2017.

Turner, J., et al.: The Dominant Role of Extreme Precipitation Events in Antarctic Snowfall Variability, 46, 3502-3511, 2019.

Turner, J., et al.: Record Low Antarctic Sea Ice Cover in February 2022, Geophys Res Lett, 49, 2022.

van den Broeke, M.: Strong surface melting preceded collapse of Antarctic Peninsula ice shelf, Geophys Res Lett, 32, 2005.

van den Broeke, M. R., Reijmer, C., and van de Wal, R. S. W.: Surface radiation balance in Antarctica as measured with automatic weather stations, Journal of Geophysical Research, 109, 2004.

van Ommen, T. D. and Morgan, V.: Calibrating the ice core paleothermometer using seasonality, Journal of Geophysical Research: Atmospheres, 102, 9351-9357, 1997.

Van Ommen, T. D., Morgan, V., and Curran, M. A.: Deglacial and holocene changes in accumulation at Law Dome, East Antarctica, Annals of Glaciology, 39, 359-365, 2004.

van Wessem, J. M., et al.: Modelling the climate and surface mass balance of polar ice sheets using RACMO2 – Part 2: Antarctica (1979–2016), The Cryosphere, 12, 1479-1498, 2018.

Vance, T., et al.: A Millennial Proxy Record of ENSO and Eastern Australian Rainfall from the Law Dome Ice Core, East Antarctica, Journal of Climate, 26, 710-725, 2013.

Vaughan, D. G., et al.: Recent Rapid Regional Climate Warming on the Antarctic Peninsula, Climatic Change, 60, 243-274, 2003.

Vega, C. P., et al.: Surface mass balance and water stable isotopes derived from firn cores on three ice rises, Fimbul Ice Shelf, Antarctica, The Cryosphere, 10, 2763-2777, 2016.

Vernet, M., et al.: The Weddell Gyre, Southern Ocean: Present Knowledge and Future Challenges, Reviews of Geophysics, 57, 623-708, 2019.

Vignon, É., et al.: Present and future of rainfall in Antarctica, Geophys Res Lett, 48, e2020GL092281, 2021.

Vinther, B., et al.: Climatic signals in multiple highly resolved stable isotope records from Greenland, Quaternary Sci Rev, 29, 522-538, 2010.

Vinther, B. M., et al.: A synchronized dating of three Greenland ice cores throughout the Holocene, Journal of Geophysical Research: Atmospheres, 111, 2006.

Waddington, E. D., et al.: Inference of accumulation-rate patterns from deep layers in glaciers and ice sheets, Journal of Glaciology, 53, 694-712, 2007.

Wang, G., et al.: Compounding tropical and stratospheric forcing of the record low Antarctic sea-ice in 2016, Nature communications, 10, 13-NA, 2019.

Wang, Y., et al.: A Comparison of Antarctic Ice Sheet Surface Mass Balance from Atmospheric Climate Models and In Situ Observations, Journal of Climate, 29, 5317-5337, 2016.

Wauthy, S., et al.: Physico-chemical properties of the top 120 m of two ice cores in Dronning Maud Land (East Antarctica): an open window on spatial and temporal regional variability of environmental proxies, Earth Syst. Sci. Data Discuss., 2023, 1-33, 2023.

Westhoff, J., et al.: A stratigraphy-based method for reconstructing ice core orientation, Annals of Glaciology, 62, 191-202, 2020.

Wille, J., et al.: Atmospheric River Climatology of Antarctica, 2019.

Winski, D., et al.: High-frequency observations of melt effects on snowpack stratigraphy, Kahiltna Glacier, Central Alaska Range, Hydrological Processes, 26, 2573-2582, 2012.

Winstrup, M., et al.: An automated approach for annual layer counting in ice cores, Clim Past, 8, 1881-1895, 2012.

Wolff, E. W., Rankin, A. M., and Röthlisberger, R.: An ice core indicator of Antarctic sea ice production?, Geophys Res Lett, 30, 2003.

Wolff, E. W., et al.: Southern Ocean sea-ice extent, productivity and iron flux over the past eight glacial cycles, Nature, 440, 491-496, 2006.

Wolff, E. W.: Chemical signals of past climate and environment from polar ice cores and firn air, Chem Soc Rev, 41, 6247-6258, 2012.

Yang, X., Pyle, J. A., and Cox, R. A.: Sea salt aerosol production and bromine release: Role of snow on sea ice, Geophys Res Lett, 35, 2008.

Yeo, S.-R. and Kim, K.-Y.: Decadal changes in the Southern Hemisphere sea surface temperature in association with El Niño–Southern Oscillation and Southern Annular Mode, Climate Dynamics, 45, 3227-3242, 2015.

Yuan, X. J.: ENSO-related impacts on Antarctic sea ice: a synthesis of phenomenon and mechanisms, Antarct Sci, 16, 415-425, 2004.

Zhang, M., et al.: 250 years of accumulation, oxygen isotope and chemical records in a firn core from Princess Elizabeth Land, East Antarctica, Journal of Geographical Sciences, 16, 23-33, 2006.

Zhao, K., et al.: Detecting change-point, trend, and seasonality in satellite time series data to track abrupt changes and nonlinear dynamics: A Bayesian ensemble algorithm, Remote Sensing of Environment, 232, 111181, 2019.

Zwally, H. J., et al.: Variability of Antarctic sea ice 1979–1998, Journal of Geophysical Research: Oceans, 107, 2002.

List of publications

From this thesis:

1. **Rahul Dey,** Meloth Thamban, Chavarukonam Madhavanpillai Laluraj, Kanthanathan Mahalinganathan, Bhikaji Laxman Redkar, Sudhir Kumar, Kenichi Matsuoka (2023). Application of visual stratigraphy from line scan images to constrain chronology and melt features of a firn core from coastal Antarctica. ***Journal of Glaciology,*** 69(273), 179-190 (**Impact Factor – 3.4**)

2. Bhanu Pratap, **Rahul Dey**, Kenichi Matsuoka, Geir Moholdt, Katrin Lindbäck, Vikram Goel, C. M. Laluraj, Meloth Thamban (2022). Three-decade spatial patterns in surface mass balance of the Nivlisen Ice Shelf, central Dronning Maud Land, East Antarctica. ***Journal of Glaciology,*** 68(267), 174-186 (**Impact Factor – 3.4**).

Other:

1. **The firn symposium team**. Firn on ice sheets (in press). ***Nature Reviews Earth and Environment***. (**Impact Factor – 42.1**)

2. Marie G. P. Cavitte, Hugues Goosse, Kenichi Matsuoka, Sarah Wauthy, Vikram Goel, **Rahul Dey**, et. al., (2023). Investigating the spatial representativeness of Antarctic ice cores: A comparison of ice core and radar-derived surface mass balance. ***The Cryosphere***, 17, 4779–4795 (**Impact Factor – 5.2**)

3. Vikas Dev, Vishvesh Kumar Pathak, **Rahul Dey**, et al., (2022). Calcareous peloids in the north-western Arabian Sea: implications of late Quaternary marine sedimentation and paleoclimate. ***Arabian Journal of Geosciences,*** 15, 105.

List of conference presentations

1. **Rahul Dey**, Meloth Thamban, Chavarukonam Madhavanpillai Laluraj, Kenichi Matsuoka (11 – 20th July 2023). 250 years of summertime melting and snow accumulation in the coastal Dronning Maud Land, East Antarctica (Oral). IUGG 2023 General Assembly, Berlin, Germany.

2. **Rahul Dey**, Meloth Thamban, Chavarukonam Madhavanpillai Laluraj, Kenichi Matsuoka (16 – 19th May 2023). Sea ice influenced climate variability in coastal Antarctica (Poster). National Conference on Polar Science, Goa, India

3. **Rahul Dey**, Meloth Thamban, Chavarukonam Madhavanpillai Laluraj, Kenichi Matsuoka (2 – 7th October 2022). Role of sea ice cover in controlling the snow accumulation variability and stable isotopic composition of precipitation in coastal Antarctica (Poster). 3rd IPICS Open Science Conference, Crans-Montana, Switzerland.

4. **Rahul Dey**, Meloth Thamban, Chavarukonam Madhavanpillai Laluraj, Kenichi Matsuoka (1 – 10th August 2022). What controls the stable isotope ratios of precipitation in coastal Antarctica? (Oral) 10th SCAR Open Science Conference (Virtual), India.

5. **Rahul Dey**, Meloth Thamban, C.M. Laluraj, K. Mahalinganathan, Tariq Ejaz, Bhanu Pratap, Kenichi Matsuoka (20 – 22nd August 2019). Snow accumulation variability over the past century in coastal Dronning Maud Land, East Antarctica: insights from ice core records. National Conference on Polar Science, Goa, India.